THESIS FOR THE DEGREE OF DOCTOR OF ENGINEERING

Synthesis, Structure and Proton Conduction of Substituted $BaTiO_3$ and $BaZrO_3$ Perovskites

SEIKH M. H. RAHMAN

Department of Chemical and Biological Engineering

CHALMERS UNIVERSITY OF TECHNOLOGY

Göteborg, Sweden 2013

Synthesis, Structure and Proton Conduction of Substituted $BaTiO_3$ and $BaZrO_3$ Perovskites

SEIKH M. H. RAHMAN

ISBN: 978-91-7385-927-1

Doktorsavhandlingar vid Chalmers tekniska högskola
Serial no:3608
ISSN: 0346-718X

Department of Chemical and Biological Engineering
Chalmers University of Technology
SE-412 96 Göteborg
Sweden
Telephone + 46 (0)31-772 1000

Cover: Hexagonal and cubic perovskites, complex plane plot.

Printed at Chalmers Reproservice AB
Göteborg, Sweden 2013

Dedication

To my family

To my mother and father, who has been teaching ever since...,

To my wife, Tasnoova Hoq, who has been travelling this journey, all the way side by side.

And most importantly:

To my kids: Tahmid, Taibah and Fatin Ilham, for bringing endless joy of life.

Synthesis, Structure and Proton Conduction of Substituted $BaTiO_3$ and $BaZrO_3$ Perovskites

Thesis for the Doctor of Engineering
Department of Chemical and Biological Engineering
Chalmers University of Technology, 2013

Abstract

Proton conducting oxides can be beneficial as electrolyte materials in devices such as fuel cells, hydrogen sensors etc. Proton conducting fuel cells (PCFCs), utilising H_2 as fuel, stand out as a promising technology for future clean energy generation. The works herein is devoted to improve the performance of current state of the art perovskite structured $BaZrO_3$ based electrolyte materials as well as synthesise and characterise novel electrolytes within the $BaTiO_3$ based systems. Usually acceptor doping of these perovskites allows for proton conductivity in hydrogen containing atmosphere. In this thesis heavily co-doped strategy along with the impact of addition of sintering aid (ZnO) and various synthesis routes in $BaZrO_3$ based materials is being tested. Heavily doped $BaTiO_3$ based systems are also synthesised for the first time and characterised with an emphasis on proton conduction. This work is based on techniques such as X-ray powder diffraction studies, neutron powder diffraction, thermogravimetric analysis and AC impedance spectroscopy. In addition a neutron total scattering study is employed for the first time to understand the local structural environment for the deuteron position in a proton conducting electrolyte. Co-doping and sintering aid (in solution synthesis) for the In/Yb:$BaZrO_3$ electrolyte seems to be beneficial. Heavily substituted Sc/In:$BaTiO_3$ materials also show enhanced proton conductivity.

Keywords: *New proton conductor, heavily doped oxygen deficient perovskite (BaTiO3/ BaZrO3), X-ray and neutron powder diffraction, Rietveld refinements, deuteron position, Impedance spectroscopy, neutron total scattering, RMC modelling.*

List of publications:

This thesis is based on papers and manuscripts listed below.

I. Istaq Ahmed, Francis G. Kinyanjui, Seikh M. H. Rahman, Patrick Steegstra, Sten G. Eriksson and Elisabet Ahlberg, *"Proton conductivity in mixed B-site doped perovskite oxide $BaZr_{0.5}In_{0.25}Yb_{0.25}O_{3-\partial}$,* Journal of the Electrochemical Society 157 (2010) (12) B1819.

II. Seikh M. H. Rahman, Istaq Ahmed and Sten G. Eriksson, *"Synthesis and enhanced proton conduction in a 20 mol% ytterbium doped barium zirconate ceramic using Zn as sintering aid"*, Applied Mechanics and Materials 110-116 (2011)1181.

III. Seikh M. H. Rahman, Christopher S. Knee, Istaq Ahmed, Sten G. Eriksson and Reidar Haugsrud, *"50 mol% In doped $BaTiO_3$: Characterization of Structure and Conductivity"*, International Journal of Hydrogen Energy 37 (2012) (9) 7975.

IV. Stefan T. Norberg, Seikh M. H. Rahman, Stephen Hull, Christopher S. Knee and Sten G. Eriksson., *"The proton conducting electrolyte $BaTi_{0.5}In_{0.5}O_{2.75}$: Determination of the deuterium site and its local environment"* J. Phys.: Condens. Matter 25 (2013) 454214

V. Seikh M. H. Rahman, , Istaq Ahmed, Reidar Haugsrud , Sten G. Eriksson and Christopher S. Knee *"Characterisation of structure and conductivity of $BaTi_{0.5}Sc_{0.5}O_{3-\delta}$"*, submitted to Solid State Ionics, June 2013.

VI. Seikh M. H. Rahman, Stefan T. Norberg; Christopher S. Knee, Jordi. J. Biendicho, Stephen Hull and Sten G. Eriksson, *"Characterisation of structure and proton conductivity of hexagonal and cubic $BaTi_{1-x}Sc_xO_{3-\delta}$ $[0.1 \leq x \leq 0.8]$"*, manuscript in preparation.

My contributions to the papers in the order above

I formulated and designed the studies, Synthesised and prepared samples, designed and performed the experiments, analysed the data, and was mainly writing the manuscript, with exceptions below.

Paper I: except inception of the study / part of experimental data collection and analysis / writing the manuscript.

Paper III: except SEM data collection.

Paper IV: except design of study, data analysis and manuscript for the RMC and total scattering section.

Paper V: except thermodynamics of hydration section data analysis and part of discussion regarding this hydration.

Additional publications not included in the thesis

I. Istaq Ahmed, Seikh M.H. Rahman, Patrick Steegstra, Stefan T. Norberg, Sten-G. Eriksson, Elisabet Ahlberg, Chris S. Knee, and Stephen Hull,"*Effect of co-doping on proton conductivity in perovskite oxides* $BaZr_{0.9}In_{0.05}M_{0.05}O_{3-\partial}$ *(M =* Yb^{3+} *or* Ga^{3+}*)"*, International journal of hydrogen energy 35(2010) , 6381-6391.

II. Chernov, S.V., Dobrovolsky, Y.A., Istomin, S.Y., Antipov, E.V., Grins, J., Svensson, G., Tarakina, N.V., Abakumov, A.M., Van Tendeloo, G., Eriksson, S.G., Rahman, S.M.H., *"*Sr_2GaScO_5*,* $Sr_{10}Ga_6Sc_4O_{25}$*, and* $SrGa_{0.75}Sc_{0.25}O_{2.5}$*: a Play in the Octahedra to Tetrahedra Ratio in Oxygen-Deficient Perovskites"*, Inorg Chem 51 (2012) (2) 1094.

III. John Gustavsson, Christine Hummelgård, Joakim Bäckström, Inger Odnevall Wallinder, Seikh Mohammad Habibur Rahman, Göran Lindbergh, Sten Eriksson and Ann Cornell, *"In-situ activated hydrogen evolution by molybdate addition to neutral and alkaline electrolytes"*, J. Electrochem. Sci. Eng. 2(3) (2012) 105-120.

IV. Christine Hummelgård, Rasmus Karlsson, Joakim Bäckström, Seikh M.H. Rahman, Ann Cornell, Sten Eriksson and Håkan Olin *"Physical and electrochemical properties of cobalt doped* $(Ti,Ru)O_2$ *electrode coatings"* Accepted in Materials Science and Engineering B, 2013(0).

V. Johan Bielecki, Stewart F. Parker, Seikh M. H. Rahman, Christopher S. Knee, Sten G. Eriksson, Lars Börjesson and Maths Karlsson *"Local structure and hydration/dehydration properties of proton conducting brownmillerite* $Ba_2In_2O_5$ *investigated with Raman spectroscopy"*, in manuscript.

VI. Maryia Ivanova, Sandrine Ricote, Habibur Rahman, Morten Huse and Reidar Haugsrud , *"Novel High-Temperature Proton and Mixed-Proton Electron Conductors for Fuel Cells and* H_2*-Separation Membranes"* 2011, http://www.nordicenergy.org/wp-content/uploads/2012/01/Novel-High-Temperature-final-report.pdf

Table of Contents

List of Tables

List of Figures

Thesis layout

The content of the thesis is organized as follows. With the research presented mainly in the appended papers, the summarising chapters 1-5 are used to explain the subject and place the results in a wider perspective. The introductory chapter (Chapter 1) states the motivation for the thesis project as well as the overall approach of this research. Chapter 2 contains general background and a literature review with a special focus on intermediate temperature fuel cells. Chapter 3 gives a literature review of oxide and proton-conducting ceramics, and mechanisms of ion incorporation and conduction, as well as some structural and physical properties of $BaTiO_3$/$BaZrO_3$. Chapter 4 refer to the experimental methods and procedures used for the synthesis of materials for the project. Methods of characterization by X-ray powder diffraction (XRPD), neutron powder diffraction (NPD), thermogravimetric analysis (TGA), impedance spectroscopy (IS), infrared spectroscopy (IR), scanning electron microscopy (SEM) etc. are also briefly explained in chapter 4. A summary of results and discussion is then provided in chapter 5. A brief conclusion and future prospect is outlined in chapter 6.

List of Abbreviations

CHHP	Combined Heat, Hydrogen, and Power
SOFC	Solid Oxide Fuel Cells
PCFC	Proton conducting-/ (Proton conducting solid oxide-)/ proton ceramic- fuel cell
PEMFC	Proton Exchange Membrane-/ (Polymer Electrolyte Membrane) Fuel Cells
HTPC	High Temperature Proton Conductors
HTMPE	High Temperature Mixed Proton Electron Conductors
MIEC	Mixed Ionic–Electronic Conductors
AFC	Alkaline Fuel Cells
PAFC	Phosphoric Acid Fuel Cells
MCFC	Molten Carbonate Fuel Cells
DMFC	Direct Methanol Fuel Cells
ASR	Area Specific Proton Resistances Ωcm^2.
EIS/IS	Electrochemical impedance spectroscopy / Impedance spectroscopy
XRPD	X-ray powder diffraction
NPD	Neutron powder diffraction
RMC	Reverse Monte Carlo
FT-IR	Fourier Transformed-Infrared Spectroscopy
TGA	Thermogravimetric Analysis
SEM	Scanning Electron Microscopy
EDS	Energy dispersive X-ray spectroscopy
ΔG	Gibbs free energy, $Jmol^{-1}$
F	Faraday's constant, F= 96,485 $Cmol^{-1}$
E^0	Equilibrium cell potential, Volts (V)

YSZ	Yttria stabilized zirconia
CGO	Gadolinia stabilized zirconia
SDC	Samaria stabilized zirconia
BZY20	$BaZr_{0.8}Yb_{0.2}O_{3-\delta}$, (Y = Y/Yb)
BZY	Y-doped barium zirconate
BZIY50	$BaZr_{0.5}In_{0.25}Yb_{0.25}O_{3-\delta}$
BTI50	$BaTi_{0.5}In_{0.5}O_{3-\delta}$
BTS50	$BaTi_{0.5}Sc_{0.5}O_{3-\delta}$
σ_H/σ_D	Ratio of Conductivities in proton (H) / Deuteron (D)
SHE	Standard hydrogen electrode
σ	conductivities / partial conductivities $\Omega^{-1}cm^{-1}$ or Scm^{-1}
$\sigma_{m,tot}$	Total conductivity
$\sigma_{m,proton}$	Total proton conductivity
$\sigma_{s,proton}$	Specific total proton conductivity (porosity corrected)
$p(H_2O)$	Partial pressure of water
$p(O_2)$	Partial pressure of oxygen
ΔH^0_{hydr}	Molar hydration enthalpy change
ΔS^0_{hydr}	Molar hydration entropy change
E_a	Activation energy
t	Goldschmidt tolerance factor
$v_O^{\bullet\bullet}$	oxygen vacancy (effective charge = +2)
$[OH_O^{\bullet}]$	Hydroxide/ proton defects
$Mf_B^{/}/Acc^{/}$	M^{3+} dopant ion at the B site (acceptor) (effective charge is – 1)
$A_A^{\times}$	A^{2+} metal ion at its original position (effective charge =0)
$O_O^{\times}$	oxygen ion at its position (effective charge =0)

1. Introduction

1.1 MOTIVATION FOR THE THESIS PROJECT

Whereas the 19th Century was the century of the steam engine and the 20th Century was The century of the internal combustion engine, it is likely that the 21st Century will be the Century of the fuel cell [1]. Fuel cells generate electricity by an electrochemical reaction in which oxygen and a hydrogen-rich fuel combine to form water. Unlike internal combustion engines, the fuel is not combusted, the energy instead being released electrocatalytically. This allows fuel cells to be highly energy efficient (2-3 times more efficient than thermal power plants or internal combustion engines), especially if the heat produced by the reaction is also harnessed [2].

Full cells are now on the verge of being introduced commercially, impacting on the way we currently produce power. Fuel cells can use hydrogen gas as a fuel, offering the prospect of supplying the world with clean, sustainable electrical power. Hydrogen driven fuel cells are an ideal alternative to the internal combustion engine and seen as a key technology to reduce vehicle emissions of greenhouse gases, as vehicles are one of the largest and fastest-growing emission sources. However, energy is used and greenhouse gases are produced "upstream" from the vehicle fuel cell itself, to produce, store and transport hydrogen [3].

In a successful hydrogen economy, energy from solar panels and wind-power is converted into chemical energy via the splitting of water into hydrogen and oxygen. Although implementation of an ideal hydrogen economy is a long-term ambition,

development of the fuel cell devices is currently receiving significant attention [4]. A study on cumulative number of fuel cell related patents awarded over time shows that from 2000 through 2011, an average of 26 patents per year were awarded. [4].

Fuel cell based combined heat, hydrogen, and power (CHHP) production systems (tri-generation energy system) [5] or IDEAL-Cell [6] where the cell works simultaneously as proton and oxide ion conducting with operating temperature ranging of 600 to 700 °C are also emerging to boost overall efficiency.

In recent years research on the development of intermediate temperature fuel cells operating between 200 and 600 °C, has gained much momentum. This is a most desirable operating temperature range for many practical applications. Fuel cells operating in this temperature range have some advantages of both high temperature fuel cells (e.g. solid oxide fuel cells – SOFC – operating at 700-1000 °C) and that of low temperature fuel cells (proton exchange membrane fuel cells – PEMFC – operating at 70-100 °C) such as fast electrode kinetics, short start-up time, fuel flexibility, use of inexpensive non-platinum catalysts, particularly insensitive to impurities in the fuel (e.g. CO) and less degradation problems. Major approaches in the development of intermediate temperature fuel cells would include searching for new electrolyte materials with a sufficiently high ionic conductivity in the intermediate temperature range. The solid oxide fuel cell contains a critical electrolyte component made of a ceramic oxide material. So far the development of commercially viable SOFCs have been hindered by issues related to the stability and performance of available materials [7, 8]. This thesis deals with aspects related to some of these concerns. Taking advantage of the ability of X-ray and neutron diffraction to realistically describe materials structure on the atomic scale, conductivity of few candidate materials for proton conducting electrolytes will be addressed.

1.2 Overall objective

The overall approach is to develop a solid oxide proton conducting and solid oxide mixed proton electron conducting membranes for fuel cells and hydrogen

separation membranes with area specific proton resistances (ASR) below 0.1 Ωcm^2. This may be achieved by improving the proton transport properties of complex oxides like perovskites, double perovskites, brownmillerites, pyrochlores. These goals should be obtained through:

- Optimisation of traditional acceptor doping and development of novel schemes for co-doping.
- Application and development of "soft chemistry" routes in order to prepare homogeneously doped materials and new low temperature compounds normally unattainable at elevated temperature.
- A focuson finding correlations between structural and functional properties of proton conducting electrolytes by applying state-of-the-art X-ray powder and neutron powder diffraction (XRPD/NPD) along with electrochemical impedance spectroscopy (EIS) techniques.

2. Fuel cell

2.1 FUEL CELL SYSTEMS

The fuel cell is not a new concept, rather it has been known for almost two centuries. The US space program during the sixties practically utilized it while the momentum in development and commercial inauguration took place in nineties [9]. At present there are many issues such as cost, efficiency and reliability stopping fuel cells from reaching full commercialization. Hence, the discovery of a chemically stable and highly conducting electrolyte remains at the forefront of focus. In this circumstance, intermediate temperature (200-700 °C) fuel cells offer very attractive solutions over other counterparts. The intention of this chapter is to briefly provide a background regarding fuel cells with particular emphasis on operating temperature, SOFCs and the conductivity of electrolyte materials. All the information in this chapter are covered thoroughly in references [6, 9-31] along with the references mentioned below.

2.1.1 Basic principle of solid oxide fuel cells

A fuel cell is by definition an electrical cell, that convert hydrogen, or a hydrogen-containing fuel's chemical energy, directly into electrical energy plus heat through the electrochemical reaction of hydrogen and oxygen to give water. The process is that of electrolysis in reverse. The main components of a fuel cell include fuel electrode (anode) and an oxidant electrode (cathode) separated by a membrane (electrolyte) which lets ions through. The electrodes employ catalysts, to activate, the hydrogen oxidation and oxygen reduction. The electrodes then split respective H_2 and O_2 molecules and incorporate the atoms into its structure where they are ionized. Electrons from the anode flow through

the electrical load in the external loop to the cathode, while protons and/or oxygen ions are transported in the electrolyte. Depending on whether the electrolyte conducts oxide ions and/or protons, the components are then assembled into water at the anode and/or the cathode. Charge is carried through oxide ions as illustrated in SOFC (Figure 2.1(a)) or by hydrogen ions (protons) as in Proton Exchange Membrane Fuel Cell (PEMFC)/ Proton Conducting Fuel Cell (PCFC) (Figure 2.1(b)). The reactions of the hydrogen fuel cell are and potential against standard hydrogen electrode (SHE) thus [11]:

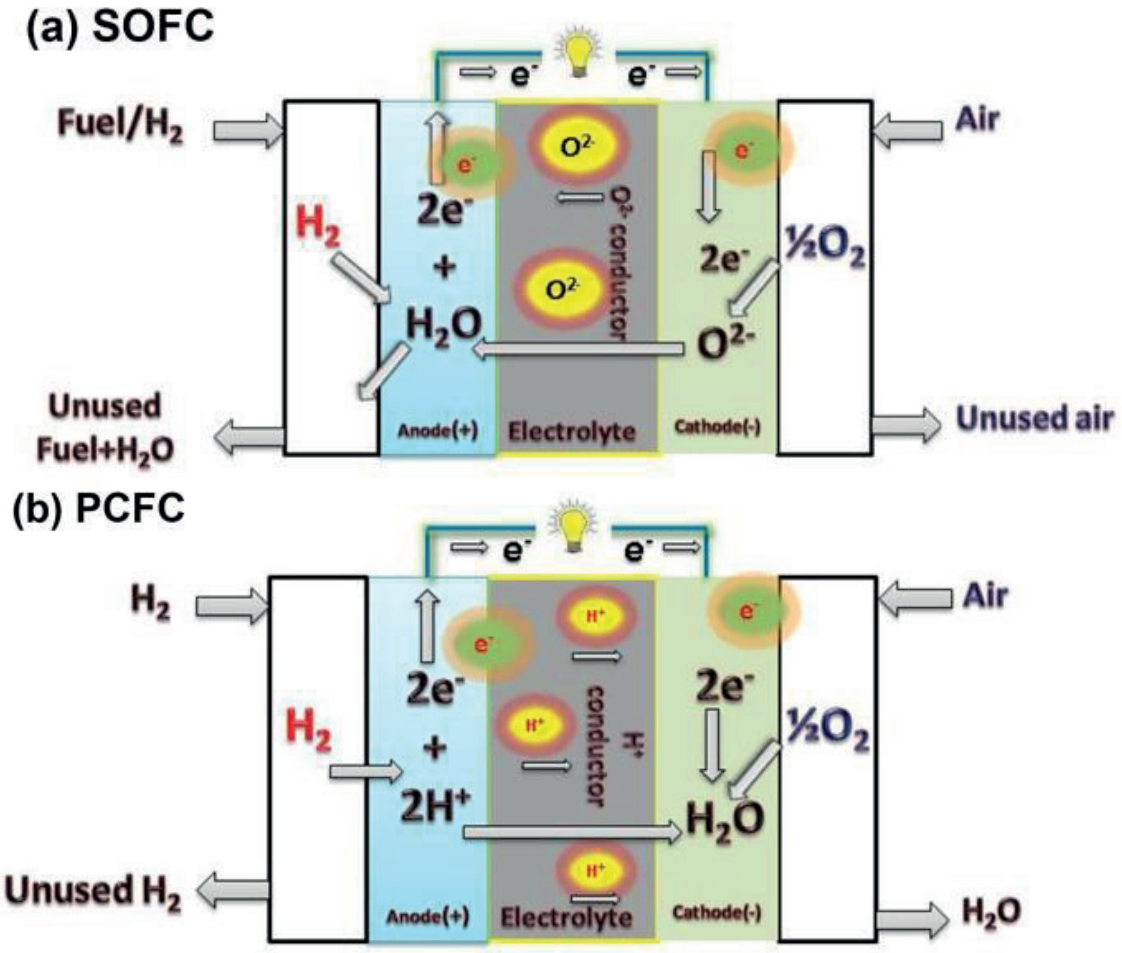

Figure 2.1(a) Solid Oxide Fuel Cell (SOFC): charge carrier: oxide ion. (b) Proton Conducting Fuel Cell (PCFC): charge carrier: proton.

Anode: $2H_2 \rightarrow 4H^+ + 4e^-$ $E°$=0 V vs. SHE (2.1)

Cathode: $O_2 + 4H^+ + 4e^- \rightarrow 2H_2O$, $E°$=1.23 V vs. SHE (2.2)

The overall reaction is then:

$O_2 + 2H_2 \rightarrow 2H_2O$ $E°$=1.23 V, with ΔG = -237 kJ/mol [11] (2.3)

2.2 FUEL CELLS: SOFC, PEMFC AND PCFC

Fuel cells are categorized by their electrolyte material and ionic transport mechanism. Table 2.1 shows most common types of fuel cells and their supplementary features [18]. The thermodynamic potential for a fuel cell theoretically stands at 1.23 V. However, in practice PEMFCs exhibit a voltage of about 0.6 V for current densities of 0.6-0.8 A/cm^2. In order to improve power generation, individual fuel cells are usually combined into a fuel cell "stack". An interconnect plate is always installed to provide the electronic contact between the anode of one cell and the cathode of the next cell [24].

SOFC and PEMFC are two of the main fuel cell systems that are in advantageous position towards commercialisation. They have their advantages and disadvantages in terms of operating temperature, materials used, cost and applications. SOFCs use a solid ceramic electrolyte, where oxygen dissociates at the cathode; oxide ions migrate through the electrolyte to the anode, react with hydrogen and form water. Subsequently, the functioning norm of this fuel cell type is dissimilar than PEMFCs in the sense that oxide ions and not protons are migrating in the electrolyte. SOFCs usually utilize relatively low cost materials such as yttria stabilized zirconia (YSZ), which has been used for more than 25 years. However, operating temperatures of 800-1000 °C are needed to achieve sufficient ionic conductivity in the electrolyte and thus they are generally classified as high-temperature (HT) solid oxide fuel cells [21, 24, 32]. Their high operating temperature means that electrochemical reactions on the electrodes do not require the use of noble metal catalysts and in addition fuels can be reformed within the fuel cell itself. This eliminating the need for external reforming and allows the units to be used with a variety of hydrocarbon fuels, carbon monoxide and renewable biomasses [33]. They are

also relatively resistant to small quantities of sulphur in the fuel, compared to other types of fuel cell, and can hence be used with coal gas.

Dense ceramic electrolytes prevent fuel crossover from the anode to the cathode side. High overall (fuel to electricity and heat) efficiencies up to 80% can also be achieved due to the high-grade heat that can be utilised. The high operating temperature also leads to some disadvantages; such as the stability in oxidising and reducing conditions, chemical compatibility with various ceramics employed, thermal expansion compatibility of various components over the large temperature range, and adequate ionic conductivity of the membrane. In addition, because of the high operating temperature, long waiting times for heat up and cool down cycles are required in order to minimize the structural stresses caused by the expansion and contraction of materials in the cell. These issues can cause shorter service life due to the materials degradation, components, etc.[19]

On the other hand, PEMFC fuel cells generally use perfluorosulfonic acid (PFSA) polymer, trade name Nafion, as the electrolyte. In these kinds of fuel cells H_3O^+ is the ionic charge carrier in the electrolyte, and relies on liquid water humidification of the polymeric membrane. This consequently restricts the operating temperature upward to 90 °C, since at higher temperature the membrane would be dry with correspondingly low conductance. More recently other materials, e.g. polybenzimidazle (PBI) have been suggested that retain protons to higher temperatures than PFSA. These have the advantage of increasing their temperature of operation up to 220 °C without using any water management. The low operating temperature of PEMFCs constrains the choice of materials for the electrodes. To reach the required reaction rate only very catalytically active materials can be used. In a conventional PEMFC, platinum and platinum alloys are the typical catalyst in the carbon electrodes. They offer short start-up time, broad range of applications, higher efficiency, good power density and design and package flexibility...

Table 2.1: Fuel Cells currently in use or development with their important features listed.

Parameters	Fuel cell types					
	PEMFC	**AFC**	**PAFC**	**MCFC**	**SOFC**	**DMFC**
Electrolyte	Solid polymer membrane	Liquid solution of KOH	Phosphoric acid (H_3PO_4)	Li+/Na+ carbonate	Oxide electrolyte	Solid polymer membrane
Operating temp. (°C)	50–100	50–200	~200	~650	800–1000	60–200
Anode reaction	$H_2 \rightarrow 2H^+ + 2e^-$	$H_2 + 2OH^- \rightarrow 2H_2O + 2e^-$	$H_2 \rightarrow 2H^+ + 2e^-$	$H_2 + CO_3^{2-} \rightarrow H_2O + CO_2 + 2e^-$	$H_2 + O^{2-} \rightarrow H_2O + 2e^-$	$CH_3OH + H_2O \rightarrow CO_2 + 6H^+ + 6e^-$
Cathode reaction	$½O_2 + 2H^+ + 2e^- \rightarrow H_2O$	$½O_2 + H_2O + 2e^- \rightarrow 2OH^-$	$½O_2 + 2H^+ + 2e^- \rightarrow H_2O$	$½O_2 + CO_2 + 2e^- \rightarrow CO_3^{2-}$	$½O_2 + 2e^- \rightarrow O^{2-}$	$3O_2 + 12H^+ + 12e^- \rightarrow 6H_2O$
Charge carrier	H^+	OH^-	H^+	CO_3^{2-}	O^{2-}	H^+
Fuel	Pure H_2	Pure H_2	Pure H_2	H_2, CO, CH_4, other hydrocarbons	Any fuel	CH_3OH
Oxidant	O_2 in air	O_2 in air	O_2 in air	O_2 in air	O_2 in air	O_2 in air
Efficiency	40–50%	50%	40%	> 50%	> 50%	40%
Cogeneration	–	–	Yes	Yes	Yes	No
Cell Voltage	1.1	1.0	1.1	0.7–1.0	0.8–1.0	0.2–0.4
Power density (kW/m^3)	3.8–6.5	~1	0.8–1.9	1.5–2.6	0.1–1.5	~0.6

Disadvantages of the currently used PEMFCs are the poor kinetics of the oxygen reduction reaction on the cathode, anode catalysts are sensitive to poisoning by carbon monoxide (CO) and sulphur (S), high materials (Pt, membrane, etc.) cost and large overpotential losses [34].

Therefore, it would be attractive, if SOFCs could be designed to give a reasonable power output at intermediate temperatures (IT, 400–700 °C) [8]. An alternative to oxide ion conducting SOFCs is to use a proton conducing electrolyte. Fuel cells utilizing proton conducting electrolytes, namely acceptor doped Ba and Sr based perovskites, such as Y-doped $BaCeO_3$, Yb-doped $SrCeO_3$ and Y-doped $BaZrO_3$ have been demonstrated and peak power as high as 1200 mW/cm^2 has been claimed [35]. These materials have been called high-temperature proton conductors (HTPCs) to distinguish them from proton-conducting polymers working below 100 °C[8]. The easy proton migration in the HTPCs represents one of the reasons that make HTPCs very attractive electrolyte materials for IT-SOFCs. The proton ceramic fuel cell (PCFC) has the highest theoretical efficiency among the fuel cells when using hydrogen as fuel, due to the possibility of operation close to 100 % fuel utilization [36]. A PCFC works as opposed to a SOFC in such a way that the water is formed on the anode side of the SOFC. It retains most of the benefits of higher temperature by the way of operating as low as 200-700 °C. However, if a PCFC is to operate with natural gas as fuel, the reforming needs to be accomplished before reaching the anode side [21]. More recently, proton electrolytes are utilized in co-ionic conduction, where both O^{2-} and H^{+} can migrate through the electrolyte and fuel cells can be operated as LT-SOFC (Low-temperature SOFC) with higher efficiency [6, 37-39].

2.3 PROSPECTS OF INTERMEDIATE TEMPERATURE FUEL CELL

Current limitations of SOFCs lie in their reliability and durability, directly linked to the high operating temperature needed to limit the Ohmic losses across the electrolyte [21]. The working temperature of a fuel cell has a large influence on fuel cell performance, efficiency, the range of applications, materials, compatibility of the

components and fuels used, etc. High operating temperatures for PEMFCs help increase chemical reaction rates at the electrode surfaces (improving power density). It also makes the fuel cell more superficial to impurities in the fuel and facilitates the use of carbon containing fuels, enabling more direct fuel flexibility and simplification of water management. When the working temperature is low (80 °C, for PEMFC), expensive electrode materials becomes necessary, even with pure hydrogen fuel. If a PEMFC were operated at higher temperatures, this would enable replacement of expensive Pt catalysts with cheaper metal- based catalysts or metallic perovskite-type oxides, as well as improve the use of the heat rejected [40]. The development of a high temperature PEMFC could also eliminate the need for reactant humidification, water-cooling, and other water requirements. This could reduce the weight, volume, and complexity of the fuel cell system, and thus increase the gravimetric/volumetric power density and reduce system cost[41]. On the other hand, decreasing the SOFC working temperature from 800 - 1000 °C towards intermediate ranges offers promising gains, such as increased service life by reducing aging of the materials operated under high temperatures, fast heating-up, less sophisticated fabrication materials (e.g., metals) than ceramic ones for many components (interconnections and heat exchangers, etc.) and increased potential for mobile applications [34, 42].

Development of intermediate temperature fuel cells or IT-SOFC (400-750 °C) [8, 31] could possibly overcome many disadvantages of both the SOFC and the PEMFC [43]. In order to achieve the 'ideal' operating temperature for fuel cells in general, the appropriate fuel cell technology to choose for a given application is driven by variety of factors such as required performance, lifetime, cost, fuel, size, weight, efficiency, start-uptime, waste heat quality, etc. However, it is clear that lowering the operating temperature of SOFCs unlocks a wider range of potential applications, including some that have previously been the domain of low temperature fuel cells [43]. Extensive importance of lowering the operating temperature of SOFC or their potential use and

future prospects can be accessed in more details in the references [7, 21, 26-28, 31, 43-53].

2.4 THE SEARCH FOR NEW ELECTROLYTES

The electrolyte is central among all the important materials in fuel cells. Electrolyte type defines the fuel cell and determines the temperature range of operation. This may be solid (polymer or ceramic) or liquid (aqueous or molten salt) and must have a high ionic and low electronic conductivity for efficient operation. The electrolyte in an SOFC is an oxide ion conductor; however, the electrolyte may also be a proton, carbonate or hydroxide ion conductor depending on the type of fuel cell (see Table 2.1). Research on Proton conducting SOFC or PCFC (Proton conducting solid oxide fuel cell) are particularly highlighted for lowering the operating temperature of SOFC. There is presently a strong interest in new electrolyte and electrode materials for fuel cells operating at intermediate temperatures [9, 10, 15, 17, 27, 31, 45, 48, 54-61].

Different materials are searched for as candidate intermediate temperature electrolyte material e.g. organic materials such as impregnated phosphoric acid- doped polybenzimidazole (PBI) [16, 62, 63], membranes with changed polymer chemistry [64-67], organic-inorganic composites [68-71], oxide ion and proton-conductive ceramic metal oxides [7, 8, 26, 31, 43, 52, 53, 61, 72-85] etc. Despite extensive research, currently there are no solid proton conductors with appropriate conductivity ($\geq 10^{-1}$ S/cm) and reliability for the operating temperature between 200 °C and 500 °C [53].

Solid proton conducting materials and their conductivities, originally compiled by Norby [53] in 1999 and later on updated with some more recent literature data, is presented in Figure 2.4 [41]. It still reveals the lack of suitable electrolyte materials available in this certain temperature range. A recent article comparing between the Arrhenius plots of the proton-conducting Y-doped barium zirconate (BZY) and the best performing oxygen-ion conducting electrolytes measured below 600 °C, [33], reveals significant improvement in terms of proton conductivity as shown in Figure 2.5. In

particularly, $BaZr_{0.8}Y_{0.2}O_{3-\delta}$ (BZY20) and its derivatives such as $BaZr_{0.7}Pr_{0.1}Y_{0.2}O_{3-\delta}$ (BZPY10) or thin films show promising conductivity greater than 1×10^{-2} Scm^{-1} below 600 °C [33].

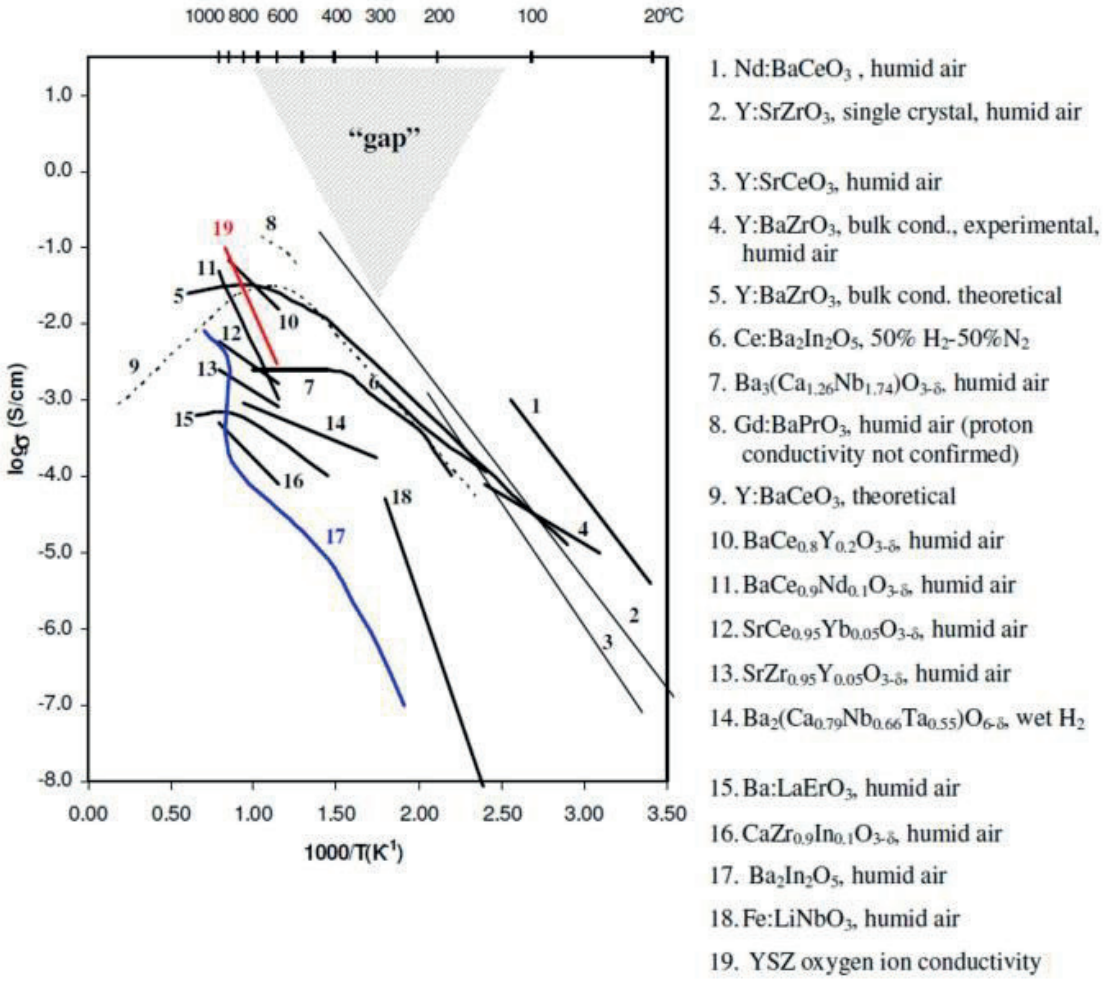

Figure 2.2 Literature data on proton conductivity of selected proton-conducting ceramics. Conductivity of a typical electrolyte material for SOFCs, YZS, is shown for comparison. Reproduced from [41] with permission.

Despite the fact that high-temperature proton-conducting oxides were revealed almost 30 years ago and tried for fuel cell applications, the poor chemical stability and

low proton conductivity is reducing interest in fuel cell applications of these materials. Although various methodologies are being applied and we are slowly getting closer towards optimal performance, commercial applications are still far away and several problems are still to be solved to reach this aim. In particular, Finding suitable electrolyte and electrode materials becomes critical for the development of portable fuel cells based on proton conducting oxides. The research in this field is really still in its infancy and a significant effort is needed to unravel novel electrolyte and electrode materials for proton-conducting or IT- SOFCs.

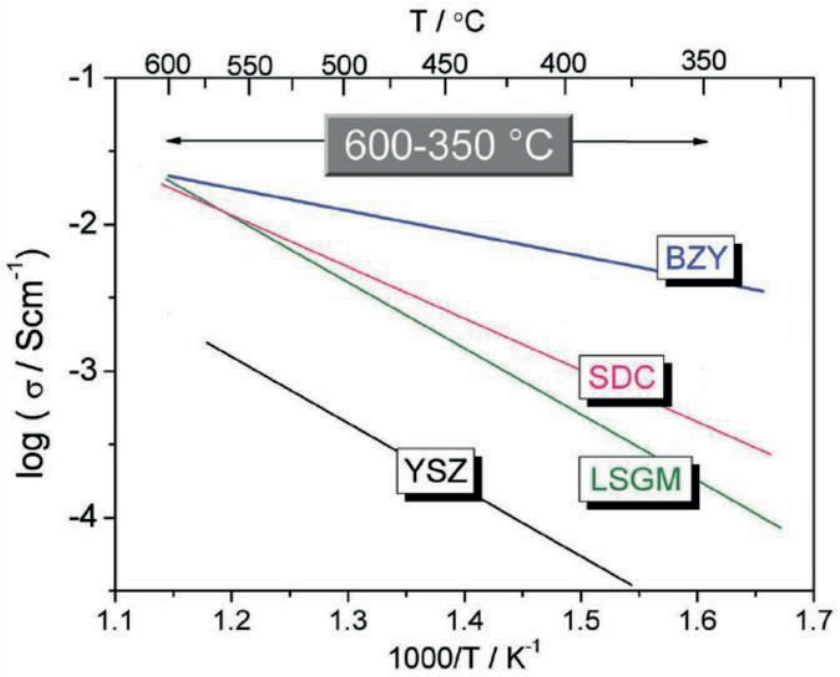

Figure 2.3 Comparison between the Arrhenius plots of the electrical conductivity of the proton-conducting Y-doped barium zirconate (BZY) and the best performing oxygen-ion conducting electrolytes, Sm-doped ceria (SDC) doped lanthanum gallate (LSGM) and yttria-stabilized zirconia (YSZ) measured below 600 °C, all in the form of sintered pellets. Reproduced from [33] with permission.

3: Theory and literature review: Solid oxide electrolytes, Perovskites, Defects and Transport of ions

3.1 INTRODUCTION

The electrolyte is the component of the fuel cell responsible for conducting ions between the electrodes. It also separates the reacting gases and is blocking for the internal electronic conduction and thus forces the electrons to flow through the external circuit. An oxide ion electrolyte conducts O^{2-} whereas proton conduction, results from an oxide's ability to dissolve protons from water vapour or hydrogen. For satisfactory performance, the electrolyte must meet some requirements that limit the choice of the material. There are some general criteria for the quality of a solid oxide electrolyte material to be used in an electrochemical cell: [33, 60, 72, 86, 87] (1) an oxide-ion conductivity greater than 10^{-2} -10^{-1} S.cm^{-1} at the operating temperature; (2) negligible electronic conduction, which means an electronic transport number close to zero; (3) high density to promote gas impermeability; (4) thermodynamic stability over a wide range of temperature and oxygen partial pressure; (5) Thermal expansion co-efficient (TEC) compatible with that of the electrodes and other cell materials from ambient temperature to cell operating temperature; (6) suitable mechanical properties, with fracture resistance greater than 400 MPa at room temperature; (7) negligible chemical interaction with electrode materials under operation and fabrication conditions to avoid formation of blocking interface phases; (8) ability to be prepared as thin layers (less than 30μm); (9) low cost of starting materials and fabrication.

There is an urgent need to develop materials that might allow the deployment of the next generation of SOFCs able to produce a reasonable power output at intermediate

temperatures (IT, 200–700 °C). In the attempt of reducing SOFC operating temperatures, the main issues that must be faced are related to the increasing electrolyte resistivity and electrode polarization [43]. The electrolyte resistance can be lowered either by decreasing its thickness to decrease ohmic losses or by using alternative electrolyte materials having higher ionic conductivity than YSZ in the lower temperature range [33]. The role of materials science is fundamental for discovering and developing electrolyte materials that support high ion conductivities along with the other pre-requisites mentioned above. Intense research in this field, particularly over the last decade, has led to the discovery of several new classes of materials with excellent ion conducting properties, which in some cases exhibit different conduction mechanisms than the vacancy-mediated transport of well-known oxide-ion conductors such as yttria-stabilized zirconia (YSZ). In this chapter the materials which are studied in Papers I–VI, along with a brief overview of other materials relevant to the field, particularly oxide- and proton-conducting electrolytes, are introduced.

3.2 CONVENTIONAL OXIDE-ION CONDUCTORS

Most conventional fast oxide-ion conducting materials have crystal structures of the fluorite type, AO_2, where A is a tetravalent cation. Zirconia for example is stabilized by producing solid solution with trivalent rare earths ZrO_2-Ln_2O_3 or divalent alkaline earth metals ZrO_2-AO. The most widely used are those stabilized with yttrium (YSZ) or scandium (SSZ) [88] . The conductivities of these solid solutions increase with the degree of substitution to an optimum for 8% Y_2O_3 and 11% Sc_2O_3, [89] and this maximum conductivity is reached at a degree of substitution close to the minimum that stabilizes the cubic fluorite phase. YSZ has become the electrolyte most widely used in SOFCs. Although one major drawback is the high working temperatures (800-1000 °C) needed to obtain sufficient ionic conductivity. The drawback of high working temperatures can be partially overcome by replacing YSZ with a stabilized ceria, which has higher conductivities than YSZ, allowing for lower temperature operation (500-700 °C) [27].

Stabilized ceria is normally doped with gadolinia (CGO) or samaria (SDC) and optimum doping levels are in this case close to 10-11% of rare earth oxide. The main drawback of stabilized ceria is the partial reduction of Ce^{4+} to Ce^{3+} under the high temperature reducing conditions present in a fuel cell, and the conductivity of these materials is not purely ionic, with a non-negligible proportion of electronic (n-type) conductivity [27, 72]. Recently, investigations show the possibility of power generation in water concentration cells at room temperature using YSZ or SDC electrolytes when they are nanostructured [27, 90]. An alternative strategy for improving the properties of fluorite-type oxide ion conductors is to add zirconia to ceria (or vice versa), as the fluorite related oxides are mutually soluble. The reduction of cerium is almost negligible at temperatures below 600 °C, which put forward the stabilized ceria as a suitable candidate for intermediate temperature fuel cells (500-600 °C), with the commercialization of such cells being investigated [27].

Another important fast oxide-ion conductor with a fluorite based structure is δ-Bi_2O_3. This compound is characterised by an oxygen sublattice which has one in four of the oxygen sites occupied by intrinsic anion vacancies, which is the basis for its high reported oxide-ion conductivity. However, the highly conductive δ- phase is only stable above ca. 730 °C. Stabilization of this phase to room temperature can be achieved by partially replacing bismuth with rare-earth elements (such as Y, Dy or Er) in combination with supervalent cations, such as Nb or W. Similar to ZrO_2-based electrolytes, the highest ionic conductivities are achieved for materials containing the minimum dopant concentration required to stabilize the cubic fluorite structure. However, in many cases the doping level required is high (15–42 mol %), resulting in relatively poor conductivities, especially at low temperatures. Renewed interest in δ-Bi_2O_3 has mainly focussed on the local structure and ion migration paths using new characterisation techniques such as total neutron scattering [91, 92]. This has revealed that, even though the long-range order evident from conventional X-ray or neutron diffraction is consistent with a cubic symmetry, the local structure of the δ phase closely resembles the distorted

square pyramidal arrangement found within the phase of the pure material stable at ambient temperature, otherwise known as the α phase [91, 92]. For example, $(Bi_2O_3)_{0.735}(Er_2O_3)_{0.21}(WO_3)_{0.055}$ shows a conductivity of 0.05 S cm^{-1} at 550 °C [93] while $(BiO_{1.5})_{0.88}(DyO_{1.5})_{0.08}(WO_3)_{0.04}$ has a conductivity of 0.043 cm^{-1} at 500 °C . This co-doping also increases the stability of the material with time [94]. Although conductivities are higher, in reality these materials have major drawbacks, including partial reduction under low oxygen partial pressures, bismuth volatility at relatively low temperatures, high thermal expansion co-efficient (TEC), and poor mechanical properties [27, 95, 96]. Other fluorite -related materials include the pyrochlore structure with general composition $A_2B_2O_7$. This can be viewed as a superstructure of a defective fluorite , $(A,B)O_{1.75}$, with one oxide-ion vacancy per formula unit, yielding a vacancy concentration of 12.5 mol% [72]. The systems most widely studied compositions are $Gd_2(Ti_{1-x}Zr_x)_2O_7$ and $Gd_{2-y}Ln_yZr_2O_7$ (where Ln = Sm, Nd, La). However, the oxide-ion conductivities of pyrochlore materials are still low compared to other conventional oxides such as YSZ and CGO.

A cubic perovskite structured, lanthanum gallate ($LaGaO_3$) is another well investigated SOFC electrolyte. In these ceramics, La can be partially substituted by Sr, Ca, Ba, Sm and Nd, while Ga may also be partially replaced by Mg, In, Al or Zn, as in $La_{1-x}Sr_xGa_{1-y}Mg_yO_{3-\delta}$ (LSGM). Compositions containing Sr and Mg substitutions respectively for La (between 10 and 20%) and Ga (between 10 and 20%) showed high ionic conductivities in both oxidizing and reducing atmosphere. The introduction of small amounts of Co ($La_{0.8}Sr_{0.2}Ga_{0.8}Mg_{0.115}Co_{0.085}O_3$) increases the oxide ion conductivity, especially at low temperatures (0.1 S cm^{-1} at 650 °C), without causing problems of increasing the *p*-type electronic conduction significantly [97, 98].

Other perovskites known to exhibit oxide-ion conductivities comparable to that of YSZ include $NdGa_{0.9}Mg_{0.1}O_{2.95}$ [99, 100] and $Gd_{0.85}Ca_{0.15}AlO_{2.925}$ [101]. Work is also being carried out on perovskite-related oxides of the K_2NiF_4 ($A_2BO_{4+\delta}$) structure such as $Ln_2NiO_{4+\delta}$ (where Ln = La, Nd, Pr). In these materials, excess oxygen ($\delta > 0$) is

accommodated at interstitial sites with oxide-ion conduction mediated by an interstitial transport mechanism [72, 102].

The brownmillerite-type $Ba_2In_2O_5$ phase can be classed as an oxygen defective perovskite, where at room temperature the oxygen vacancies are ordered, resulting in alternating layers of octahedral and tetrahedral indium [83, 103]. This phase then goes through an order/disorder transition to a tetragonal perovskite above 900 °C that contributes a drastic increase in its oxide ion conductivity (0.1 S cm^{-1} at 900 °C). Several doping approaches have been put forward to pull down this transition temperature or even suppressing it, for example substitutions on the In site by W [104], Ti [105], Ga [106, 107], V, Mo [108], or on the Ba site by La [109, 110] or Sr.

3.3 CONVENTIONAL PROTON CONDUCTORS

While doped $LaGaO_3$ is an excellent oxide ion conductor, other perovskite materials originally conceived as oxide ion conductors have been confirmed to be good proton conductors as well [53, 78, 111, 112]. The dissolution of water into an acceptor-doped oxide at elevated temperature was first examined at the end of the 1960s [111, 113]. However, the real breakthrough in the scientific community regarding proton conduction in ceramic oxides started in the 1980s, when Iwahara and his co-workers completed their systematic studies on acceptor-doped perovskite- type oxides [114-119]. In their studies they found low proton conduction in hydrogen- containing atmospheres for oxides such as $LaAlO_3$, $LaYO_3$, and $SrZrO_3$.

The most widely studied perovskite proton conducting systems are currently cerates [114, 117] and zirconates [120] in the form $Ba(Zr/Ce)_{1-x}Y_xO_{3-x/2}$ [27] with reported maxima in bulk proton conductivity well above 0.005 S cm^{-1} [121]. For BZY20 synthesised using NiO as sintering aid, shows total conductivity of 0.033 S cm^{-1} at 600 °C [33]. The cerates are the systems with higher proton conductivity, but show problems of stability versus CO_2. Doped barium zirconate has higher chemical stability but presents some problems of poor sinterability and poorly conducting grain boundaries

[122]. In order to improve this sinterability, Zn doping (<5%) in these systems was applied, allowing densification (>95% theoretical) at relatively low temperatures of 1200 °C, which is about 200 °C lower than without Zn doping [123, 124]. The largest proton conductivity and smallest activation energy have been reported so far for barium zirconate doped with 20 mol% of yttrium (BZY20) [125, 126].

High proton conductivity has also been reported for complex perovskites of the type $A_2(B'B'')O_6$ and $A_3(B'B_2'')O_9$, where A is a divalent cation, B′ is a divalent or trivalent cation respectively and B″ is a pentavalent metal, usually Nb or Ta [127, 128]. The level of oxide ion vacancies is increased by changing the concentration of the B′ ions at the expense of the B″ ions. Some examples include $A_3Ca_{1+x}Nb_{2-x}O_{9-3x/2}$,[129] $Sr_3CaZr_{0.5}Ta_{1.5}O_{8.75}$, [130] or $Sr_2Sc_{1+x}Nb_{1-x}O_{6-x}$.

Proton conductivity has also been reported in brownmillerite materials. The proton conduction in $Ba_2In_2O_5$ originates form the formation of the hydrate $Ba_2In_2O_5.H_2O$ [131]. However, high values of proton conductivity are not observed and this coupled with high instability in humid atmosphere, high reactivity towards CO_2 and easy reducibility makes the use of $Ba_2In_2O_5$ difficult in practical application [131-135]. In order to improve the conductivities of these materials various oxygen-deficient perovskite-like complex oxides have been investigated, for instance brownmillerite compositions like $A_2BB'O_5$ where B B′ are Ho-Ga, Y-Ga, Sc-In, Sc-Sc [136], $Ba_2(In_{1-x}M_x)_2O_5$ where M= Sc, Lu and Y [137], $Ba_2(Sc_{1-x}M_x)_2O_5$ where M= Lu, Yb, Tm and Er [138], $Ba_2(In_{1-x}Ti_x)_2O_{5+x}$ ($0 \leq x < 1$) [105, 139, 140], $Ba_2In_{2-x-y}Ce_xLa_yO_{5+x/2}$ (x = 0.25 and 0.5; y = 0.25 and 0.5) [141] $Ba(In_{1-x}M_x)O_{2.5+x/2}$ ($0.0<x<0.15$) (M=Zr, Ti and Hf) [142], $A_2BB'O_5$ [A= Ba, Sr, B=Zn, B′= Zr Ce Ti Hf, Sn] [143]. More recently cubic oxyanion containing phases, $Ba_2Sc_{2-x}P_xO_{5+x}$ (x = 0.4, 0.5) and its Si analogue [84] have also been reported as proton conductor.

3.4 NEW OXIDE ION AND PROTON CONDUCTING ELECTROLYTES

Fluorite and perovskite oxide ion conductors for SOFC applications have essentially reached the state of the art that is possible, consequently, in recent years, there has been a growing trend toward the investigation of alternative structure-types, for the prospect of future major advances [27]. $La_2Mo_2O_9$, first reported by Lacorre et al., shows very high conductivities (0.06 S cm^{-1} at 800 °C), exceeding that of YSZ at elevated temperatures [144]. In terms of a compromise between stability and conductivity, the composition $La_{1.7}Gd_{0.3}Mo_{0.8}W_{1.2}O_9$ has been reported to be most promising [145], with very high conductivities, higher than in the parent high temperature (β) form are also reported (0.11 S cm^{-1} at 800 °C for $La_2Mo_{1.94}Nb_{0.06}O_{8.97}$) [146].

Apatite-type oxides have an ideal general formula of $A_{10}(MO_4)_6O_2$, where A = alkaline earths, rare earths, M = Si, Ge, P and have also shown excellent oxide ion conductivities with the highest conductivity in the literature reported for the composition, $La_{9.5}(GeO_4)_{5.5}(AlO_4)_{0.5}O_2$ (0.16 S cm^{-1} at 800 °C) [27, 147]. Another material in which the accommodation of interstitial oxide ions has been shown to be possible is the layered tetrahedral network melilite structure with reported high oxide ion conductivity (σ = 0.02−0.1 S cm^{-1} between 600 and 900 °C for $La_{1+x}Sr_{1-x}Ga_3O_{7+x/2}$ (x = 0.54) [27, 148]. Mayenite with nominal composition $Ca_{12}Al_{14}O_{33}$ and BIMEVOX, where BI stands for bismuth, ME for metal, V for vanadium and OX for oxygen, are also reported as oxide ion conducting electrolyte [72]. BIMEVOX represents a relatively stable and good ion-conducting (of the order 0.1–1.0 S cm^{-1} at 600 °C) family of oxides derived from the parent oxide $Bi_4V_2O_{11}$.

While searching for more stable proton conducting materials, Haugsrud and co-workers [52, 121] came across several acceptor-doped rare-earth orthoniobates and orthotantalates of general formula $RE_{1-x}A_xMO_4$ (where RE = La, Gd, Nd, Tb, Er or Y; M

= Nb or Ta; A = Ca, Sr or Ba; and x = 0.01–0.05). Oxide ion conductors also exhibiting high temperature proton conductivity include lanthanum gallates of general formula $La_{1-x}Ba_{1+x}GaO_{4-x/2}$ and for some pyrochlore systems, especially for $La_2Zr_2O_7$-based systems, where proton incorporation is promoted by doping with lower valent cations on the A- or B-sites. Higher proton conductivities are found for zirconates doped on the A-site, i.e. the proton conductivity of $(La_{1.95}Ca_{0.05})Zr_2O_{7-\delta}$ is 6.8×10^{-4} S cm^{-1} at 600 °C; three times larger than that of the system doped on the B site, suggesting differences in the proton concentrations [149-152]. Other high-temperature proton conductors receiving attention include phosphates without structural protons , such as $LaPO_4$ [153] and solid inorganic acids showing high proton conductivities at moderate temperatures (120–300 °C) such as $CsHSO_4$ and CsH_2PO_4 [154]. Nominally undoped and Ca-doped Ln_6WO_{12} (Ln = La, Nd, Gd and Er) is also reported and investigated as a proton conductor [155]. This material transports both ions (protons and oxide ions) and electrons [156].

3.5 MIXED PROTON-ELECTRONIC CONDUCTORS, H_2 SEPARATION MEMBRANES AND PCFC ELECTRODES

Mixed ionic–electronic conductors (MIECs) [33, 53, 157-163] are materials that conduct both ions and electronic charge carriers (electrons and/or holes). Usually, high electronic and oxygen-ion conductivities are very important in solid-state electrochemical devices designed for energy conversion and gas sensing. Some important applications of MIECs include solid oxide fuel cell (SOFC) electrodes, oxygen separation membranes, insertion electrodes, electrochromic windows, oxygen sensors, gas sensors, and catalysts. In addition there is emerging interest in the possibility of developing mixed protonic–electronic conductors for hydrogen separation. On the other hand, a cathode for PCFCs necessitates taking into account of the water generation reaction. For this reason, mixed protonic/electronic conductors are favoured as cathode material for PCFCs over metals

(e.g. Pt) or mixed electronic/oxygen-ion conductors. Traditionally, high-temperature proton conductors are acceptor-doped oxides. They can exhibit mixed conduction from protons, oxygen vacancies and electron holes. Rare-earth-doped $BaCeO_3$, for example, shows contributions of all three conductivities under high humidity, high oxygen partial pressures, and at high temperature and moreover, also a mixed n-type electronic, oxygen ion and protonic conductor in H_2+H_2O atmospheres. The p-type electronic conductivity depends on the valence states of the cations involved, but usually it decreases rapidly with decreasing oxygen activity. Some HTPCs can also exhibit electronic n-type conduction under sufficiently reducing conditions. To achieve considerable n-type conduction, the oxides should contain an easily reducible cation. For HTPCs or hydrogen separation membranes, n-type conduction will be relatively more important than the p-type conduction often encountered in. A good candidate cathode material for a proton -conducting electrolyte should exhibit high electrical conductivity, large electrode – electrolyte–air triple phase boundary (TPB) length, adequate porosity for gas transport, good compatibility with the electrolyte, and good catalytic activity for the following electrode reaction

$$4H^+ + O_2 + 4e^- \rightarrow 2H_2O$$

Now it is observable that protonic, oxygen-ion, p-type and n-type electronic conductivities are strongly governed by external parameters, such as temperature, gas atmosphere, and oxygen and water partial pressures. In general, appreciable electronic conductivity confines the application as electrolyte materials because it decreases the cell open-circuit voltage. Nonetheless, Fabbri et al. [8] emphasized the importance of mixed protonic-electronic conduction as anode or cathode materials for a proton -conducting electrolyte based SOFC.

3.6 Structure and Defect Chemistry of Doped Barium Zirconate and Titanate

3.6.1 Perovskite Structure

Although the name perovskite was originally used to describe the rare mineral $CaTiO_3$, it is commonly used today to describe a more general group of oxides with a similar crystal structure. The perovskite structure has the general formula ABO_3, where the A-cation is a metal with a +2 or +3 charge and the B-cation with a +4 or +3 charge, respectively. Here the A-site cations are typically larger than the B-site cations and of the similar size of O-site anions.

The perovskite structure (see Figure 3.1) is built on BO_6 octahedra in 3 dimension spaces, while the AO_{12} cubooctahedra fills the spaces in the octahedra. The ideal structure can be of three different structural degrees of freedom (a). displacement of cations A and B from the centers of their cation coordination polyhedra, AO_{12} and BO_6 (b). distortions of the anionic polyhedra coordination around A and B ions, (c). tilting of the BO_6 octahedra about one , two or three axes.

The real structures of perovskites depend on the relative size of the A and B ions. When the ratio of the ionic radii differs too much distortions occur of which octahedra tilting is the most common one. With perovskite tilt the BO_6 octahedron twist along one or more independent axes to accommodate the radius-difference. The Goldschmidt tolerance factor (t) is used as guide to determine the possibility of formation of perovskite structure with a given composition in a particular temperature and pressure. For ideal perovskite, the tolerance factor is expressed as

$$t = \frac{r_A + r_O}{\sqrt{2}(r_B + r_O)} \tag{3.1}$$

In the ideal cubic structure, t is unity, though the perovskite structure can form for values of t between 0.8 and 1.10, but with lower symmetry. The role in determining the space group or structure adopted is not unambiguously guided by the tolerance factor.

Factors other than ion size such as degree of covalency, metal-metal interactions, Jahn-Teller and lone pair effects, also contribute in structure determination. As the value of t decreases, the structure of the unit lattice is shifted from cubic to triclinic as a result of the increased distortions [164].

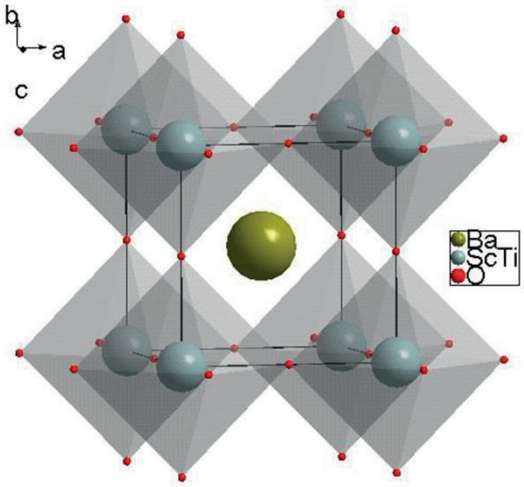

Figure 3. 1 The structure of the ABO_3 perovskites. A cation (Ba^{2+}) at the centre of a cubooctahedra, while B site cation (Ti^{4+}) at the centre of BO_6 polyhedra can be partially replaced by a lower valance cation (Sc^{3+}). Charge balance, creates some oxide ion vacancy, thus creating oxygen deficient perovskites.

The stability and the crystal group are mainly determined by the ratio of the ionic radii of the A and B cations. Indeed, the structure is dependent not only on the size but also on the nature of the A and B atoms [164] . If a B-site cation is progressively replaced by a dopant, a large difference in ionic radii tends to lead to the formation of the superstructures rather than random arrangements of the two kinds of ions. In complex mixed perovskites of the type $A_2(B'B'')O_6$ and $A_3(B'B'')O_9$ there can be random distribution of B' and B'' ion in the octahedral positions or a superstructure with hexagonal lattice is observed.

Other typical polymorphs of the perovskite structure are Brownmillerite ($A_2B_2O_5$) and K_2NiF_4 structures. Brownmillerite ($A_2B_2O_5$) is an oxygen deficient type of perovskite in which the oxygen vacancy is ordered. The unit cell contains BO_6 and BO_4 units in an ordered arrangement. Because of the oxygen deficiency, the coordination number of the A-site cations decreases to 8. The lattice parameter of the Brownmillerite structure relates to the cubic lattice parameter (a_p) of the ideal perovskite as $a=b=\sqrt{2}\ a_p$, $c= 4a_p$. Based on the intergrowth of the different numbers of Perovskite $KNiF_3$ and rock salt KF units, there are many structures called Ruddelsden-Popper compounds with the general formula $(ABO_3)_nAO$: for example $Sr_3Ti_2O_7$ (n=2), $Sr_4Ti_3O_{10}$ (n=3).

Because of the variety of structures and chemical compositions, perovskite oxides display a large range of properties. Well-known properties of the perovskite oxides are ferroelectricity in $BaTiO_3$ -based oxides and superconductivity in $YBa_2Cu_3O_7$, etc. In addition to these, several perovskite oxides exhibit high electrical conductivity, which is close to that of metals, and ionic conductivity, as well as mixed ionic and electronic conductivity. Based on these variations in electrical conducting properties, perovskite oxides are chosen as the components for SOFC [164]. It is also well known that several perovskite oxides exhibit high catalytic activity.

3.6.2 Defect Chemistry and hydration thermodynamics

All crystalline solids above 0 K will exhibit deviations from the ideal structure. Thus all inorganic compounds may, in principle, have variable composition and thus be nonstoichiometric. These deviations or imperfections are called defects [165].

Defects can be of zero to three dimensional. When the imperfection is restricted to one structural or lattice site and its nearby vicinity, it is a zero dimensional imperfection or a point defect. For example vacancies, interstitial atoms, impurity atom in crystal are point defects. Displacements or dislocation in the structure in certain directions is called line defects or 1-dimensional defects. 2-dimensional or plane defects consist of stacking faults, grain boundaries, internal interfaces and external surfaces. A three-dimensional

defect such as precipitations extends in all directions. In addition to these structural defects, a crystal may comprise electronic defects; electrons and holes. Only point defects, electronic defects and grain boundaries are considered to be significant for this thesis.

Protons are positively charged hydrogen ions (H^+). They have no electrons in their shell and are of relatively very small in sizes compared to other elements. So they cannot usually occupy a lattice or normal interstitial site. Consequently it is important for oxides to have defects in order to incorporate protons. Protonic defects in oxides occur typically through the formation of oxygen vacancies and their subsequent filling by exposure to humid or hydrogen atmosphere at elevated temperature [53, 61, 114, 115]. However, during the synthesis of the oxides, protons may also dissolve as a charge compensator for dopants. Thus oxygen vacancies are not strictly necessary [111]. By changing the ratio of the main constituents of perovskite, vacancies may be formed e.g. $Ba_3Ca_{1+x}Nb_{2-x}O_{9-\delta}$ [127], $Ba_2YSnO_{6-\delta}$ [166]. This type of defects can be termed as intrinsic defect, since no foreign elements or ions are introduced in the system. Generally the defects in perovskites are of Schottky type (Figure 3.2 a) which is a stoichiometric defect having a pair of vacant sites, an anion vacancy and a cation vacancy [50, 51, 52]. In case of Frenkel type defects (Figure 3.2 b) oxygen interstitials are required.

A comprehensive treatment of the defect chemistry of solids along with various approximate methods to solve systems of nonlinear equations of the solid-state equilibria governing the defect concentrations is found in literature [167-170]. The vacancy may be formed extrinsically to compensate for a lower valance acceptor dopant on either the A- or B-site. In the perovskite structure acceptor doping can be performed by the partial substitution of B^{4+}-site with a +3 cation or the substitution of the A^{2+}-site with a +1 cation. Specifically, for barium zirconate, the zirconium (B^{4+}-site) is partially substituted with a trivalent yttrium to create oxygen vacancies. With a significant dopant concentration, extrinsic oxygen vacancy defects are the dominant species. The doping

reaction for an acceptor Mf on the B site of a II–IV perovskite ABO_3 in dry atmospheres can be written as follows [78]

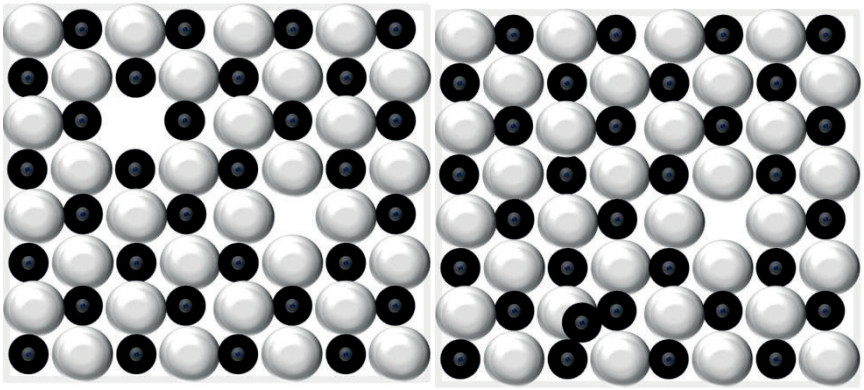

(a) **(b)**

Figure 3.2 Schematic presentations of different types of point defects in ionic crystal (a) Schottky type (b) Frenkel type, adapted from [171].

$$Mf_2O_3(s) + 2AO(s) = 2A_A^{\times} + 2[Mf_B^{/}] + 5[O_O^{\times}] + 2[v_O^{\bullet\bullet}] \quad (3.2)$$

where $A_A^{\times}$ is the A^{2+} metal ion at its original position (effective charge =0), $O_O^{\times}$ is the oxygen ion at its position (effective charge =0), Mf_2O_3 is the foreign metal oxide used for doping, $[Mf_B^{/}]$ is the M^{3+} dopant ion at the B site (acceptor) (effective charge is – 1), $v_O^{\bullet\bullet}$ is the oxygen vacancy (effective charge = +2).

Hydrogen is a donor in oxides and usually be ionized to a proton. This proton will be located in the electron cloud of an oxide ion, such that the species is a hydroxide ion on the site of an oxide ion, being effectively positive and in Kröger–Vink [172] notation written as $OH_O^{\bullet}$. This protonic defect can also be written as an interstitial proton $H_i^{\bullet}$, although the interstitial site is not a regular one. In hydrogen or water saturated atmospheres, hydroxyl ion compensate the acceptors and contribute to the protonic conductivity. Proton incorporation is found to be an exothermic reaction [61, 78]

$$H_2O(g) + O_o^{\times} + v_O^{\bullet\bullet} = 2[OH_O^{\bullet}] \quad (3.3)$$

$$K_3 = exp\frac{\Delta S_3^0}{R} exp\frac{-\Delta H_3^0}{RT} = \frac{[OH_O^\bullet]^2}{[O_O^\times][v_O^{\bullet\bullet}]P_{H_2O}} \quad (3.4)$$

Where K_3 is the equilibrium constant of hydration reaction, ΔS_3^0 and ΔH_3^0 are the standard hydration entropy and enthalpy respectively. The two positively charged protonic defects formed can diffuse into the bulk of the oxide but this requires the diffusion to be accompanied by a counter diffusion of oxide ion vacancies [61]. This indicates that an oxide displaying proton conductivity also exhibits some oxide ion conductivity in the dry state. Hence, the oxide will have an ambipolar diffusion of $v_O^{\bullet\bullet}$ and $[OH_O^\bullet]$.

Alternatively, equilibrium constant K_3, of the hydration reaction can be expressed as $kTlnK_3 = T\Delta S_3^0 - \Delta H_3^0$ [173]. Here all the concentrations are given in the same units, so that the standard concentrations cancel, and the partial pressure of water is in bars. The electroneutrality condition in this case is [78] :

$$2\left[v_O^{\bullet\bullet}\right] + [OH_O^\bullet] = \left[Acc^/\right] = constant \quad (3.5)$$

where $Acc^/$ denotes acceptors in general. Electroneutrality is comprised of volume or molar concentrations, not site fractions. One of the limiting cases where protons dominate (i.e. at low temperatures), acceptors become frozen in or being all dissolved so that varying solubility of protons is not effective and can be approximately is [78]

$$[OH_O^\bullet] \approx \left[Acc^/\right] = constant \quad (3.6)$$

On the other hand, if protons are minority as such

$$2\left[v_O^{\bullet\bullet}\right] \approx \left[Acc^/\right] = constant \quad (3.7)$$

Then the proton concentration (assuming condition 3.7) becomes [78]:

$$[OH_O^\bullet] = \sqrt{\left(K_3[O_O^\times][v_O^{\bullet\bullet}]P_{H_2O}\right)} =$$

$$\sqrt{[Acc^/]\left([O_O^\times]P_{H_2O}\right)}\, exp\frac{\Delta S_3^0}{2R} exp\frac{-\Delta H_3^0}{2RT} \quad (3.8)$$

Assuming, small defect concentrations, $[O_O^{\times}]$ equals the concentration of oxide ion sites, and for molar concentrations this is equal to 3 in perovskites. An analytical solution to the full electroneutrality is obtained by combining the equilibrium expression with the electroneutrality condition and assuming $\left[O_O^{\times}\right] = [O] = constant \gg 2\left[v_O^{\bullet\bullet}\right] + [OH_O^{\bullet}]$, the proton concentration becomes

$$[OH_O^{\bullet}] = \frac{\left(K_3[O]P_{H_2O}\right)\left(-1+\sqrt{1+\frac{8\left[Acc/\right]}{\left(K_3[O]P_{H_2O}\right)}}\right)}{4} \tag{3.9}$$

If we instead assume the more general condition

$[O_O^{\times}] + \left[v_O^{\bullet\bullet}\right] + [OH_O^{\bullet}] = [O] = constant$ Then we obtain the concentration of protons:

$$[OH_O^{\bullet}] = \frac{\left(K_3P_{H_2O}[O]\right)\left(-1+\sqrt{1-\frac{2\left[Acc/\right]}{[O]}+\frac{\left[Acc/\right]^2}{[O]^2}+\frac{8\left[Acc/\right]}{\left(K_3P_{H_2O}[O]\right)}-\frac{4\left[Acc/\right]^2}{K_3P_{H_2O}[O]^2}}\right)}{4-K_3P_{H_2O}} \tag{3.10}$$

However, factors such as non-stoichiometry, atmosphere, dopant size, etc. complicate the defect reactions. Firstly, the existence of Ba^{2+}-site substitution has been proposed by theoretical calculations for large dopants such as La and Sm [174]. In the presence of oxygen, acceptor-doped oxide ion vacancies may be charge compensated via the absorption of oxygen to produce electron holes as described in equation 3.11a below.

$$½O_2(g) + v_O^{\bullet\bullet} \rightarrow O_O^{\times} + 2h^{\cdot} \tag{3.11a}$$

At low partial pressures, oxygen can also desorb from the lattice, forming electronic defects:

$$O_O^{\times} \rightarrow ½O_2(g) + v_O^{\bullet\bullet} + 2e^{/} \tag{3.11b}$$

This reaction (equation 3.11a) competes with the formation of $[OH_O^{\bullet}]$ defects described in equation 3.3. From the equilibrium equations given below for reactions 3.3

and (3.11a), it is apparent that protonic and p-type electronic conductivity depends respectively on the water vapour pressure and oxygen partial pressure [82, 111]:

$$[OH_O^{\bullet}] = K_3[V_O^{\cdot\cdot}]^{½}(P_{H_2O})^{½} \quad (3.12)$$

$$[\rho] = K_{11}[V_O^{\cdot\cdot}]^{½}(P_{o_2})^{¼} \quad (3.13)$$

where K_3 and K_{11} are the equilibrium constants of Eq.(3.3) and (3.11a), $[\rho]$, $[OH_O^{\bullet}]$ and $[v_O^{\bullet\bullet}]$ are the concentration of electron holes, protons and oxygen vacancies, P_{o_2} and P_{H_2O} are the oxygen and water vapor partial pressures.

Thus, generally, perovskite-type compounds can have facile electronic conduction, thus ionic conduction is often supplemented by electronic conduction. The concentration of the electronic defects depends on the deviation of cation and/or anion ratios. Contribution of electronic conduction varies with the conditions such as the degree of deviation from their stoichiometric ratios, the content of impurity, atmosphere and temperature. As already seen in equations (3.13) electronic conductivity of an oxide electrolyte at elevated temperature is influenced by partial pressure of oxygen, P_{o_2}. n-type electronic conductivity, σ_n increases with decreasing P_{o_2}, whereas p-type electronic conductivity σ_p increases with increasing P_{o_2}. In general they are expressed as [175]

$$\sigma_n = \sigma_n^0 exp P_{O_2}^{-1/n} \quad (3.14)$$

$$\sigma_p = \sigma_p^0 exp P_{O_2}^{1/n} \quad (3.15)$$

where n is some natural number, and σ_n^0 and σ_p^0 are the constants that are independent of the partial pressure of oxygen [175]. The relationship is illustrated in Figure. 3.3.

It is accepted that the ionic conductivity, σ_i, itself is independent of P_{o_2} for many oxide electrolytes. Accordingly, the total conductivity σ is expressed as follows [175]:

$$\sigma = \sigma_i + \sigma_n^0 exp P_{O_2}^{-1/n} + \sigma_p^0 exp P_{O_2}^{1/n} \quad (3.16)$$

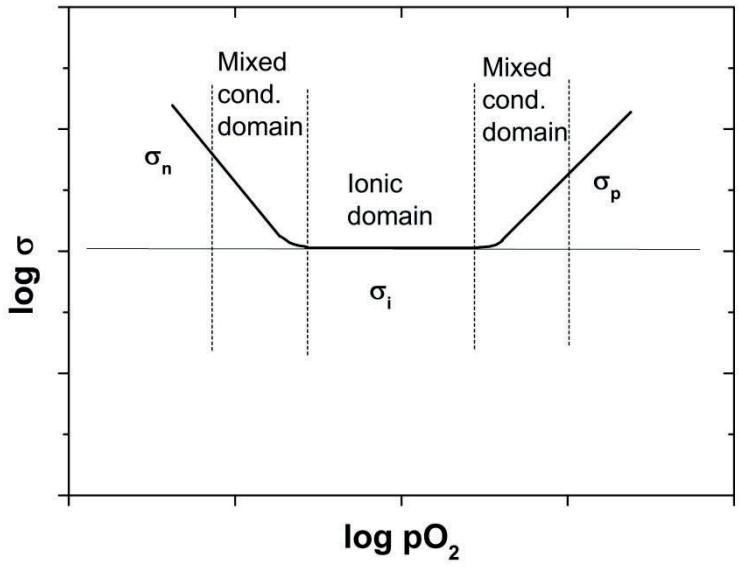

Figure. 3.3 Dependence of conductivity on partial pressure of oxygen reproduced from [175].

The equilibrium constant and its thermodynamic parameters in equation 3.4 are important because they determine whether the material is primarily dominated by oxygen vacancies or protons. Based on the loss of one mole of $H_2O(g)$ in reaction 3.3, the entropy of hydration, is expected to be approximately -120 J/mol K and experimental values of -120 ±40 J/mol K are found [78, 176]. The enthalpy of this reaction, ΔH_3^0, varies widely. When the enthalpy of hydration is negative the resulting acceptor-doped oxide will be dominated by protons at low temperatures and oxygen vacancies at high temperatures. For more negative hydration enthalpy materials, it takes a higher temperature to shift the equilibrium to the left in equation 3.3. The transition temperature between the defect situations is determined by ΔH_3^0, ΔS_3^0, $\left[Acc^{/}\right]$ and P_{H_2O} where, ΔH_3^0 is the most important factor [177].

To be able to predict the concentration and conductivity of protons in a material, correlations between hydration thermodynamics and materials properties

have been searched for. According to Kreuer, more negative hydration enthalpy is in the order Sr→ Ba and Nb→ Zr→ Ce, Er for the occupation of A- and B-site of perovskite-type oxides [178]. The more negative hydration enthalpy was explained by the increase in the basicity of the lattice oxygen, i.e. basic oxides form the strongest OH bonds. Moreover, it is shown that hydration enthalpy for perovskite-type oxides become more negative in the order:

titanates → niobates → zirconates → stannates→ cerates,

Thus supporting the general observation that the basicity of the oxide is an important factor for the hydration enthalpy. The enthalpy of the hydration reaction tends to become more exothermic with increasing Bronsted basicity of the oxide, i.e. with decreasing electronegativity of the cations interacting with the lattice oxygen [173, 178]. Norby expanded on the correlation idea of Kreuer by suggesting a correlation between the hydration enthalpies and the difference in the electronegativities of A- and B-site cations [111]. The most negative hydration enthalpies have been reported for perovskites with similar electronegativities of A- and B-site cations.

Figure 3.4 shows the standard enthalpy of hydration for a number of perovskite-related oxides as a function of the difference in the electronegativity of the A- and B-site cations. The best linear fit of these data points yields as a first or rough approximation:

$$\Delta H_3 = 370\Delta\chi_{B-A} - 173 \qquad (3.17)$$

where Allred-Rochow electronegativities [179] are used. Further investigations done by Bjørheim *et al.* [180], on systems, where the A-cation is more electronegative than the B-cation, such as $PbZrO_3$, show that it is necessary to use the absolute value of the electronegativity difference. Since the electronegativity is related to the covalent radius of an atom, Norby et al. have suggested a correlation between the Goldschmidt tolerance factor (degree of distortion) and the hydration enthalpy [176].

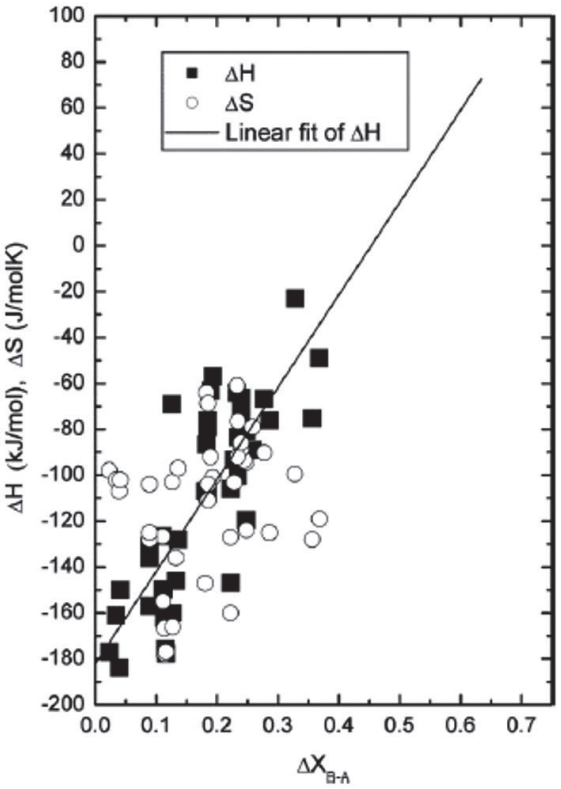

Figure 3.4 Apparent relationships between the hydration enthalpy and the difference in electronegativity between the B- and A-site cations. The electronegativities are in the Allred-Rochow scale and the figure is taken from [111] with permission.

A perovskite with large electronegativity difference would have a Goldschmidt tolerance factor close to unity (high-symmetry structures), and the hydration enthalpy will decrease with decreasing tolerance factor.

3.7 ELECTRICAL CONDUCTIVITY IN CERAMIC OXIDES

Electrical conductivity is the net transport of various charge carriers under an electric field. As we have seen ceramic oxides can exhibit both electronic and ionic

conductivity. Electronic conductivity comprises transport of electrons (n-type) and holes (p-type) whereas ionic conductivity involves transport of ions (e.g., oxygen ions and/or protons) through the solid. Total electrical conductivity, σ, of a conducting oxide is the sum of the partial conductivity accompanying with each type of charge carrier, j and is assumed by:

$$\sigma = \sum_j \sigma_j = \sigma_e + \sigma_i = \sigma_n + \sigma_p + \sigma_{i^+} + \sigma_{i^-} \quad (3.18)$$

Here, units of partial conductivities are expressed in $\Omega^{-1}cm^{-1}$ or Scm^{-1} and σ_e, σ_i , σ_n, σ_p, σ_{i^+}, σ_{i^-} denote the conductivity contribution from electronic charge carriers, ionic charge carriers, electrons , holes , anions, and cations, respectively.

Transport number, t_j is the fraction of the total conductivity contributed by each charge carrier:

$$t_j = \frac{\sigma_j}{\sigma} \quad (3.19)$$

When an electric field, E, is applied to a sample, charged species will be subject to a force proportional to both the electric field and the charge of the species. This force gives rise to a net current density, i_j, which is then given by

$$i_j = z_j e c_j u_j E = \sigma_j E \quad (3.20)$$

Where σ_j is the partial conductivity of the charge carrier of species, j. c_j is the concentration of charge carrier j (number per unit volume). u_j is the charge mobility (drift velocity in a constant electric field, $m^2s^{-1}V^{-1}$) and $z_j e$ represents charge (expressed as a multiple of the charge of an electron, e =1.602189 x 10^{-19}C). The concentration parameter, c_j depends on atmosphere and chemical composition of the oxide, while the charge mobility u_j is usually a function of temperature only. The charge mobility of an ion is related to its mechanical mobility, B_j, (the drift velocity of an ion per unit of applied electric force, $m^2s^{-1}C^{-1}V^{-1}$) and its diffusion coefficient through the solid, D_j, by the following relationship:

$$u_j = z_j e B_j \quad (3.21)$$

$$D_j = k_B T B_j \quad (3.22)$$

Where k_B=1.381 x 10^{-23} J/K is the Boltzmann's constant, T is temperature (K), D_j is the diffusion coefficient (cm^2s^{-1}), and B_j is the mechanical mobility ($m^2s^{-1}C^{-1}V^{-1}$). Combining equations 3.20, through 3.22, we obtain, the so called Nernst-Einstein equation as.

$$u_j = \frac{z_j e D_j}{k_B T} \tag{3.23}$$

$$\sigma_j = \frac{c_j (z_j e)^2 D_j}{k_B T} \tag{3.24}$$

Again, the Arrhenius equations for the case of ionic conductors, is expressed in terms of the temperature dependence of the charge mobility and ionic conductivity as:

$$u_j = \frac{u_{j,0}}{T} \exp \frac{-E_j^F}{k_B T} \tag{3.25}$$

$$\sigma_j = \frac{\sigma_{j,0}}{T} \exp \frac{-\left(E_j^F + E_j^M\right)}{k_B T} \tag{3.26}$$

where $u_{j,0}$ is a proportionality constant that depends on attempt frequency (probability that an ion will attempt to break the bond and leave its current position in a structure), the distance moved by the atom, and the size of the external field. $\sigma_{j,0}$ is a proportionality constant that involves c_j and $z_j e$, and also depends on the attempt frequency and jump distance. E_j^F and E_j^M are the energies for charge carrier formation and migration, respectively. An Arrhenius-type temperature dependency is common in the ionic and the electronic conductivities of any ionic compounds.

In general, the temperature dependence of the electrical conductivity is given by the Arrhenius equation:

$$\sigma = \frac{\sigma_0}{T} \exp\left(\frac{-E_a}{k_B T}\right) \tag{3.27}$$

Where E_a is the activation energy for formation and transport of the charge carriers. This expression is often expressed as:

$$ln\sigma T = ln\sigma_0 + \left(\frac{-E_a}{k_B T}\right) \tag{3.28}$$

And plotted as lnσT against 1/T, which produces a straight line with a slope of$-E_a$.

3.8 CHEMICAL STABILITY

Empirically high thermodynamic stability and high proton conductivity still seem to exclude one another [173]. Although the cerate based compounds show high proton conductivity for given water partial pressure but below 700 °C they react even with air to form carbonates. On the other hand preferentially basic oxides stabilize protonic defects, hence acidic gases such as CO_2 and SO_2, are not compatible with these basic oxides [61].

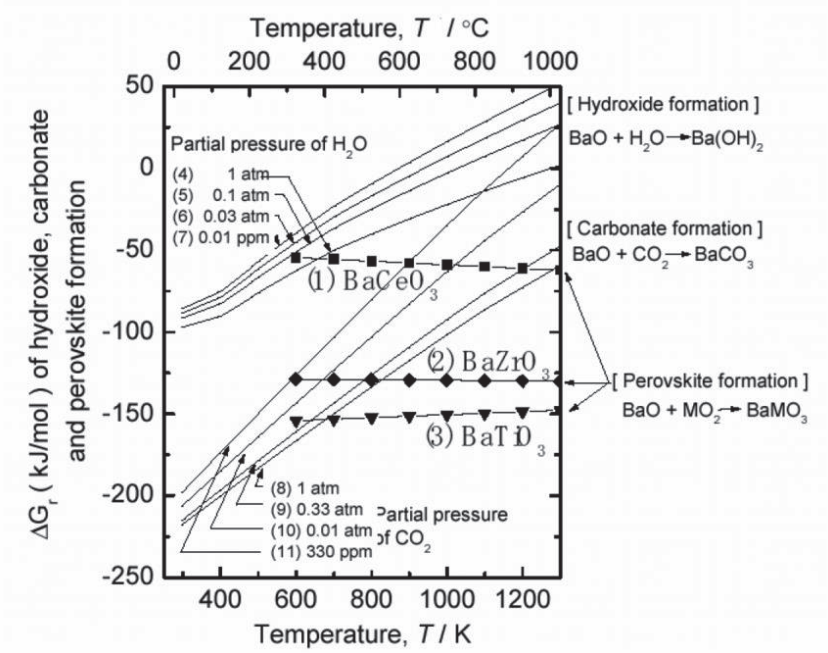

Figure 3.5 Gibbs energy of formation of barium hydroxide, barium carbonate, and perovskite from constituent oxides taken from [181] with permission.

$$BaCeO_3 + CO_2 \rightarrow BaCO_3 + CeO_2 \quad (3.29)$$

$$BaCeO_3 + H_2O \rightarrow Ba(OH)_2 + CeO_2 \quad (3.30)$$

This reactivity causes severe degradation of the material and precludes applications in electrochemical devices in severe conditions, such as a fuel cell based on hydrocarbon fuels. In contrast, barium zirconate exhibits excellent stability under CO_2 [120] rendering it highly attractive for applications in aggressive environments. Figure 3.5 shows the Gibbs energy of formation of barium hydroxide, barium carbonate, and the formation of the perovskite from oxides [181].

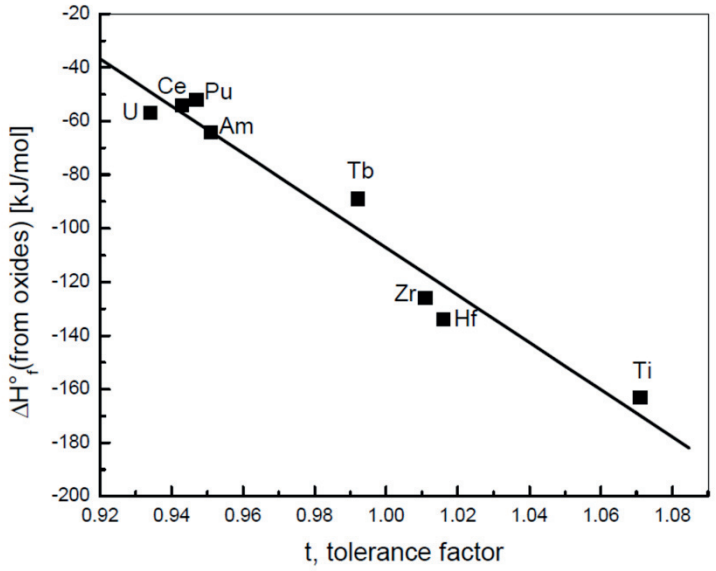

Figure 3.6 Tolerance factor vs. formation enthalpy of Ba-based perovskite compounds, with B-site cation listed on the plot, taken from [182].

$BaCeO_3$ exhibits relatively high formation energy, compared to $BaTiO_3$ and $BaZrO_3$. For the perovskite to be stable, the Gibbs energy of perovskite formation must be lower than both the formation energy of the hydroxide and carbonate. The barium zirconate system is stable against the hydroxide formation at all given water partial pressures and temperatures. Below ~530 ºC in pure CO_2 (1atm), decomposition reaction of barium zirconate is thermodynamically expected, however, slow kinetics allow the

system to maintain its stability. The stability with respect to the formation of carbonates and hydroxides increases in the order: cerate > zirconate > titanate, i.e., opposite to the direction of the stability of protonic defects.

Additionally, in order to better describe the formation of a perovskite, enthalpy of formation from the oxides can be calculated from the heats of solution which are determined experimentally by several groups. Navrotsky et al. [183] have shown that the heat of formation from oxides of perovskite compound vary in a nearly linear relation with the value of the Goldschmidt tolerance factor t, Figure 3.6 illustrate this relationship with Ba-based perovskites.

3.9 PROTON TRANSPORT

The protons are located on oxide host ions and exhibit thermally activated rotational and stretching vibrations. They can be found in a variety of local energy minima, subject to which neighbouring oxide ion(s) they are directed towards. Depending on the O–O distance, the protons may set up hydrogen bonds, OH–O, between the two oxide ions, this decreases their distance somewhat, and affects the structure [78]. It was found that the hydrogen transport belongs to free proton migration [184, 185] called the Grotthuss mechanism. In addition, the isotope effect also indicates that the hydrogen ion conduction is free proton transport rather than hydroxide transport [184] (see Figure 3.7).

The Grotthuss mechanism consists of reorientation of the OH^- ion followed by hopping of the proton from one O^{2-} to an adjacent O^{2-} site to give the hopping or proton transfer 'reaction' [184]. This Grotthuss mechanism is different from the transport of hydroxyl ions as a whole. The latter is termed a vehicle mechanism of transport and is commonly encountered in aqueous solution and other liquid-like membranes. In solids, the vehicle mechanism is restricted to materials with open structures to allow for the

passage of ions and molecules. An example of the vehicle mechanism includes polymer membranes, in which the vehicular mechanism is used to transport protons in a H_3O^+ ion.

$$OH\text{--}O \rightarrow O\text{-}H\text{-}O \rightarrow O\text{--}HO \qquad (3.31)$$

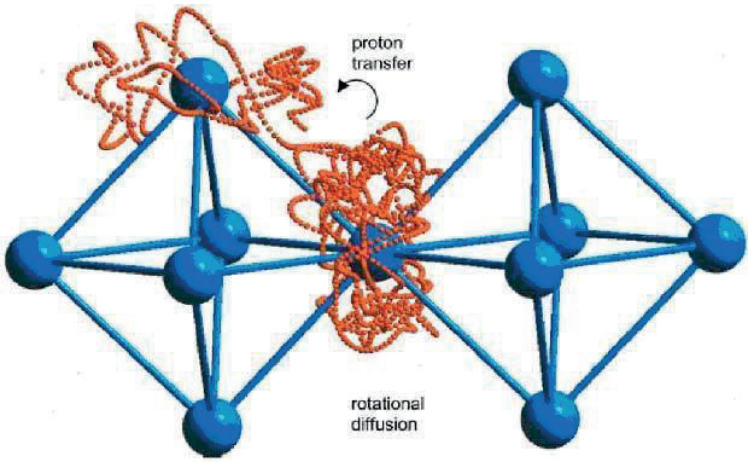

Figure 3.7 Proton transport in a perovskite; featuring both the rotational diffusion and proton transfer based on molecular dynamic simulations, taken from [61] with permission.

Kreuer [61] describes the proton transfer reaction as the rate-limiting step for proton transport in perovskites. However, at the same time their study on the proton environment using the IR technique, points to strong hydrogen bond interactions, favouring fast proton transfer instead of fast reorientations. These contradicting observations are explained by a dynamical oxygen lattice.

Most perovskite-type oxides usually have larger structural oxygen distance than the distance required for creating strong hydrogen bonds. Therefore there is a trade-off between the free energy gained by the hydrogen bond formation with the free energy required for the lattice distortion necessary for hydrogen bonding. By way of this, short oxygen separations (favouring proton transfer) and large oxygen separations (allowing rapid hydrogen bond breaking) have similar probabilities of occurring.

Simulations show that the protonic defects produce short but transient hydrogen bonds with all the nearest surrounding oxygen ions. Over time this leads to a slight reduction of the structural OH--O separations giving an average configuration. Over a short time interval the structural OH--O separations are reduced as a result of hydrogen bonding corresponding to an instant configuration. Figure 3.8 shows both the average and the instant configuration. The transient hydrogen bond reduces the OH--O separation from 312 pm (for cubic) to an average of 281 pm [173].

The proton makes the jump to the neighbouring oxygen ion only when the OH--O distance is momentarily short [186]. Therefore, a dynamic host oxygen sublattice is favourable for both proton transfer and rotational diffusion. The simulation results also show that the proton locally "softens" the lattice to allow the transient formation of hydrogen bonds followed by the proton transfer between adjacent oxygen ions [174, 187-190].

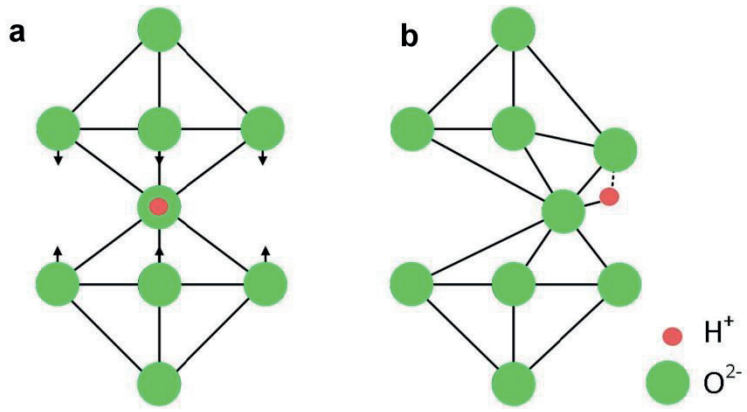

Figure 3.8 Average (a) and instant (b) configuration of dynamic hydrogen bonding, adapted from [61, 176].

3.10 ISOTOPE EFFECT

An isotope effect is visualized when: any physical property that depends directly or indirectly on the mass of the ions building up the lattice of a material is influenced. Exchanging an element by one of its isotopes (e.g., ^{16}O with ^{18}O) leads to an alteration in

the value such as vibration frequency. Soon-after the discovery of deuterium (heavy hydrogen) by Harold C. Urey in 1931, the isotope effect was developed as a tool to elucidate the hydrogen involved reaction mechanism. The isotope effect is used to confirm protonic conductivity in solid oxide conductors. In this part a brief introduction to the isotope effect in proton conductors and the principal theories involved in understanding the effect is given.

When an oxide exhibits proton conductivity, a decrease in the conductivity is observed when switching from a hydrogen-containing atmosphere (H_2 or H_2O) to a deuterium-containing atmosphere (D_2 or D_2O). This is commonly referred to as the isotope effect [169, 184, 191-194] and is linked to the large mass ratio of the respective hydrogen isotopes.

Different theories have been developed to understand the mechanism of isotope effect, such as classical theory, semi-classical theory, tunnelling theory and escape theory. The classical theory is adopted first to describe the isotope effect due to the influence of the pre-exponential term in equation 3.27. The proton (or deuteron) "hops" from one lattice site to another over a potential energy barrier, as a function of the configurational coordinate. The conductivity can be related directly to diffusion through the Nernst-Einstein relation as in equation 3.23: $\sigma_j = \frac{c_j (z_j e)^2 D_j}{k_B T}$

where D_j is the self-diffusion coefficient of the defect species *j*, k_B is the Boltzmann constant. The self-diffusion coefficient of the defect species is proportional to the frequency of sufficiently energetic jump attempts, ω, which again is proportional to the vibration frequency, ν. In the case where ν is only the OH stretching frequency, a simple harmonic oscillator approximation can be used, giving [182]:

$$\nu = \frac{1}{2\pi}\sqrt{\frac{k}{\mu}} \tag{3.32}$$

where k is the spring constant of the bond (O-H or O-D in this case) and μ is the reduced mass. Alternatively, $\nu \propto 1/\sqrt{m}$ where m is the effective mass. Therefore the $\sigma_0 \, is \; \propto 1/\sqrt{m}$ and conductivity will be written as

$$\sigma = \frac{\sigma_0}{T} \exp\left(\frac{-E_a}{k_B T}\right) \propto \frac{1}{\sqrt{m}} \exp\left(\frac{-E_a}{k_B T}\right) \tag{3.33}$$

In the classical model, the activation energy is constant therefore the effective mass is the only parameter that affects the conductivity. The heavier mass of deuteron ($OD_O^{\bullet}$) compared with hydrogen ($OH_O^{\bullet}$) leads to a lower conductivity which contributes to the observable isotope effect.

$$\sigma_{OH_O^{\bullet}} = \sqrt{2}\sigma_{OD_O^{\bullet}} = 1.414\sigma_{OD_O^{\bullet}} \tag{3.34}$$

However, the activation energy, E_a, has its contribution to the isotope effect. Semi-classical theory, which takes the zero-energy difference into consideration, is adopted here. In most cases, the activation energy is different for hydrogen and deuteron with $E_D > E_H$ [169, 195] as described in Figure 3.9, which makes the difference in conductivity more observable.

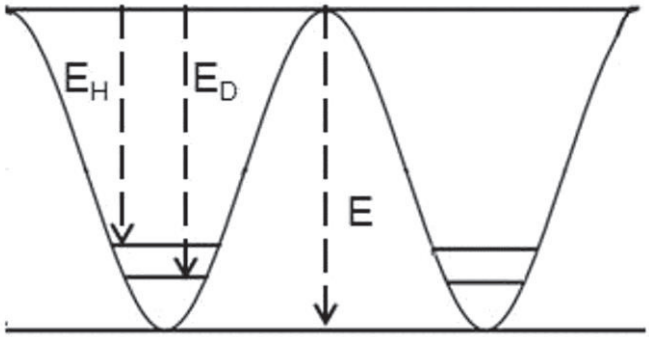

Figure 3.9 Semi-classical treatments of a proton and deuteron in a finite potential well. The existence of different zero-point energies of the two species results in an activation energy for D^+ migration that is about 5 kJ/mol higher than for that for H^+ (adapted from [169, 184]).

3.11 FACTORS DETERMINING CONDUCTIVITY: DEFECT–ACCEPTOR INTERACTIONS AND CRYSTAL SYMMETRY

There are many factors which determine the perovskite as a suitable electrolyte material in the HTPCs. In addition to lattice conductivity, some other factors also to be taken account into. One factor is the grain boundary blocking effect, which depends on grain structure and depends on sample processing. Another factor is the appearance of electronic defects at high or very low oxygen partial pressures. However, the bulk or lattice conductivity is most interesting from a fundamental viewpoint when attempting to understand the nature of the proton transport process. The incorporation of protons is seemingly independent of acceptor dopant concentration as long as the dopant does not affect the electron density of the lattice oxygen. Oxygen vacancies and/or protons sometimes can be effectively associated to acceptor dopant ions. Eventually, protons tend to be trapped by acceptors, importantly at low temperatures.

In order to migrate, the protons need to obtain an extra enthalpy, to dissociate from such trapped, local bound states. Kreuer *et al.* [126] found that $BaZrO_3$ doped with the same amount of Y^{3+} and Sc^{3+} had differences in activation energy and bulk conductivity. Oxide ions coordinated to Sc^{3+} becoming more electron rich (basic), than Y^{3+} and thus binds or traps protons more strongly. Hence, Sc:$BaZrO_3$ shows moderately higher activation energy but significantly lower conductivity than the Y doped sample.

Usually, for an oxygen-ion conducting electrolyte, dopants with ionic radius close to that of the substituted element are preferred to improve their conductivity [15] though for proton conducting electrolytes such a strong correlation is not observed [126, 173, 196]. For example even though the ionic radii of six-coordinated Sc^{3+} (0.745 Å) and In^{3+} (0.8 Å) match very well with the ionic radius of Zr^{4+} (0.72 Å), while the ionic radius of Y^{3+} (0.9 Å) is significantly larger [197], BZY shows much larger proton conductivity than Sc or In-doped barium zirconates [126, 173, 196]. Recently, Yamazaki et al. [198] and Ahmed et al. [199, 200] found that the proton uptake increases with dopant

concentrations. A larger proton concentration can be achieved in the $BaZr_{1-x}Y_xO_{3-\delta}$ ($0 < x < 0.7$) powders with high x but increasing the dopant content more than 20 mol% is not beneficial for improving the proton conductivity [125].

These results indicate optimising the proton conductivity is a complex interplay between proton concentration and mobility. The highest proton conductivities are observed for perovskite-type oxides. Parameters crucial for high proton conductivity in perovskites, include, highest molar volume (lattice constants), and little deviation from the ideal cubic perovskite structure. The highest mobilities of protonic defects have been observed for cubic perovskite-type oxides (ABO_3) so far [173]. This structure is characterized by a three-dimensionally linked framework of corner-sharing BO_6 octahedra with the A-cation in 12-fold coordination and the oxygen being surrounded by eight nearest and four next nearest oxygen neighbours. For oxides with perovskite-like structures of reduced symmetry (usually orthorhombic, tetragonal or rhombohedral) and other structure types, lower proton mobilities are generally reported [173, 186]. Thus mutual interactions of various defects (protons, oxide ions, acceptor metal cations) hydrogen bonding and also covalent and ionic interactions are significant in the long range proton mobility.

3.12 ELECTROLYTE MATERIALS INVESTIGATED AND MOTIVATION

In the quest to find suitable proton conducting materials within acceptor-doped perovskites (with most common formula: $A^{2+}B^{4+}_{1-x}M^{3+}_{x}O^{2-}_{3-\delta}$), the majority of the investigated materials in the literature focus on alkaline earth cerates and zirconates [27, 53, 61, 78, 200] . In comparison relatively few studies focus on proton conductivity in alkaline earth titanates [126, 173, 201, 202] based perovskites. This motivated the investigation of the structural and electrical properties of trivalent cation substituted $BaTiO_3$ with In^{3+} and Sc^{3+} as the acceptor dopant ions. A particular focus was on heavily doped systems, e.g, $BaTi_{1-x}M_xO_3$, with $x \geq 0.5$ in order to maximise the proton concentration. At the extreme of x = 1, the brownmillerite phase $Ba_2In_2O_5$ [203, 204] and

$Ba_2Sc_2O_5$ [136] based oxides have also been investigated as potential proton conductors. In addition, ytterbium substituted $BaZrO_3$ is also investigated in studies relating to the use of ZnO as a sintering aid, and the effect of co-doping with In, e.g. $BaZr_{0.5}In_{0.25}Yb_{0.25}O_{3-d}$, on the overall conductivity.

3.12.1 Naming conventions

In the following, some shorthand conventions will be used to write the compounds chemical formulas instead of the strictly correct $AB_{1-x}M_xO_{3-\delta}H_\gamma$. Here the cation-to-cation ratios are fixed, while the oxygen stoichiometry and the proton content vary. The stoichiometry of oxygen and proton using the Kröger-Vink notation is used for the gas-solid equilibrium and defects. In general, the dopant/matrix pair will be referred to as $M:ABO_3$. A further abbreviation is used, so that B stands for Barium, S for Scandium, Y for Ytterbium, I for Indium, Z for zirconium, T for Titanium, and Zn for Zink and so on. For example BTS50 means barium titanate doped with 50 mol % Scandium, or $BaTi_{0.5}Sc_{0.5}O_{3-\delta}$.

3.13 THESIS OBJECTIVES

As-per the overall approach discussed in Chapter 1, this thesis described research strongly connected to the development of suitable ceramic proton-conducting materials with potential usage as electrolytes and mixed protonic and electronic conducting cathode materials for the intermediate temperature fuel cell. In summary the particular problems and objectives we are focusing on in the present work are:

Proton conductivity in doped barium titanate: (a) the experimental investigation is focused on synthesizing new materials with a series of dopant species including In, and Sc, (b) The study is expanded to the dopant concentration and solubility limit and the effect on proton conductivity (c) Detailed structural characterization, especially those

with larger concentration of dopant. (d) Determine the total and proton conductivity in different gas conditions (wet and dry) including the dependency of conductivity on partial pressure of water vapour and oxygen. (e) Use of neutron total scattering and Reverse Monte Carlo (RMC) method to better understand the local B-site and proton environment of $BaTi_{0.5}In_{0.5}O_{2.75}$.

For the $BaZrO_3$ systems: (a) study the synthesis route and addition of ZnO on the proton conductivity in ytterbium substituted phases. (b) Investigate the impact of co-doping with Yb and In on the conductivity of $BaZrO_3$.

4: Experimental methods

4.1 SYNTHESIS OF SAMPLES

Perovskites can be prepared as polycrystalline ceramics, single crystals or thin films. Some solids can be prepared by a variety of routes but others, especially those that are not thermodynamically stable may be much more difficult to prepare and may require special methods [205]. Over the years, several preparation techniques have been developed for the synthesis of perovskite structured materials. Among them most common are (a) standard solid state reaction and (b) wet chemical method. Other techniques such as sol gel or gel polymerization, precursor, mechanical alloying, floating zone, flux method, reactive sintering etc. are also useful in terms of preparing single phase polycrystalline ceramic.

4.1.1 Solid state reaction technique

This method is also called ceramic method which consists of heating two or more non-volatile solids which react to form the required product. The solid-state method can be used to prepare a whole range of materials including mixed metal oxides, sulfides, nitrides, aluminosilicates, etc. With this technique the final product is achieved through the mixing of reactants in appropriate ratios, compacting and firing them at a relatively high temperature. The method is intrinsically slow but simple: the ions from two crystallites of different compositions which will interact inter-diffuse into each other. Although the reactants may be well mixed in the macro level (e.g. on the scale of 1 μm or 10^{-2} mm), however, on the atomic level they are very inhomogeneous. Therefore, it is necessary to grind and mix the powder at several occasions during the synthesis process.

Evidently, the hopping of an ion in a crystal lattice necessitates a great deal of energy to overcome the activation barriers, and the lattice defect (Schottky and Frenkel)

concentrations must be high enough for the inter-diffusion to take place at appreciable rates. For this reason, high temperatures (above 500- 2000 °C) and a very good contact between crystallites are essential. Very high temperature is also a requirement so that ions have sufficient thermal energy to, occasionally, vibrate or hop out of one site onto an adjacent vacancy or interstitial site. In this way the remaining reactants become more separated and thus difficult to reach the reaction to completion. One way of breaking up reactant/product interfaces is to frequently grind the partially reacted mixtures. Another way is to use liquid or gaseous transporting agent to give enhanced reaction rates. The so-called Tamman's rule [206] stating that at temperatures higher than about two thirds of the melting point T_m solid state materials become reactive (some authors also propose 1/2 T_m) in Kelvin: With the solid state method, intermediate milling and long calcinations (several hours to days) are repeated until a homogeneous powder is obtained. This method is suitable for the preparation of large batches of samples and relatively fast, cheap, with nearly 100% yields. The reactants are mostly elementary oxides or carbonates, which are thermodynamically miscible into each other, and desired product is the most stable phase at the calcination temperature. It also gives quite coarse particles (over hundreds of nm in diameter).

Experimental procedure

In this study the materials are prepared from $BaCO_3$ and oxides of various B-site elements with mostly of 99% or higher purity. After measuring in appropriate ratios, they are thoroughly ground in ethanol (95-99.5%) in an agate mortar before firing. Most of the reactions took place in alumina (Al_2O_3) crucibles in ambient atmosphere, wth a first calcination step around 800-1000 °C. After regrinding the samples are pressed to pellets of 10-20 mm die at 4-20 tons of pressure. The pellets are sintered mostly in two stages first around 1100-1350 °C, and the final one around 1400-1550 °C.

4.1.2 Solution synthesis

Wet chemical routes, sol-gel- or combustion-based, consist of the mixing of precursors in a solution or sol suspension, followed by a single calcination to obtain the product. Different combustion methods use chelating agents, like EDTA or citric acid, or additional oxidizers, like ammonium nitrate, to modulate the resulting grain size. A concentrated solution or colloidal solution of the reactants, called the 'sol', is prepared and then further concentrated to form the gel. The gel is heat-treated to form the product. Generally the steps follow as:

Dispersal or hydrolysis→Sol→ Heat or aging→ Gel→ Calcining →Product

A sol is a colloidal suspension of particles in a liquid (~1-100 nm diameters) and a gel is a semi-rigid solid in which the solvent is confined in a framework of material that is either colloidal or polymeric. The sol is transformed to a gel by dehydrating and/or polymerisation. The gel forms the product by heating to decompose the alkoxides or carbonates to give the oxide. Sol-gel methods use a polyol like ethylene glycol, and mild heating (80-120 °C) until a polymeric gel is obtained. The solid or gel here contains intrinsically homogeneous distribution of cations from the very beginning, thus minimizing the need for inter-diffusion of cations between the grains. The resulting powders are also usually obtained at low temperature and consists of very small grains (tens of nanometers in diameter). In addition, the reaction times are quite short compared to solid state reactions.

Experimental procedure

In the wet chemical route, appropriate amounts of $Ba(C_2H_3O_2)_2$, $Zr(C_5H_8O_2)_4$, $Yb(C_2H_3O_2)_3.4H_2O$, $Zn(C_2O_4.H_2O$ and/or $In(C_2H_3O_2)_3$ depending on the final product, were dissolved in hot acetic acid while stirring the solution. 0.1M citric acid was then added and the solution was heated slowly to 150–250 °C to evaporate the acid . After evaporating the acid, the solution formed a black solid. This black solid was ground in an agate mortar and heated to 400 °C for 2h followed by another heating at 800 °C for 8h .

After firing at 800 °C , the black powder turned into a white powder, which was finally ball milled at 500 rpm for 15 min and then pelletized using 10 or 13 mm diameter of die under a pressure of 4 or 8 tons , respectively. Finally, the pellets were sintered at 1500 °C in air for 24-48 h.

4.1.3 Sintering aid

Doped barium zirconate shows highly refractory nature, which promote formation of small grain sizes and a large total grain-boundary area as well as low density [123]. High temperature synthesis (1700 °C – 1800 °C) along with longer sintering time (e.g. 24h) and nano-sized particles are desirable in order to achieve desired density (> 93%) for fuel cell application [122, 207, 208]. Small grain sizes facilitate densification at relatively low temperature by contrast it introduces a larger number of grain-boundaries. High temperature sintering promotes grain-growth which indeed reduces the total grain-boundary area. However, this larger grain-growth may introduce large porosity or micro-cracks inside the sample. In addition grain boundary resistance should not dominate the total conductivity and hence dominate the fuel cell performance. High temperature synthesis can lead to evaporation of Ba leading to A site non-stoichiometry and reduced conductivity. Therefore, a balance between the high density and grain-growth is needed in order to overcome these problems. It is shown that, the sinterability of barium zirconate has been improved by the incorporation of metal oxide additives during the sintering process. Some of the additives, like ZnO, CuO, In_2O_3, Li_2O, NiO, and CaO showed a dramatic improvement on the sintering of BZY [123, 124, 208-216]. These additives are, it is shown to improve density at relatively low sintering temperature. However, excessive use of these sintering aid such as, ZnO has shown adverse effects on the conduction and suggest that only minimal amounts (< 4 mol%) should be used for improved sinterability.

Experimental procedure

20 mol% Yb doped $BaZrO_3$ samples were prepared using 2 mol% ZnO as a sintering aid. Firstly, the samples were prepared by sol-gel or wet chemical route. In this synthesis, appropriate amounts of the metal organics $Ba(C_2H_3O_2)_2$, $Zr(C_5H_8O_2)_4$, $Yb(C_2H_3O_2)_3.4H_2O$ and $Zn(C_2O_4.H_2O)$ were placed in a beaker together with acetic acid and citric acid as described in section 4.1.2. The sample prepared from solid state reaction (SSR) route used stoichiometric amounts of $BaCO_3$, Yb_2O_3, ZrO_2 and ZnO as the starting materials following the procedure described in section 4.1.1.

4.1.4 Vacuum drying, Protonation and Deuteration of samples

As-prepared samples can incorporate water while cooled down from high sintering temperature at ambient conditions. In order to get rid of this water, a dried sample was prepared by annealing the as-prepared sample at 900-950 °C under vacuum ($\approx 10^{-5}$-10^{-5} mbar pressure) for 10-12h. The sample in powder form is usually placed in a silica tube sealed at one end. This tube is heated in a furnace while connected to a vacuum pump as described in ref. [200]. The schematic setup is illustrated in Figure 4.1.

In order to incorporate protons in the as prepared samples, it is necessary to expose the samples in humid environment. When the exposure is done below approximately 300 °C, the protonation reaches maximum. The protonation reaction was conducted by annealing powder and pellet samples at 185-300 °C under N_2 gas flow (10-50 mL/min) saturated at 22°C-76.2 °C with H_2O vapour for several days (2-5 days).

Alternatively, the vacuum-dried sample is placed in a hydrothermal autoclave with maximum amount of heavy water (D_2O), calculated based on stoichiometry. The sealed autoclave is then heated at a temperature of 185 °C for 12-18h. Thus the dried sample is incorporated with heavy water; the so called deuterated sample is kept in a sealed bottle for further characterization.

4.1.5 Preparation of Pellet

Synthesized powders were mixed with a binder of approximately 1-3% by mass of the powder oxide. The binder used was either polyvinyl alcohol (PVA) or a solution (consisting of 200 mL of water, 2 g of polyvinyl alcohol (PVA), 1 ml of glycerine, and 10 mL of ethanol). Green pellets were obtained by uniaxial pressing under a pressure of 70- 230 MPa (depending on the diameter of the die used) for approximately 2-5 min. On firing, the binder was removed by heating the pellets at 600 °C (ramp of 1 °C / min) under ambient air for a period of 60 min. After sintering, the pellets were polished with SiC, and painted with Pt paste. A final firing at 800-1000 °C for 1-2 hour was performed to burn off the organics from the paste and then the Pt form porous electrodes. The fabricated pellets were further used for conductivity measurements in different atmospheres. The density of the pellets were determined by measuring the nominal mass and volume of the final sintered pellet and compared with density from X-ray diffraction.

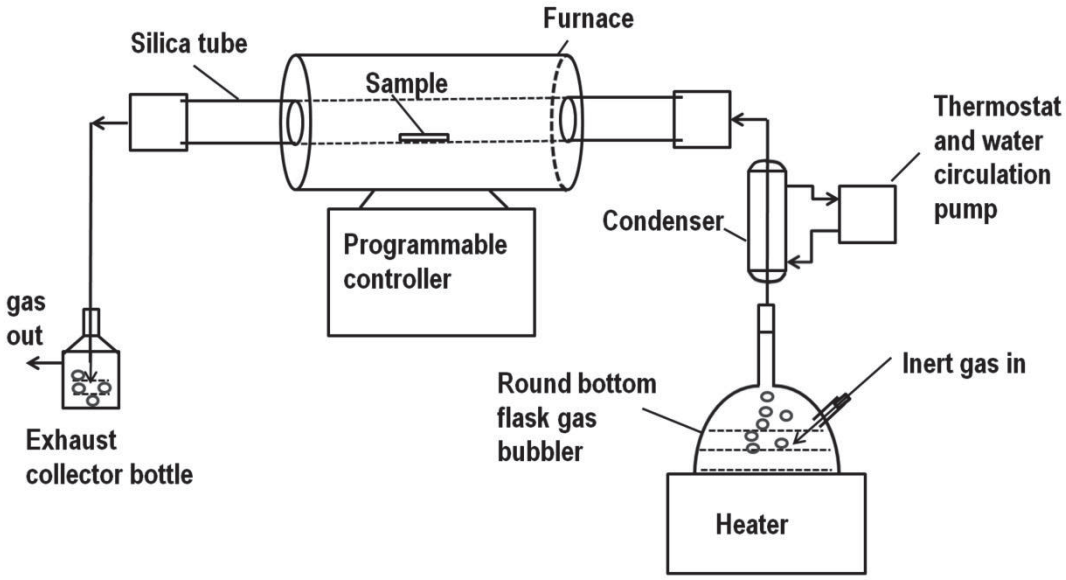

Figure 4.1 Schematic setup used for the protonation of the samples.

The Scherrer equation [217] given below was used to calculate the crystallite size of the pellets.

$$D_{hkl} = \frac{K\lambda}{B_{hkl}\cos\theta} \quad (4.1)$$

where D_{hkl} is the crystallite size in the direction perpendicular to the lattice planes, hkl are the Miller indices of the planes being analysed, K is a numerical factor frequently referred to as the crystallite-shape factor, λ is the wavelength of the X-rays, B_{hkl} is the width (full-width at half-maximum) of the X-ray diffraction peak in radians and θ is the Bragg angle. In the absence of detailed shape information, K = 0.9 is a good approximation. The instrumental broadening B_0 can be introduced in the B value by using the equation [218]

$$B = \sqrt{(B_{hkl}^2 - B_0^2)}. \quad (4.2)$$

The instrumental broadened profile was obtained from the measurement of a NIST LaB_6 line position and line shape standard (SRM 660b) for powder diffraction. The grain size of sintered samples was checked by SEM as well.

4.2 CHARACTERISATION METHODS

4.2.1 X-Ray & Neutron Powder Diffraction

4.2.1.1 X-ray powder diffraction (XRPD)

One of the methods of obtaining information about the arrangement of atoms in a material is diffraction. X-rays, neutrons or electrons are scattered by atoms that are organized in a periodic arrangement in the crystals. If the scattering centres are separated by distances comparable to the wavelength of the X-rays then interference between the X- rays scattered from particular electron centres can occur. For an ordered array of scattering centres this can give rise to interference maxima and minima [219].

Scattering of the impinging X-ray beam from neighbouring planes will produce in phase diffracted X-ray beams (constructive interference) if the additional distance

travelled by the X- ray photon scattered from neighbouring planes correspond to an integral number of wavelengths (see Figure 4.2). This path difference will depend on the lattice spacing or d_{hkl}, where hkl are the Miller indices for the planes under consideration, and will also be related to the angle of incidence of the X- ray beam, θ. For an integral wave length, the Bragg equation can be written as

$$Path\ length\ difference = 2d_{hkl} \sin\theta = n\lambda \quad (4.3)$$

$$\text{or, } \lambda = \frac{2d_{hkl}}{n} \sin\theta \quad (4.4)$$

where n is an integer and in general is always taken as unity and λ is the X-ray wave length.

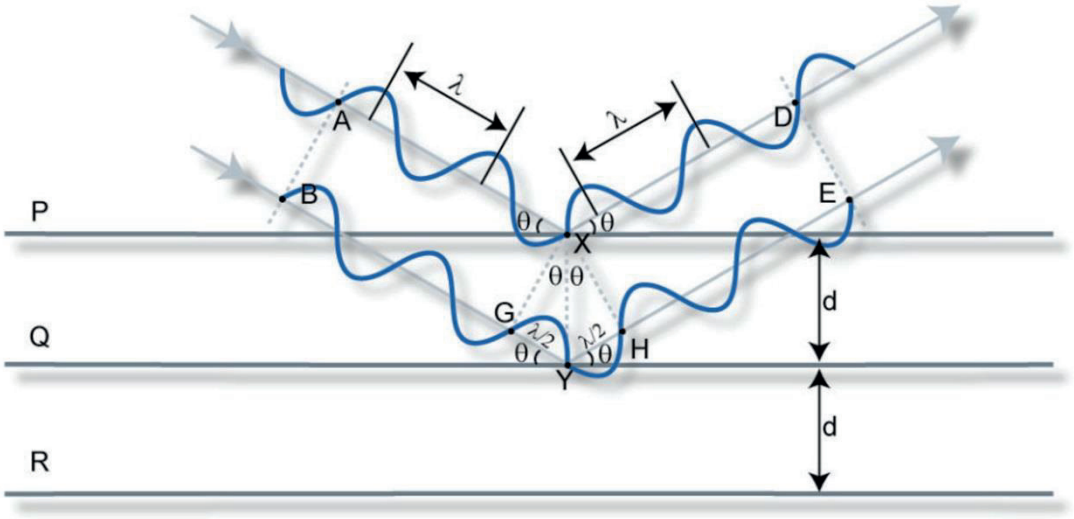

Figure 4.2: Derivation of Bragg's law. The extra distance travelled by the lower X-ray can be shown to be equal to $2d\ sin\theta$. Taken from [220].

In a crystalline material an infinite number of lattice planes with different Miller indices exist and each set of planes will have a particular separation, d_{hkl}.

To find a relation between diffraction angle, θ, Miller indices and lattice parameters one can combine Bragg's law with the appropriate plane spacing equation, which is given for a cubic system in equation 4.5

$$\frac{1}{d^2} = \frac{h^2+k^2+l^2}{a^2} \quad (4.5)$$

From this we obtain the equation

$$\sin^2\theta = \frac{\lambda^2}{4a^2}\{h^2 + k^2 + l^2\} \quad (4.6)$$

Thus from a powder diffraction experiment one can index all the Bragg reflections and eventually determine unit cell dimensions.

The peak intensities of the various reflections in an X-ray or neutron diffraction experiment are controlled by the atom types and their distribution in the unit cell [219]. Measurement of these peak intensities helps to determine crystal structure. For this purpose usually single crystal X-ray diffraction data is used as all diffraction peaks can be resolved. In a powder diffraction experiment, all the reflections occur along a 2θ axis and they tend to overlap, especially at higher angles and for low symmetry and large unit cell structures. Hence it becomes difficult to extract intensities for individual reflections. Structural information may still be obtained from powder diffraction patterns using the Rietveld method, as will be discussed later.

4.2.1.2 Neutron powder diffraction (NPD) [221-223]

In comparison with X-rays, neutrons have a much higher relative sensitivity towards light elements in comparison with heavy elements. Neutrons can also often distinguish neighbouring elements, multiple site occupancies and defect for example oxygen vacancies (both randomly distributed or ordered) in complex oxides. In addition, as neutrons interact with unpaired electrons, magnetic structures can be studied. The disadvantages of NPD include the scarcity and low flux of its sources and the large quantity of sample needed for obtaining good-quality data.

In a continuous wavelength, reactor source, neutrons are produced through the fission process in a nuclear reactor. Here a single (selectable) wavelength can be used with a continuous flux of neutrons. Position sensitive detectors, are used to record neutron rate as a function of diffraction angle.

In a pulsed or spallation source, neutrons are generated by colliding pulses of accelerated charged particles such as protons into a heavy element target. The neutrons produced in both systems have a high velocity, and are slowed down by a moderator to be useful for ND experiments. The type and temperature of the moderator affects the obtained distribution of energy (wavelength) for the neutrons, with a peak indicating the energy (wavelength) of the majority of neutrons. The neutrons produced at spallation sources always have a low wavelength (high energy) tail before the peak distribution. In general they have higher flux in the low wavelength region compared to the reactor source neutrons (Figure 4.3).

This is particularly helpful for the study of the small d-spacing region, using spallation sources. Due to the fact that the flux of neutrons generated in these sources is pulsed, they can be used for time of flight experiments that will be discussed later. For steady state sources, a certain wavelength of neutrons for the diffraction experiment can be carefully chosen by a monochromator. Keeping in mind that neutrons have no charge and have a high mass, they penetrate into the atoms without being diffracted by electrons. The scattering take place through interaction of neutrons with the nucleus.

The probability of interaction between neutrons and the nucleus is determined by the intensity of the neutron beam and a parameter called the cross section. In practice, it can be defined as the effective area presented to the neutron beam by a particular nucleus, and has units of area, barn, where 1barn = 10^{-24}cm^2. This parameter is not directly related to the area or size of the nucleus. The interaction between neutron and the nucleus can be in the form of absorption or scattering, and therefore the cross section consists of two components: the scattering cross section and the absorption cross section, and expressed

as function of b, here b is a parameter called the scattering length, which is analogous to the x-ray scattering factor, but has different properties due to the difference between scattering processes of neutrons and x-rays.

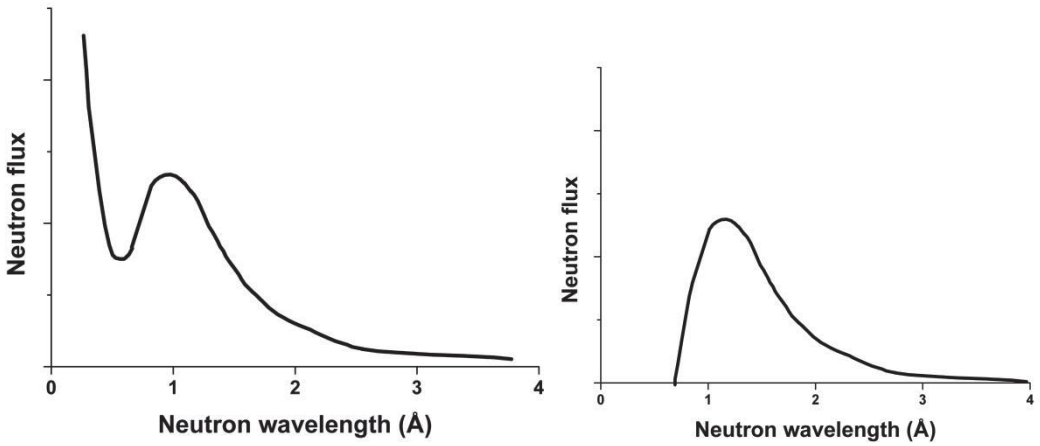

Figure 4.3. The distribution of Neutron wavelengths in a spallation source (left) and a reactor source (right).

The scattering of neutrons can be regarded as instantaneous capture and re-emission of the neutron by the nucleus. Therefore, the neutron scattering power is different from the x-ray scattering power in that b is related to the nuclear forces and there is no theory to predict its value. It has to be determined experimentally for different nuclei. Also, unlike the x-ray scattering factor, there is no angle dependence for *b*, and therefore in a neutron diffraction pattern, the intensities of structural peaks do not vanish at large 2θ angle. Also, *b* depends on the type of nucleus, and therefore, different isotopes of the same element will have different *b* values. Another interesting property of *b*, is that it can be negative for some nuclei, which implies a 180° phase change upon scattering. In some cases, such as ^{51}V, $b \approx 0$. This means almost no interaction with the neutron beam, which is why the sample containers for neutron diffraction experiments often are made of ^{51}V.

4.2.1.3 Time of Flight (TOF) Neutron Diffraction

This is also called energy-dispersive or fixed angle procedure. In this technique a pulsed neutron beam with a range of wavelengths is delivered to the sample. The time of flight method takes advantage of the inverse relationship between the wavelength and velocity of the neutron. Therefore, the shorter the wavelength, the shorter the time needed to reach the detector.

The de Broglie relation is given by:

$$\lambda = \frac{h}{mv} = \frac{ht}{mL} \tag{4.7}$$

where λ is the wavelength, m is the mass of neutron, v is the velocity of the neutron, h is Plank's constant, t is the time of flight and L is the distance travelled by the neutron. Combining this with Bragg's law gives:

$$\lambda = 2d \sin\theta = \frac{ht}{mL} \rightarrow d = \frac{ht}{2mL \sin\theta} \tag{4.8}$$

TOF, t (μsec) = 252.78L(m)λ(Å), where the symbols in bracket indicates units.

By recording the time it takes for a neutron to reach the detector, one can calculate its wavelength, or the d-spacing of the set of planes by which it is diffracted. Here each detector collects a complete diffraction pattern upon manifestation of each neutron pulse. This is because different wavelength neutrons conforming to different d-spacings reach the detector at different times. The resolution of the data is related to the uncertainty in the d- spacing. In general, highest resolution is achieved in TOF diffraction by using long incident flight paths and scattering angles close to 180° (i.e. back scattering) [222]. A detector at a lower angle (lower bank) records large d-spacing, while a high-angle (backscattering) detector collects small d- spacing. There will be some overlap between the d-regions covered by these detectors. Schematic representation of the time of flight instrument and various detectors set up is presented in Figure 4.4.

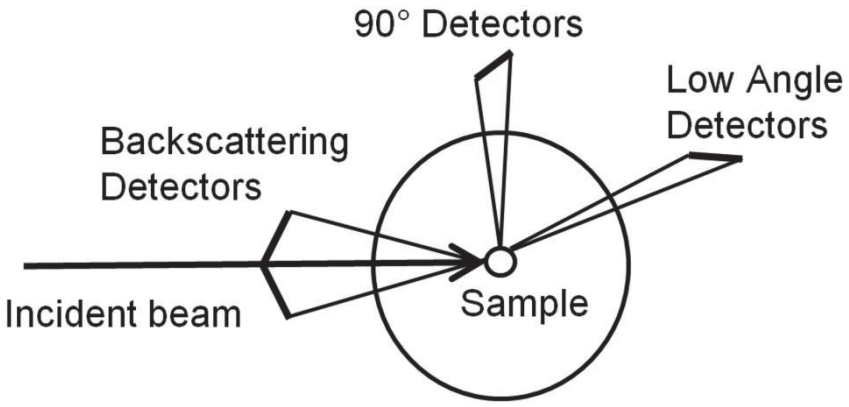

Figure 4.4 Schematic representation of the time of flight instrument set up.

4.2.1.4 The Rietveld method [224-227]

Rietveld refinement (full profile fitting) is a least-squares refinement technique used to minimise the difference between observed powder diffraction data, y_i(obs), and a calculated powder diffraction profile, y_i(calc), where i is any arbitrary point in the pattern. It is a comprehensive, computer based method for the analysis of the entire powder diffraction pattern, the Bragg peak intensities do not need to be treated individually.

Hugo Rietveld, the founder of the method, realised that for non-Gaussian and non-symmetric peak shape, the profile function or angular dependency could be represented by

$$H_k{}^2 = U\tan^2\theta_k + V\tan\theta_k + W \qquad (4.9)$$

Where H_k is the full-width-at half maximum (FWHM) and U, V and W are the half width parameters that may be refined during the least-squares fit. H, is insight about peak shapes and angular dependency made the full profile fitting method possible.

Today the angular dependency or reflection profile function (denoted S_{ik} in equation 4.10) are often described by pseudo-Voigt, Pearson VII, Gaussian, Lorentzian and modified Lorentzian functions.

A trial structural model is needed in order to calculate the structure factor, F_{hkl}, one of the terms in y_i(calc) (See equation 4.10). Many Bragg reflections usually contribute to the intensity, y_i, observed at any arbitrary point, i, in the pattern. The calculated intensity in each point is determined from $|F_k|^2$ values calculated from the structural model plus a number of other terms.

$$y_{icalc} = \alpha \sum_k L_k |F_k|^2 S_{ik}(2\theta_i - 2\theta_k) P_k A + b_i \qquad (4.10)$$

where α is the scale factor, L_k contains the Lorentz, polarization and multiplicity factors, $|F_k|^2$ is structure factor, S_{ik} is reflection profile function, P_k is the preferred orientation, A is the absorption factor and b_i is the background intensity at the i^{th} point.

The principle of the Rietveld Method is to minimise a function M which represents the difference between a calculated profile y(calc) and the observed data y(obs). Least square refinement is undertaken until the best fit between the experimental and calculated data is obtained according to the equation below defined by Rietveld:

$$M = \sum_i W_i \left\{ y_i^{obs} - \frac{1}{c} y_i^{calc} \right\}^2 \qquad (4.11)$$

where W_i is the statistical weight and c is an overall scale factor such that $y^{calc} = cy^{obs}$. The accuracy of the structural model fitted to the observed data is judged by several reliability factors adapted to the Rietveld method. For further details consult reference [224-227]

4.2.1.5 Neutron total scattering and Reverse Monte Carlo (RMC) technique

Theoretically, a crystalline system is governed by periodicity up to an infinite range. The analysis of the Bragg diffraction gives an average description of the structure

of the crystalline material in terms of the atomic positions and their thermal vibrations. However, in reality most crystals have defects and local deviations of atoms different from the average structure. Displacements of atoms away from their ideal positions may appear as a `smeared' average atomic distribution [228]. In powder diffraction it is sometimes possible to observe the effects of these local atomic arrangements in the form of diffuse peaks observed as broad undulations in the `background' scattering. However, traditional data analyses and fitting methods deal with sharp Bragg peaks and diffuse features are often ignored or folded into the background. The distribution of defects in some materials is random, while in some compounds there is local ordering of defects. However, due to the absence of long-range defect periodicity, the powder diffraction pattern shows similar Bragg peaks for both types of compounds. A complete structural description of a crystalline material containing a significant concentration of defects requires the characterisation of both long-range and short-range correlations which, in turn, necessitates the analysis of both the Bragg and the diffuse scattering components (together termed the `total scattering'). A number of approaches have been developed to address this issue, including the *PDFFIT* [229] and reverse Monte Carlo (RMC) methods [230].

4.2.1.6 Experimental setup and procedure

The X-ray powder diffraction (XRPD) measurements were carried out at ambient temperature using a Bruker AXS D8 ADVANCE VARIO powder diffractometer [231].

The diffractometer was operated with Cu$K_{\alpha 1}$ (wavelength, λ=1.5406 Å) radiation generated at 40 kV and 40 mA, with a solid-state LynxEye detector. Bragg-Brentano Para focusing geometry results in both high resolution and high intensity of the diffracted beam. The Bragg-Brentano geometry consists of two circles, the measuring circle and the focusing circle [220].

Initial 30 minute scans were performed in order to check the phase purity and progress of synthesis in the 2θ range 20 – 65 ° with a step size of 0.05 ° and 2s collection

time per step. Longer, high quality, scans were used for further structural analysis of the as-prepared sample in the 2θ range 10 – 120 °, with a step size of 0.0092 ° and 3.9s collection time per step. The resulting pattern was ported in the evaluation software package DIFFRACplusEVA with SEARCH, where phases were identified, after background subtraction with the aid of the ICDD database. The data was analysed by the Rietveld method [224] using the GSAS program with EXPGUI interface [232, 233]. The software Winplotr in fullprof [234] , TREOR [235] and Celref [236] are used to plot, indexing and initial cell parameter evaluation form the diffraction data.

Neutron total scattering data was collected on the Polaris diffractometer of the ISIS facility, Rutherford Appleton Laboratory, U.K. [237], using the backscattering detector bank (covering scattering angles of 130 <2θ<160°), the ~90° detector bank (85 <2 θ<95°), and the low angle detector bank (28 °<2θ <42°). These cover approximate ranges of scattering vector Q (where Q= 2π/d and d is the inter-planar spacing) of 2-30Å^{-1} 1.5-20Å^{-1}and 0.8-12Å^{-1}, respectively. The sample was encapsulated in a standard 8 mm vanadium can and kept in a cryostat at a temperature of roughly 4 K for the duration of the experiment. The measurement took approximately 12 hours in order to obtain counting statistics of sufficient statistical quality to allow analysis of the total scattering.

After correction for the effects of background scattering and beam attenuation, the diffraction data from each detector bank was merged to form a single spectrum covering a wide Q range using the program Gudrun [238]. This process brings the scattered intensity onto an absolute scale of scattering cross-section. The resultant normalized total scattering structure factor, S(Q), was used to generate the corresponding total radial distribution function, G(r), via a Fourier transform [230].

RMC modelling of the neutron total scattering data was performed using the RMCProfile software [239]. The RMC model usually have a configuration box containing 12×12×12 unit cells. The RMC modelling used both reciprocal space data, $S(Q)$, and real space data, $G(r)$. The former emphasizes the long-range ordering whilst the

$G(r)$ focuses on the short-range interactions. Finally, a total of 10 RMC runs were performed to improve the statistical significance of extracted results.

4.2.2 Thermogravimetric Analysis (TGA)

Thermogravimetric analysis measures the change in mass of a substance as a function of temperature or time. The mass difference is a fundamental property of the sample and useful for quantitative calculations of compositional changes. Proton conducting oxides when treated in humid atmosphere, gain mass due to incorporation of protons. From the mass change the concentration of protonic defects can be measured, while differential scanning calorimetry (DSC) can be used to determine possible phase changes, as well as the order-disorder temperature. The Apparatus used for this study is the NETZSCH model STA 409 PC Luxx® simultaneous thermal analyser. A schematic setup is shown in Figure 4.5. The system employed for this work was equipped with a SiC furnace capable of operation from 25 to 1550 °C and a TG-DSC sensor. The system is vacuum tight and measurements performed in inert (dry N_2) atmospheres. Firstly the mass of the empty alumina crucible is determined before the finely ground sample is loaded and weighed. A protective N_2 flow of 20 mL/min is maintained during the experiment. The sample is heated at a rate of 20 °C /min, from room temperature to 1000 °C. Data is also collected in cooling mode as well with a isothermal step in between and using 20 °C /min cooling rate. The data is automatically corrected by subtracting a previous run performed with identical heating conditions and an empty sample crucible to allow the behaviour of the sample to be determined.

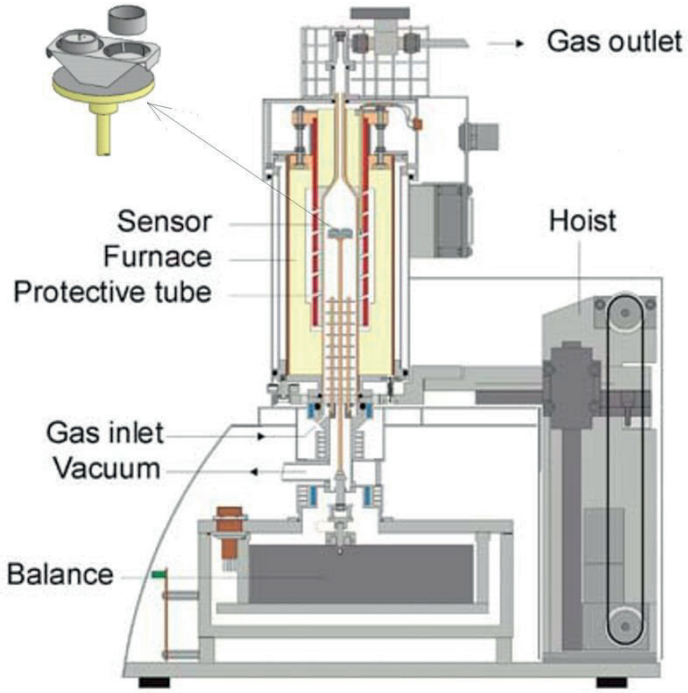

Figure 4.5, Schematic setup for the TGA

4.2.3 Impedance Spectroscopy [240-248]

Solid electrolytes properties and application can be governed by the close control of structure or microstructure (porosity, grain size and orientation, nature of grain boundaries), composition, ceramic texture, dopant and dopant (or defect) distribution. Impedance spectroscopy is a powerful technique for unravelling the complexities of such materials, by utilizing the different frequency dependencies of the constituent components for their separation. Thus, electrical inhomogeneity in ceramic electrolytes, electrode/electrolyte interfaces, surface layers on glasses, ferroelectricity, positive temperature coefficient of resistance behaviour and even ferrimagnetism can all be probed, successfully using this technique.

Electrical impedance, or simply impedance, is a measure of opposition to a sinusoidal alternating electric current. The concept of electrical impedance generalises

Ohm's law to AC circuit analysis. Unlike electrical resistance the impedance of an electric circuit can be a complex number, but the same unit, (ohm), is used for both quantities. Here the resistive and capacitive elements arising from the bulk and grain boundaries in the polycrystalline material can be separated into separate contributions. In this subsection, the underlying background of the technique will be introduced along with a useful model needed to interpret and analyse obtained results.

Generally an electrical stimulus such as a known voltage or current is applied to the electrode and a response current or voltage is observed [244]. It is most common to apply a single –frequency voltage to the interface and measure the impedance directly from the resulting phase shift and amplitude or the real and imaginary parts of the current at that frequency. Also a small direct current across a pellet of the sample, together with a superimposed alternating current can be used. For example, a sinusoidal voltage signal $v(t) = V_m \sin(\omega t)$, is applied to a circuit. This will result in a sinusoidal current, I, with the same characteristic frequency but due to capacitive or inductive circuit elements, the current may be phase-shifted by an angle θ relative to the voltage: $i(t) = I_m \sin(\omega t + \theta)$. Here $v(t)$ is the voltage function, $i(t)$ is the current function, V_m is the amplitude of voltage, I_m is the amplitude of current, ω is the angular frequency of rotation, t is time and θ is the phase difference between voltage and current [244].

According to Ohm's law, the resistance is the ratio between voltage and current. For alternating currents, the term impedance is used to describe this ratio as well as the phase shift between them. The impedance, Z consists of two components; in phase and $\pi/2$ out of phase with respect to the voltage. The in- phase part consists of the ratio between the voltage and the in-phase current, giving the real impedance component. It is termed resistance, R, and reflects the impeded transport of charge carriers through the impedance element. The out-of-phase part is similarly the imaginary impedance component and is termed reactance, X. Therefore, the total impedance may also be represented as a two-dimensional vector with a real part along the x-axis and an imaginary part along the y-axis as shown in Figure 4.6 below.

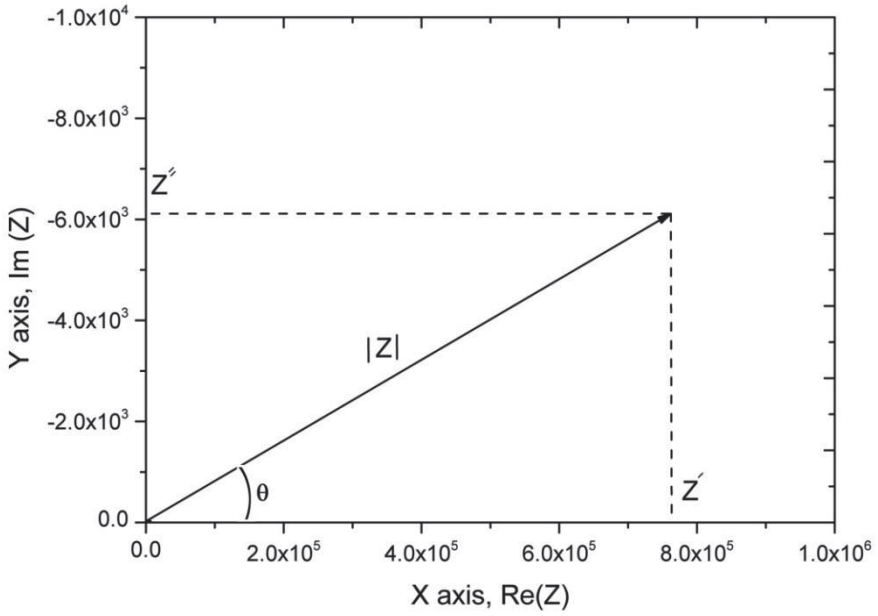

Figure4.6 The vector representation of impedance, Z, in rectangular coordinates adapted from [244].

Z= Real(Z)+j Im(Z)= R+jX and in addition, *Z(ω) = v(t)/ i(t)* and its magnitude is $|Z(\omega)| = \frac{V_m}{I_m}(\omega)$and phase angle is *θ(ω)*. It should be noted that although *Z* is the ratio of two phasors, *Z* is not itself a phasor. That is, *Z* is not associated with some sinusoidal function of time. For DC circuits, the resistance is defined by Ohm's law to be the ratio of the DC voltage across the resistor to the DC current through the resistor:$R = \frac{V_R}{I_R}$, where V_R and I_R are DC (constant real) values. Impedance in rectangular form is simply the sum of the real part with the product of j and the imaginary part: can be written as $Z(\omega) = Z' + jZ''$ where *j* is imaginary unit$\left(\sqrt{-1}\right)$. Form the Figure 4.6 *Real (Z)* = $Z' = |Z|\cos(\theta)$ and Imaginary, *(Z)* = $Z'' = |Z|\sin(\theta)$ with the phase angle, $\theta = \tan^{-1}\left(\frac{Z'}{Z''}\right)$ and modulus, $|Z| = \sqrt{Z'^2 + Z''^2}$.

The inverse of the impedance is admittance, Y, and is similarly a complex number obtained by the ratio between current and voltage. The real and imaginary components of the admittance are termed conductance (G) and susceptance (B), respectively:

$Y= Real(Y)+j\ Im(Y)= G+jB$

4.2.3.1 Passive Electrical Circuit Elements

When a current flows through a polycrystalline material it will be affected by the samples microstructure. The bulk interior, the grain boundaries, and the surface between the electrode and the sample will give a real hindrance of the transport of the charge carriers (resistive effect) and accumulation of the charge carriers (capacitance effect) travelling through the sample. The polycrystalline material response to the alternating current can be represented by three types of passive electrical circuit elements.

Resistor

One of the passive electrical circuit elements is the resistor. It is an element with a long-range transport of charge carriers where the charge carriers give rise to conductance, G and resistance $R = 1/G$. Ideally, a voltage across a resistor will instantly give rise to current and they are therefore considered to be in phase with one another ($\theta = 0$). Consequently, the impedance will only consist of a real part (resistance) that can be given as:

$$Z_{Reisistor} = \frac{V}{I} = \frac{V_m \sin \omega t}{I_m \sin \omega t} = \frac{V_m}{I_m} \quad (4.12)$$

The SI unit (International System of Units) of resistance is ohm (Ω).

Capacitor

The ideal capacitor consists of two parallel plates separated by vacuum or a dielectric material. The simplest form of a capacitor consists of two parallel conducting plates, each with area A, separated by a distance, L, with the insulator in-between. If a voltage is applied over the capacitor a charge is built up. How much charge the capacitor

can build up depends on its capacitance, *C* (in unit of farad, F), which is the ratio between stored charged, *Q* (in unit of coulomb, C), and the voltage *V*,

$$C = \frac{Q}{V} = \in_0 \in_r \frac{A}{L} \tag{4.13}$$

Where $\in_0$ is the permittivity in vacuum, $\in_r$ is the dielectric constant (or relative permittivity) of the medium. As an alternating voltage is applied over the capacitor, a phase-shifted current will be produced with $\theta = \pi/2$. The impedance of a capacitor will therefore consist of one frequency-dependent imaginary part:

$$Z_{capacitor} = \frac{1}{j\omega C} \tag{4.14}$$

Inductor

In contrast to the capacitor, which is an ideal insulator, the inductor is an ideal conductor. It typically consists of a conducting wire shaped as a coil with no resistance. As a sinusoidal voltage is applied over the inductor, a phase-shifted current with $\theta = -\pi/2$ will be produced. The impedance of an inductor will therefore similarly consist of one frequency-dependent imaginary part:

$$Z_{Inductor} = j\omega L \tag{4.15}$$

where L is the inductance of the inductor with units given in henry, H.

4.2.3.2 Physical models for Equivalent Circuit Elements

The complex impedance can be represented in a Nyquist plot (Complex plane plot) with the impedance vector Z shown as a function of the imaginary versus the real impedance, as illustrated in Figure 4.7. Here the resistor and the capacitor are connected in parallel (RC) give rise to a semicircle of radius R/2 in the first quadrant.

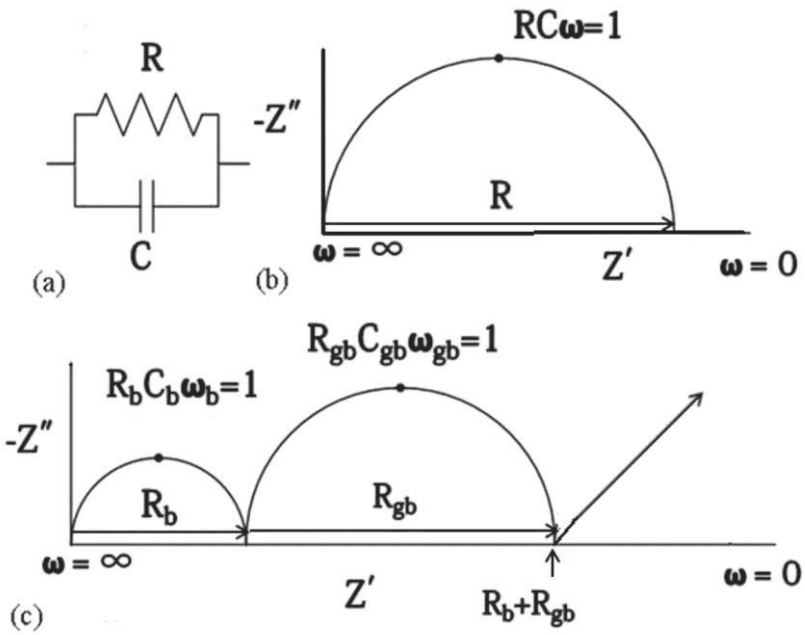

Figure 4.7 Complex impedance of a polycrystalline material: (a) equivalent circuit of a component, (b) impedance spectrum of the equivalent circuit in (a), (c) impedance spectrum of a typical ceramic sample with each semicircle representing one component with an equivalent circuit as in (a), where the highest frequency corresponds to the response to the bulk, middle frequencies to the grain boundary response, and lowest frequencies to the electrodes.

As polycrystalline material is comprised of grain interior or bulk (b) and Grain boundaries (gb), they may exhibit different conductivities. Sometimes, grain boundaries probably have boundary cores that are highly conducting and space charge layers that are depleted of charge carriers, or vice versa. Highly conducting grain boundaries in polycrystalline materials cannot be distinguished by impedance spectroscopy; they come out as an extra lumped (RC) circuit element in parallel with that of bulk and in this way merges into the bulk element [246]. However, highly resistive grain boundaries form an

extra lumped (RC) element in series with bulk element gives rise to a new semicircle in the impedance diagram, occurring at lower frequencies as represented in Figure 4.7.

An important aspect of these semicircles is that the frequency at the apex corresponds to the characteristic frequency, ω_0 of each of the subcircuits (RC) is given by [249]

$$\omega_0 = \frac{1}{RC} = \frac{A}{\rho L}\frac{L}{\epsilon_0 \epsilon_r A} = \frac{\sigma}{\epsilon_0 \epsilon_r} \tag{4.16}$$

Where resistivity, ρ is equal to $1/\sigma$, A is the area of the cross-section; L is the length of the sample.

In practice, the impedance spectrum of a polycrystalline material may be more complicated than the simple combination of RC elements and semicircles usually appear are depressed. The impedance of such a non-ideal behaviour is often represented by a Constant Phase Element (CPE). The CPE behaviour is generally attributed to a distribution of a physical property of the system, such as distributed surface reactivity, surface inhomogeneity, roughness, porosity, current and potential distributions associated with electrode geometry, etc., depending on the system. A constant phase element (CPE) is assigned with the symbol Q and in an admittance given by:

$$Y = Y_0(j\omega)^n \tag{4.17}$$

Y_0 describes a pseudo-capacitance and n is a real constant between -1 and 1. For instance, a capacitor, resistor and inductor, n equals 1, 0 and -1 respectively. A system of many grain boundaries is often well represented by a (RQ) subcircuit with n = 0.75 i.e. they are capacitor-like [246]. This new capacitance, when substituted in the expression for the characteristic frequency, ω_0, gives:

$$\omega_0 = \frac{1}{(RY_0)^{1/n}}. \tag{4.18}$$

The real capacitance of the (RQ) sub circuit can be calculated as:

$$\mathrm{C} = \frac{1}{R\omega_0} = Y_0{}^{(\frac{1}{n})} R^{(\frac{1}{n}-1)}. \tag{4.19}$$

The experimental impedance data *Ze(ω)* may be well approximated by the impedance of *Zeq(ω)* of an equivalent circuit made up of ideal resistors, capacitors, and perhaps inductances and possibly various distributed circuit elements [244]. The figure is for an arbitrary sample showing complex plane plot (-Z′′vs. Z' where Z'' is the imaginary part and Z' is the real part of the impedance) and equivalent circuit typically used to evaluate the impedance contribution from the bulk, the grain boundaries and the electrodes.

4.2.3.3 Grain Boundaries and Brick Layer Model

The measurement of the bulk conductivity is straightforward from the Nyquistplot, while the measurement of specific grain boundary conductivity requires knowledge of the grain size and grain boundary thickness. Two of the most prominent models that often are suggested are the parallel model and the series model, where the latter is more well-known as the brick layer model. In the brick layer model, a polycrystalline material is assumed to consist of uniform cube-shaped grains separated by grain boundaries both in parallel and perpendicular to the direction of the applied field.

The conducting species can either flow along the parallel grain boundaries or through the grains but they are in both cases geometrically required to cross the series grain boundaries. In order to determine the grain boundary conductivity without detailed micro-structural and electrical information, a "brick layer model" is adopted, as shown in Figure 4.8, where L is the sample length, A is the sample crosses sectional area, G is the edge length of the grains and g is the grain boundary thickness. The implication of the "brick layer model" and its application was discussed in detail in ref [249].

Here we list the conclusions that will be used in this study. Let σ_{bulk} and σ_{gb} be the specific conductivity of the bulk and grain boundary, respectively. For the situation where $\sigma_{bulk} > \sigma_{gb}$ and $g << G$, the bulk conductivity is described as

$$\sigma_{bulk} = \frac{L}{AR_1} \tag{4.20}$$

While σ_{gb} can be obtained in terms of the ratio R_1 to R_2 and g/G

$$\sigma_{gb} = (\frac{g}{G})\frac{R_2}{R_1}\sigma_{bulk} \tag{4.21}$$

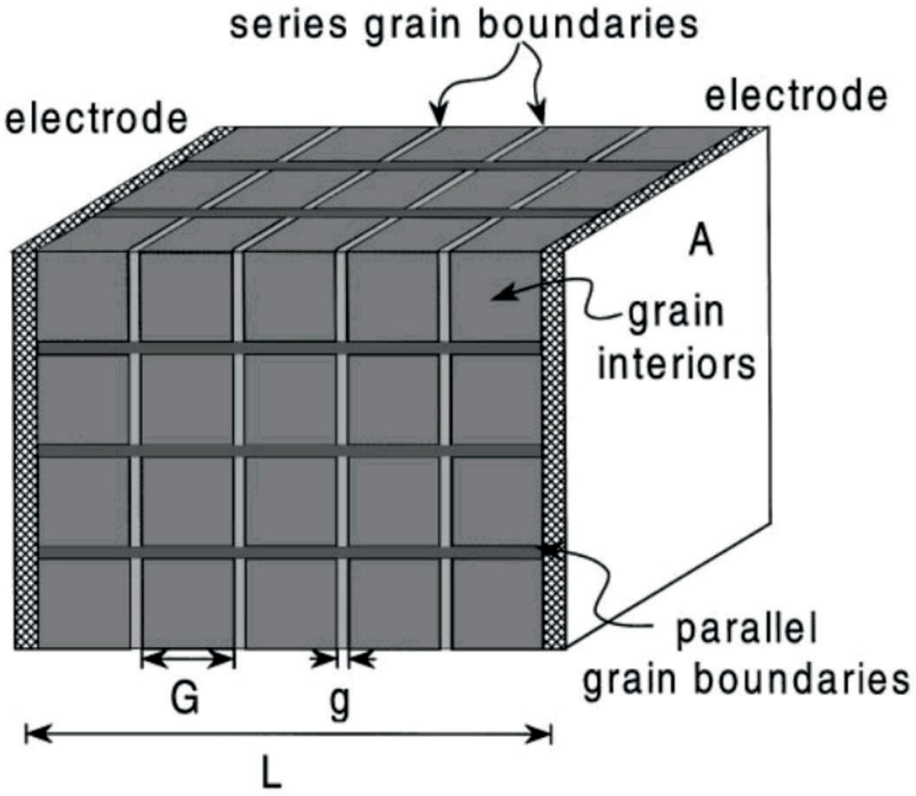

Figure 4.8 "Brick Layer" model of a polycrystalline material. Grains are assumed to be cube-shaped, and grain boundaries to exist as flat layers between grains. Taken from ref. [249] with permission.

The parameter g/G is available from the dielectric constant of the bulk and grain boundary using the equation,

$$\frac{g}{G} = \frac{C_2}{C_1}, \tag{4.22}$$

where $C = 1/R\omega_0$, as described in Figure 4.7 (a). The grain boundary conductivity derived by this means is called "specific grain boundary conductivity."

4.2.3.4 Conductivity measurement procedure

The electrical measurements were conducted using a 2-point 4-wire set-up on two different impedance spectrometers. The first of which was a HP4192A, Impedance Analyser. This instrument was only used for total conductivity measurements of BTI50 at a constant frequency of 10 kHz and an oscillation voltage of 1 V. The impedance was also measured from 4.5 MHz to 1 Hz using a Solartron 1260 frequency response analyser applying a sine wave amplitude of 1 V rms. The conductivity cell used was a ProboStat^{TM} (NorECs AS) [250].

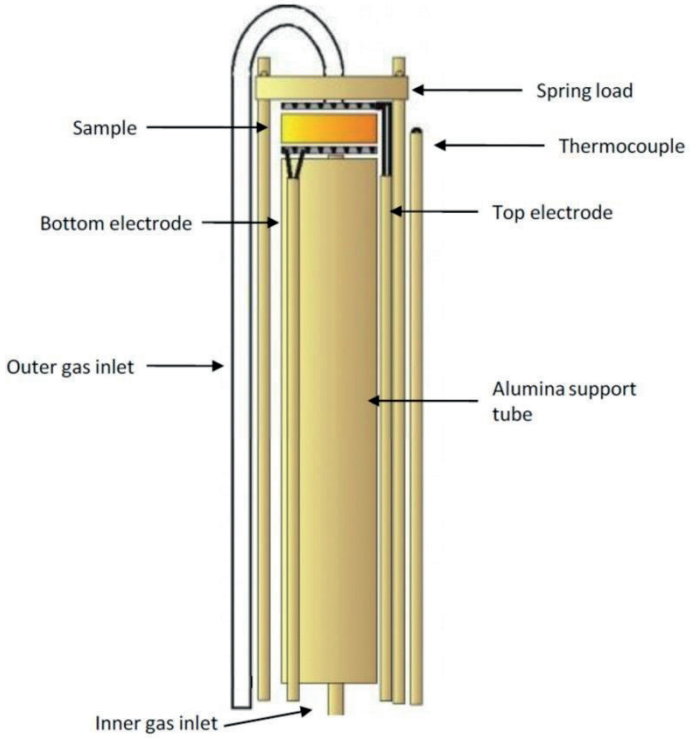

Figure 4.9 Schematic picture of the cell used for conductivity measurement taken from [250, 251]

Impedance measurements were performed on a sintered pellet of the as-prepared material, 10-20 mm in diameter, with platinum paste (Engelhard) used to assure good

ohmic contacts. The Pt electrode area and thickness of the pellet was used to extract the final conductivity. Impedance data were initially collected on heating from 150 to 1000°C (heating cycle) and cooling down from 1000 to 150°C (cooling cycle) in 50°C steps under dried, wetted and D_2O wetted conditions. Sufficient time was allowed to ensure the equilibrium before the measurement. Dry gas condition was achieved by flowing the through two beds of P_2O_5 desiccant. The wet condition was maintained by bubbling the gas through water at 22°C ($p(H_2O)$ = 0.026 atm). The conductivity cell was inserted into an external furnace.

For control of the furnace Impedance Measurement Software "SmaRT" [252] was used. The cell, as shown in Figure 4.9, consists of a long alumina support tube on which the sample is mounted.

Two electrode contacts are connected to either side of the pellet, which are then held together by a spring load. The cell contains two gas inlets providing gas below and above the sample. The cell is sealed using an outer quartz tube and a rubber O-ring.

4.2.3.5 Constant frequency AC impedance: experimental

The material was further characterized electrochemical impedance spectroscopy as a function of temperature, oxygen-, water vapour- and heavy water vapour partial pressures. Two different gas mixer and frequency response analyser was used. For this experiment, ProboStat measurement cell was connected to a gas mixer that could provide gases with well-defined activities. Point measurements of ac conductivity at fixed frequency were conducted at 10 kHz with A HP/Agilent 4192A impedance spectrometer.

The atmosphere in the measurement cell was further controlled using an in-house built gas mixer depicted in Figure 4.10. As illustrated, the gas mixer consists of eight flowmeters (A-H) arranged pairwise to form four stages of mixtures M1-M4. An excess of each mixture is bubbled over columns of descending heights of dibutyl phtalate (B1-B4), which ensures a constant overpressure through the system. The first three stages

serve to dilute O_2 (G1) with Ar (G2) giving an oxygen partial pressure range of 1 atm to 10^{-5} atm. Mixture 3 can subsequently be wetted by H_2O or D_2O via a wetting stage to form mixture 4.

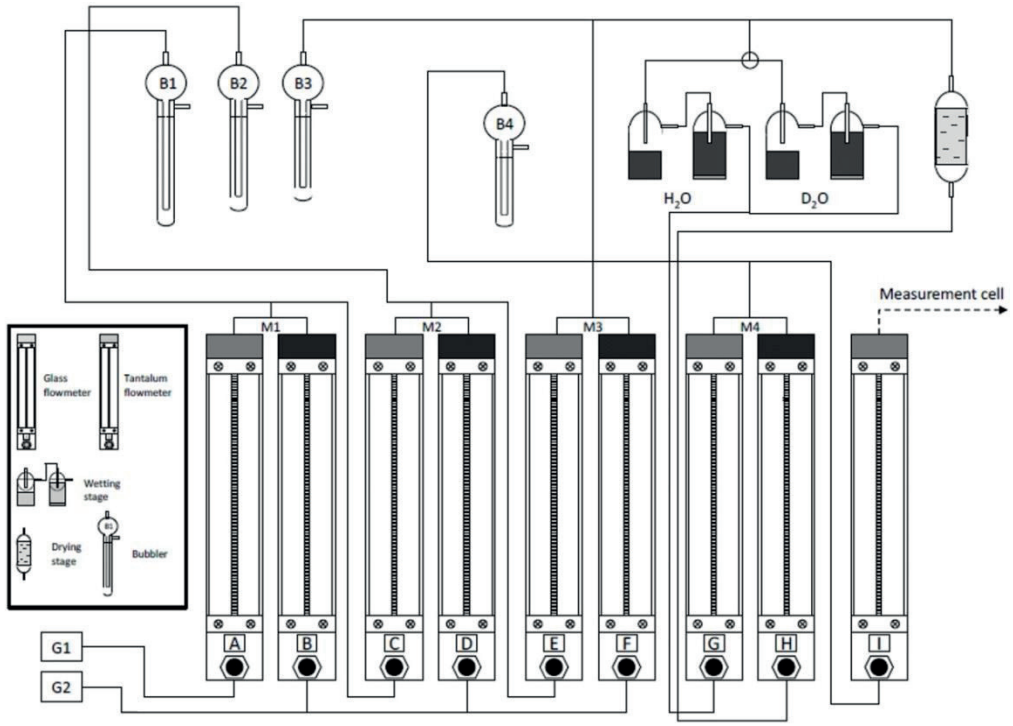

Figure 4.10 Sketch of the gas mixer used. G1 and G2 were H_2/O_2 and Ar, respectively taken from [251].

Wet conditions were achieved by bubbling oxygen gas through a saturated KBr solution giving a water vapour pressure of approximately 0.023 atm at room temperature. Drying of the gas was achieved by running the gas through a column of P_2O_5. In practice, the partial pressure of water in dry gas in the conductivity cell is estimated to be 3.0×10^{-5} atm [253]. Intermediate water vapour pressures were achieved by mixing wet and dry portions of the gas. H/D isotope effects were investigated by comparing the results obtained in H_2O and D_2O-wetted gases.

4.2.3.6 Variable frequency AC impedance: experimental

For variable frequency AC impedance spectroscopy measurement under partial pressure of O_2 for BTS70 sample, a solatron 1260 frequency response analyser was used. Conductivity isotherms (at temperatures from 1000 to 400°C) were measured versus the partial pressure of oxygen in the range 2.5×10^{-4} to 2.5×10^{-1} atm under dry conditions (~30 ppm H_2O). The impedance was monitored versus time at each new set of conditions to ensure that equilibrium was achieved before taking a measurement. Partial pressure of oxygen was measured, using a zirconia ceramic electrolyte and atmospheric air, with $p(O_2)= 0.209$, as a reference. O_2 gas was diluted by mixing with Ar. Both the gases were measured and controlled via a flow meter before mixing. Dryness was ensured by flowing the gas through a bed of P_2O_5.

4.2.3.7 Specific conductivities

The specific conductivities of the samples can be corrected for porosity using the empirical equation:

$$\boldsymbol{\sigma_s = \frac{\sigma_m}{(1-v_p)^n}} \tag{4.23}$$

Where $n = 2$ (1st approximation)[254] or 3/2 [212], σ_s and σ_m are the specific and measured conductivities, respectively, while v_p is the volume fraction of pores in the samples. Relatively large uncertainties of about 20 % are involved while using n=2, to estimate σ_s [255]. However, only small improvements may be made using more detailed knowledge regarding the sample's microstructure.

4.2.4 Scanning Electron Microscope (SEM) and Energy Dispersive Spectroscopy (EDS)

Scanning electron microscopy (SEM) in conjunction with Energy dispersive spectroscopy (EDS) was used to examine microstructural and chemical features of sintered samples. The microstructure and chemical composition of sintered samples were

investigated by means of scanning electron microscopy (Leo Ultra 55 FEG SEM) in conjunction with energy dispersive X-ray spectroscopy (EDS, Oxford INCA). The exposed top surface of the sample was polished in preparation for chemical analysis. The accelerating voltage was 2-20 kV. The collision between the bombarding electrons with the atoms of the specimen can be either elastic (electron-nucleus) or in-elastic (electron-electron) [256]. The first type of collision generates backscattered electrons, which contains information regarding topography and composition. The latter collisions, deposit energy within the sample and release secondary electrons, x-rays, light photons and heat. The secondary electrons contain mostly microstructural information. In this study, mostly secondary electrode detector was used, in order to check the morphology, grain growth and grain sizes.

4.2.5 Fourier Transformed Infrared Spectroscopy (FT-IR)

FT-IR spectroscopy was performed on a Nicolet 6700 FT-IR spectrometer with Collector II accessory for diffuse reflection infrared spectroscopy in air at room temperature. Usually as-prepared, dry and hydrated/deuterated samples in powder form are placed in a micro-sample holder for the measurement. Powder samples were subtracted with a run with optically transparent KBr. Optics used to optimally cover the range from 4000 cm^{-1} to 400 cm^{-1} with a resolution of 2 cm^{-1}. Primary objective to use this probe is to look for the broad O-H stretch vibrational band in the infrared (IR) absorbance spectrum. These bands in hydrated and as-prepared samples are attributed to the protons experiencing a range of hydrogen bonding strengths.

”

5: Results and Discussion

5.1 Indium/Ytterbium Heavily co-doped Barium Zirconate (Paper I)

The highest bulk proton conductivity and smallest activation energy have been reported so far for barium zirconate doped with 20 mol% of yttrium [125, 126]. Furthermore, doped barium zirconate, has high chemical stability, suggesting the material has a good potential for practical application, however the material also has some problems of poor sinterability and poorly conducting grain boundaries [122]. Recently, improved grain boundary conductivity and sinterability by way of using co-doping in $BaZrO_3$ has been reported [257, 258]. These studies were carried out on lightly doped (e.g.10 mol%) systems. The concentration of protons, can be increased, and hence potentially higher proton conductivity can be obtained, by heavy doping (above 20 mol %) [199, 259-261]. Therefore, we studied the oxygen deficient so called “heavily co-doped” perovskite oxide $BaZr_{0.5}In_{0.25}Yb_{0.25}O_{3-\delta}$ (BZIY50). Phase pure BZIY50 was successfully prepared via a wet chemical route (WCR). WCR was chosen as the preferred method of synthesis over the solid state route, since solid state method sintered sample showed an impurity phase ($Ba_2Yb_4O_9$). Analysis of X-ray powder diffraction data showed that the sample belongs to the cubic crystal system with space group *Pm*-3*m*. Dynamic thermogravimetric (TG) analysis confirmed complete filling of oxide ion vacancies by protonic defects during the hydration process. The proton conductivity was investigated by impedance spectroscopy. The bulk and total conductivities of pre-hydrated BZIY50 were found to be 8.5×10^{-4} and 2.2×10^{-5} Scm^{-1}, respectively, at 300°C.

The total conductivity in the co-doped perovskite oxide was higher compared to that of the respective single doped perovskite oxides phases like $BaZr_{0.5}In_{0.5}O_{3-\delta}$ [262] and $BaZr_{0.5}Yb_{0.5}O_{3-\delta}$ [260] with the same doping level. The bulk and grain-boundary mobility and diffusion coefficients of protons were calculated at 200°C using the conductivity and proton concentration data. Bulk diffusivity of BZIY50, is more than one order of magnitude higher compared to the lightly doped systems (for e.g. $BaZn_{0.9}In_{0.1}O_{3-\delta}$ in ref. [61]) where trapping of protons occurs.

5.2 ZnO as sintering aid in Ytterbium doped Barium zirconate (Paper II)

In this study 20 mol% Ytterbium (Yb^{3+}) doped barium zirconate was prepared from solid state reaction and sol-gel routes. For the first sol-gel sample, $BaZr_{0.8}Yb_{0.2}O_{3-\delta}$ +ZnO referred as Sol1:(BZY20)Z, Zn^{2+} was added as an excess of the stoichiometric formula. In the other cases, Zn^{2+} was added according to stoichiometry, giving a formula of $BaZr_{0.78}Zn_{0.02}Yb_{0.2}O_{3-\delta}$: referred to as Sol2:(BZZY20) and SS:(BZZY20) for sol-gel and solid state methods, respectively. The highest theoretical density, ≈ 90 %, was found for the Sol2:(BZZY20) sample where stoichiometry for Zn^{2+} was adjusted during mixing of the starting materials. For Sol1:(BZY20)Z and SS:(BZZY20), however, the densities were 73% and 78%, respectively and in addition some minor impurities (e.g.Yb_2O_3, $Yb_4Zr_3O_{12}$) were detected in these two samples. TGA of hydrated samples show a comparatively larger mass loss (74% of theoretical maximum) from the Sol2:(BZZY20) compared to 52% and 64% for Sol1:(BZY20)Z and SS:(BZZY20,) respectively. The total conductivity values of all of the pre-hydrated samples during heating were close to one order of magnitude higher compared to that of the cooling cycle below 600 °C with activation energy of 0.71 eV for Sol2:(BZZY20). The data shows that the addition of stoichiometric amounts of Zn^{2+} via sol-gel synthesis route promotes not only densification but also water incorporation and conductivity in comparison with the solid state route, keeping the same final sintering temperature of 1500°C. For Sol2:(BZZY20),

σ_{tot} at 600°C is 3.8×10^{-3} Scm^{-1} (pre-hydrated, under dry Ar). The results indicate addition of stoichiometric ZnO, enhances conductivity and density in comparison with the case of excess ZnO.

5.3 Characterisation of structure and conductivity of Sc^{3+} and In^{3+} substituted Barium Titanate (Paper III, V-VI)

5.3.1 Synthesis and Structure

$BaTi_{0.5}In_{0.5}O_{3-\delta}$ (BTI50) and $BaTi_{1-x}Sc_xO_{3-\delta}$ ($0.1<x<0.8$) were prepared by conventional solid state method from the starting chemicals of $BaCO_3$ and metal oxides. The preparation was similar apart from the higher final sintering temperature of 1550 °C for $BaTi_{1-x}Sc_xO_{3-\delta}$ ($0.5<x<0.8$) compared to that of 1400 °C for $BaTi_{0.5}In_{0.5}O_{3-\delta}$ (BTI50) and $BaTi_{1-x}Sc_xO_{3-\delta}$ ($0.1<x<0.4$). Giannici et al. [261] and Ahmed et al. [263] have pointed out that the high In-dopant level is possible even when sintering at 1400 °C-1500 °C for $BaCeO_3$ and $BaZrO_3$ respectively. This leads to high proton concentration, and can compensate the lower proton mobility compared to the more usual Y-doped $BaCeO_3$, as yttrium solubility in $BaCeO_3$ reaches to a limit of about 20%. [261, 264]. Again, tolerance factor or ionic radii mismatch, electronegativity and absolute hardness of the dopant ions may influence the solubility of dopant in to the Barium titante structures. In^{3+} has lower absolute Pearson hardness (13) compared to that of (24.36) Sc^{3+} [265]. Pearson total hardness is defined as, $\eta = \frac{I-A}{2}$ (5.1)

where I is the ionization potential and A is the electron affinity of the chemical species (atom or ion). A given M^{n+} ion is classified as "soft" if a small amount of energy is sufficient to modify its electronic configuration, i.e., the ion is easily polarized. The hardness values and ionic radii for the ions discussed in this study are reported in Table 5.1. This softness of the In^{3+} might have favoured the synthesis compared to Sc^{3+}.

Both BTI50 and BTS50, are characterised within cubic symmetry and space group (*Pm*-3*m*). However, For the $BaTi_{1-x}Sc_xO_{3-\delta}$ series a transitions from tetragonal $BaTiO_3$ (space group *P*4*mm*) to hexagonal $P6_3/mmc$ symmetry occurs for x = 0.1-0.2 (Figure 5.1). At and above 50% Sc^{3+} substitution the materials adopt a cubic crystal system with space group *Pm*-3*m* (Figure 3.1). Table 5.2 summarises the crystal system, synthesis temperature and relative density of the studied materials. For x=0.3-0.4 and 0.8, the materials crystal structure is not comprehensively understood, hence these are not discussed further here. Jayaraman *et al.* [105] reported a series of disordered cubic phases ($0.25 < x < 0.85$), and a mixture of cubic and tetragonal phases ($0.0 < x < 0.25$) for $BaTi_{1-x}In_xO_{3-\delta}$.

Table 5.1. Effective Ionic Radius in Octahedral Coordination and Pearson Absolute Hardness of some relevant Ions.

	Ionic Radius (Å)	**Hardness, H (Ev)**
Sc^{3+}	0.745	24.36
Ti^{4+}	0.605	-------
Ti^{3+}	0.67	7.89.
Yb^{3+}	0.886	------
Zr^{4+}	0.72	23.60
In^{3+}	0.80	13.00
Y^{3+}	0.90	20.60
Zn^{2+}	0.74	10.88
Ba^{2+}		12.70
Ce^{4+}	0.87	14.10
Gd^{3+}	0.93	11.70

Refined cell parameters and bond lengths for as-prepared, vacuum-dried, and hydrated BTI50 and BTS50 are compared in Table 5.3. The obtained density of ~77-78 % for the conductivity pellets of BTS50 and BTS70 was relatively low despite the final sintering temperature of 1550 °C, whereas for BTS60 a relative density of 86% was

obtained. In comparison, for $BaTi_{0.5}In_{0.5}O_{3-\delta}$ the density was ~82 % whilst sintering at 1400 °C.

The sinterability of proton conducting ceramic electrolytes based on $BaZrO_3$ sometimes necessitates extremely high temperatures (~1600–1800 °C) for the purpose of densification. Such high temperatures and/or long annealing times, can lead to Ba evaporation which has been shown to reduce conductivity [266, 267] and, in addition, lead to secondary phases or distortions of the crystal structure [125, 212, 268, 269]. This suggests that the use of Indium as dopant may be advantageous in lowering the required sintering temperature. This minimizes potential Ba loss.

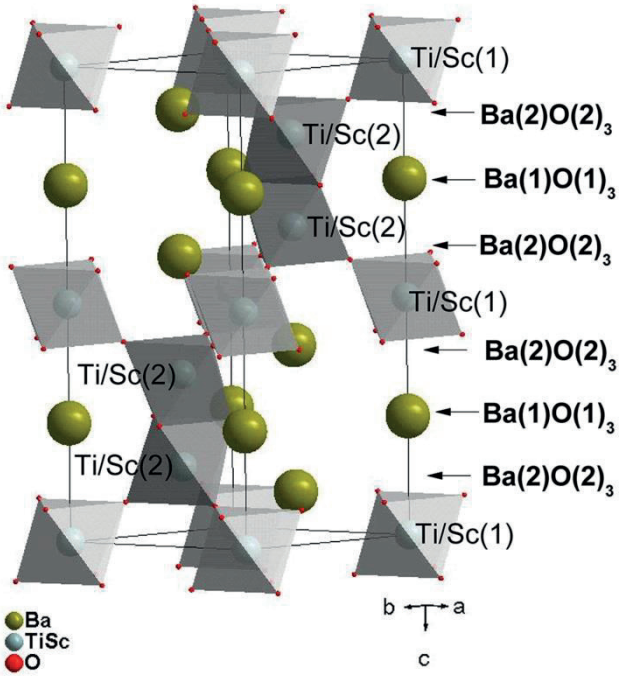

Figure 5.1 Polyhedral representation of the refined structure of hexagonal $BaTi_{0.9}Sc_{0.1}O_{3-\delta}$ (view along ab axis)

In order to verify the chemical composition, we have conducted area scanning EDS on the surface of as- prepared BTS50 and BTI50 pellets. The analysis shows the following (Atomic %) composition for BTS50 pellet: Ba to combined B site ratio, Ba:(Ti+Sc)=0.98 (±0.03), (see Table 5.4) which indicates a slight Ba loss is possible although the value obtained lies within the limit of the estimated standard deviation. BTI50, on the other hand, shows the expected composition.

In addition, to check this point further, we have prepared a pellet of the same sample under extra powder of the same composition to try to avoid any Ba evaporation. However, the density is not improved significantly (85-86%) for this sample. Even addition of ZnO (2 mol %) as a sintering aid was not successful in terms of significantly improving the density.

Table 5.2. Crystal system, synthesis temperature, and relative density of studied materials

Sample	**Crystal system /space group**	**Synthesis temperature, °C / route**	**Relative density %**
$BaTi_{0.5}In_{0.5}O_{3-\delta}$ (BTI50)	Cubic/ *Pm*-3*m*	1400	82
$BaTi_{0.9}Sc_{0.1}O_{3-\delta}$ (BTS10)	Hexagonal/ $P6_3/mmc$	1400	89
$BaTi_{0.8}Sc_{0.2}O_{3-\delta}$ (BTS20)	Hexagonal/ $P6_3/mmc$	1400	89
$BaTi_{0.5}Sc_{0.5}O_{3-\delta}$ (BTS50)	Cubic/ *Pm*-3*m*	1550	78
$BaTi_{0.4}Sc_{0.6}O_{3-\delta}$ (BTS60)	Cubic/ *Pm*-3*m*	1550	86
$BaTi_{0.3}Sc_{0.7}O_{3-\delta}$ (BTS70)	Cubic/ *Pm*-3*m*	1550	77
$BaZr_{0.8}Yb_{0.2}O_{3-\delta}$ +ZnO Sol1:(BZY20)Z	Cubic/ *Pm*-3*m*	1500/WCR	73
$BaZr_{0.78}Zn_{0.02}Yb_{0.2}O_{3-\delta}$ *Sol2:(BZZY20)*	Cubic/ *Pm*-3*m*	1500/WCR	90
$BaZr_{0.78}Zn_{0.02}Yb_{0.2}O_{3-\delta}$ SS:(BZZY20)	Cubic/ *Pm*-3*m*	1500	78
$BaZr_{0.5}In_{0.25}Yb_{0.25}O_{3-\delta}$:BZIY50	Cubic/ *Pm*-3*m*	1500/WCR	70

Table 5.3 Summary of lattice parameters and bond distances obtained from Rietveld analysis of X-ray powder diffraction data for as-prepared, vacuum-dried and hydrated (at 185 °C) $BaTi_{0.5}In_{0.5}O_{3-\delta}$ (BTI50) and $BaTi_{0.5}Sc_{0.5}O_{3-\delta}$ (BTS50) at RT.

	As-prepared	Vacuum-dried	Hydrated
Lattice parameter (Å)			
$BaTi_{0.5}In_{0.5}O_{3-\delta}$ (BTI50)	4.1536(1)	4.1539(1)	4.1623(1)/4.1528(1)*
$BaTi_{0.5}Sc_{0.5}O_{3-\delta}$ (BTS50)	4.1343(1)	4.1319(1)	4.1345(1)
Distances (Å) Ba-O			
$BaTi_{0.5}In_{0.5}O_{3-\delta}$ (BTI50)	2.93705(6)	2.93725(7)	2.94322(6)/2.9365*
$BaTi_{0.5}Sc_{0.5}O_{3-\delta}$ (BTS50)	2.92339(1)		
Distances (Å) Ti (In/Sc)-O			
$BaTi_{0.5}In_{0.5}O_{3-\delta}$ (BTI50)	2.07618(4)	2.07695(5)	2.08117(6)/2.0764*
$BaTi_{0.5}Sc_{0.5}O_{3-\delta}$ (BTS50)	2.92339(1)		

*Deuterated BTI50 ($BaTi_{0.5}In_{0.5}O_{2.53}(OD)_{0.44}$), data from Neutron powder diffraction at 4 K.

Table 5.4 Summary of EDS / SEM and crystallite size from XRPD (using Sherrer equation) for as-prepared $BaTi_{0.5}In_{0.5}O_{3-\delta}$ (BTI50) and $BaTi_{0.5}Sc_{0.5}O_{3-\delta}$ (BTS50).

	$BaTi_{0.5}In_{0.5}O_{3-\delta}$ (BTI50)			**$BaTi_{0.5}Sc_{0.5}O_{3-\delta}$ (BTS50)**		
	Ba	**Ti**	**In**	**Ba**	**Ti**	**In**
Atomic %	50.04	26.53	23.43	49.36	26.74	23.90
Standard deviation	2.09	1.91	0.39	1.67	0.52	1.15
Mean grain size (SEM image)		5μm			2-4 μm	
Mean crystallite size (XRPD)		96(1) nm			87(3) nm	

The relatively, higher melting point of Sc_2O_3 (m.pt. = 2485 °C), [compared with the lower value of In_2O_3 (m.pt. = 1910 °C)], might not be favourable for the sintering process. BTI50, though sintered at 1400 °C, has larger grains compared to BTS50

sintered at 150 °C higher temperature. Crystallite size from XRPD is much less than the average grain sizes obtained from SEM images.

5.3.3 Characterisation of conductivity

BTI50: For the as-prepared BTI50 sample, electrical conductivity was measured both with fixed and variable frequency AC impedance methods as a function of temperature, oxygen-, water vapour- and heavy water vapour partial pressures. Figure 5.2 (a), (b) and (c) display conductivity isotherms collected at 10 kHz as a function of $p(H_2O)$ in oxidizing condition, $p(O_2)$ in dry and wet states, respectively. The conductivity is strongly dependent on the partial pressure of H_2O at T < 600 °C. Fitting of the isotherms at lower temperatures such as 300 and 400 °C shown in Figure. 5.2(a) reveal exponents close to the expected value of 0.5 (see equation 3.12) whilst similar analysis of the $p(O_2)$ data in wet condition (Figure. 5.2 (c)) gives a maximum exponent value of ~0.05 for the isotherm at 600 °C, considerably lower than the expected value of 0.25 (see equation 3.13) for pure p-type conduction. Total conductivity with variable frequency AC electrochemical impedance spectroscopy also reveals two orders of magnitude higher values in wet O_2 and Ar condition than that of dry conditions. Proton conductivity is further confirmed from significant isotope effect, at 300 °C, $\sigma_H / \sigma_D = 2.02$. At T > 800 °C the material is a pure oxide ion conductor.

BTS50: For $BaTi_{0.5}Sc_{0.5}O_{3-\delta}$ (BTS50) electrical conductivity was measured with variable frequency AC impedance methods in oxygen, argon, and hydrogen under dry, hydrated (H_2O) and heavy water (D_2O) conditions. In the temperature range of 150 – 550 °C in a wet gas atmosphere the conductivity is significantly higher than that observed for dry conditions, indicating that protons are the dominant charge carriers. Isotope effect also provides evidence in favour of proton conductivity. Fitting of conductivity data

provides a hydration enthalpy change ΔH^0_{hydr} of -100±5 kJ/mol and hydration entropy change ΔS^0_{hydr} of -160±10 J/molK.

BTS50 shows mixed ionic and electronic conduction within the temperature interval of 150 – 1000 °C, with protonic contribution being greatest at T < 400 °C. The dry O_2 conductivity is consistently higher than that of dry Ar, indicating the existence of p-type electronic contribution throughout the temperature range (Figure 5.3). Whereas for BTI50, oxide ion conduction dominates above 800°C and a weak p-type conduction is observed at 600 °C from $p(O_2)$ studies. The total proton conductivity ($\sigma_{m,proton}$) and bulk conductivity ($\sigma_{m,bulk}$) of BTS50 and BTI50 at 300 °C in wet Ar is compared in Table 5.5 below.

By using equation (4.23) and taking n=3/2 specific total proton conductivity ($\sigma_{s,proton}$) and specific bulk conductivities ($\sigma_{s,bulk}$) are also presented in Table 5.5.

BTS20, BTS60, BTS70: Electrical conductivity was measured on pellets in a similar way described earlier by AC impedance spectroscopy as a function of temperature under dry and wet Ar, O_2 conditions as well as under deuterated O_2. The conductivity isobars performed on samples above 50 mol% Sc substituted $BaTiO_3$ reveal the expected strong dependence on $p(H_2O)$ at T < 500 °C along with significant isotope effect. The results show that higher scandium content leads to a higher total conductivity.

. On the other hand, hexagonal BTS20 though showing proton conductivity, the values are two orders of magnitude lower than BTS70. This is not surprizing, since the symmetry is lower and there are two different oxygen positions within the structure, which in turn can lead to proton trapping. It is also a general observation, that the highest symmetry compositions with larger cell volume, display the highest proton conductivity.

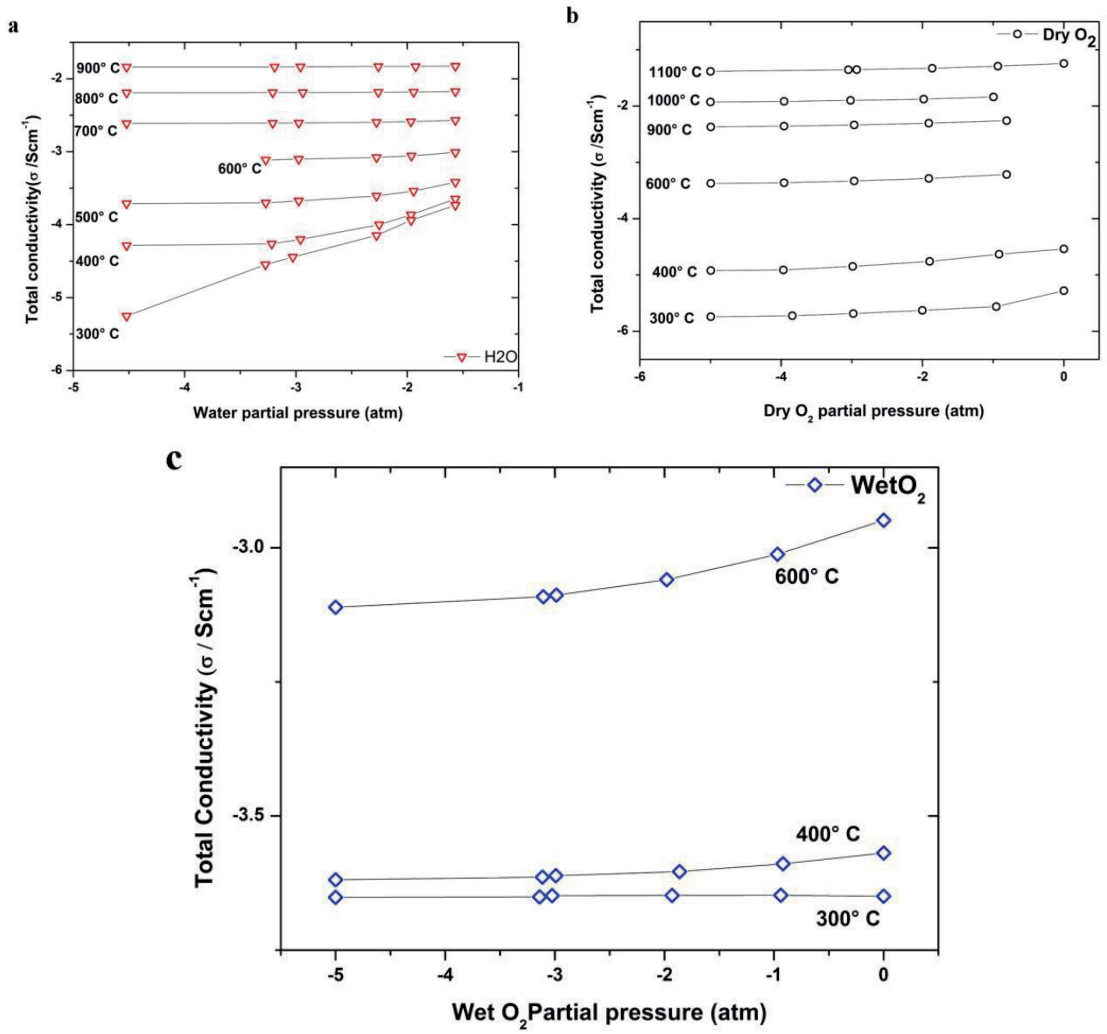

Figure 5.2. Isotherms of as-prepared $BaTi_{0.5}In_{0.5}O_{3-\delta}$ at 10 kHz. Total conductivity vs. (a) log $p(H_2O)$ in oxidizing condition: (b) log $p(O_2)$ in dry O_2+Ar mixture. (c) log $p(O_2)$ in wet O_2+Ar mixture.

.

Table 5.5 Total conductivity, Total proton conductivity ($\sigma_{m,proton}$) and bulk conductivity ($\sigma_{m,bulk}$) along with porosity corrected specific proton ($\sigma_{s,bulk}$) and bulk conductivity ($\sigma_{s,bulk}$) of BTI50, BTS50, BTS70 at 300 °C. For BTS20 only total and proton conductivity is shown at 400 °C.

	Total conductivity ($\sigma_{m,tot}$)Scm^{-1} Under Wet Ar	**Activation energy (E_a) (eV) in Wet Ar, T < 450 °C**	**Total proton conductivity ($\sigma_{m,proton}$) Scm^{-1}**	**Specific total proton conductivity ($\sigma_{s,proton}$) Scm^{-1}**	**Bulk conductivity ($\sigma_{m,bulk}$)Scm^{-1} Under Wet Ar**	**Specific bulk conductivity ($\sigma_{s,bulk}$) Scm^{-1} Under Wet Ar**
BTI50	9.07×10^{-5}	0.48	9.04×10^{-5}	1.22×10^{-4}	1.55×10^{-4}	2.09×10^{-4}
BTS50	1.44×10^{-4}	0.46	1.43×10^{-4}	2.07×10^{-4}	2.65×10^{-4}	3.84×10^{-4}
BTS70	3.77×10^{-4}	0.48	3.71×10^{-4}	5.49×10^{-4}	3.59×10^{-3}	5.31×10^{-3}
BTS20	2.61×10^{-6}	0.86	2.06×10^{-6}	2.44×10^{-6}	-	-

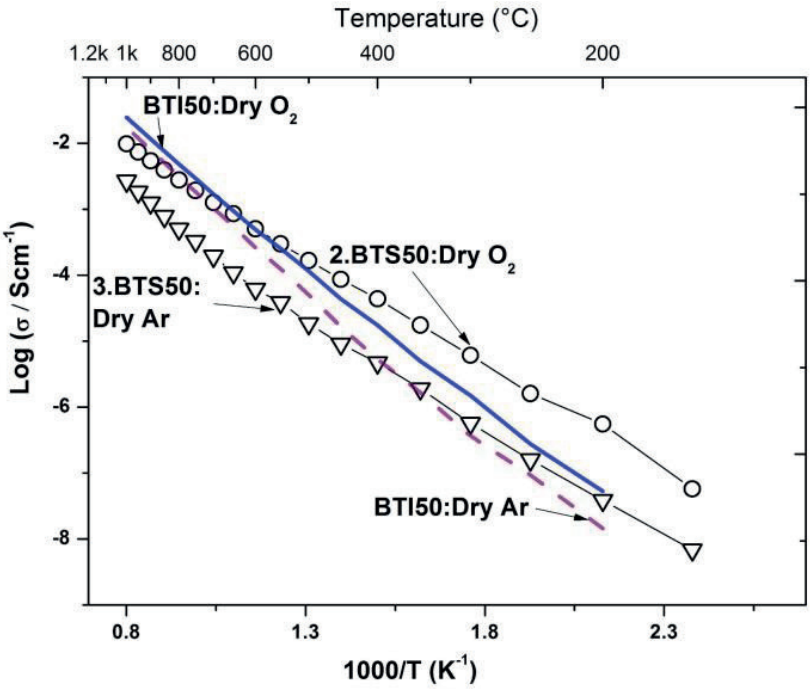

Figure 5.3. Comparison of total conductivities of as-prepared $BaTi_{0.5}Sc_{0.5}O_{3-\delta}$ (BTS50) vs. $BaTi_{0.5}In_{0.5}O_{3-\delta}$ (BTI50) measured in dry Ar /O_2 on cooling from 1000 to 150 °C.

5.4 Deuteron site and its local environment in BTI50 (Paper IV)

Deuterated $BaTi_{0.5}In_{0.5}O_{2.75}$ has been studied with neutron total (Bragg plus diffuse) scattering data. Here, both the Rietveld refinement method and the reverse Monte Carlo (RMC) modelling techniques are applied to investigate the preferred proton site, its local structural environment and that of the B-site cations.

The Rietveld refinement using the cubic space group $Pm\bar{3}m$ gave a good fit that accounts for all the observed Bragg peaks from the measured sample. This indicates that the long-range averaged structure can be described as perfectly cubic. The refined lattice parameter, a = 4.15283(2) Å, gives average Ba-O and Ti/In-O bond distances of 2.9365 Å, and 2.0764 Å, respectively. BVS calculations using the average cation-oxygen

distances, assuming a random oxygen vacancy distribution, give empirical bond valances of 2.070, 2.931, and 3.707, respectively, for the Ba^{2+}, Ti^{4+} and In^{3+} cations. The latter two values indicate that neither Ti^{4+} nor In^{3+} fit well in the oxygen octahedra given for the average $BaTi_{0.5}In_{0.5}O_{2.53}(OD)_{0.44}$ structure, which is also apparent from their widely different ionic radii, *i.e.* 0.605 Å for Ti^{4+} and 0.800 Å for In^{3+} [197]. It is, therefore, likely that the local structure environment, at least in the case of the TiO_6 and InO_6 octahedra, differ substantially from the average structure model.

The RMC obtained Ti-O and In-O radial distribution functions are markedly different from each other, with average Ti-O and In-O bond distances of 2.035 Å and 2.159 Å, respectively. The InO_6 octahedra are regular in shape whereas the TiO_6 octahedra are distorted. In addition, the Ti-O bond distribution is split into a shorter (≈ 1.65 Å to 2.10 Å) and a longer (≈ 2.10 Å to 2.55 Å) distribution, with average bond lengths of 1.90 Å and 2.34 Å, respectively, and oxygen coordination numbers of 4.10(1) and 1.84(1), respectively. The varying Ti-O bond distances, within one TiO_6 octahedra, coupled with the regular Ba/O lattice distortions hints at a combination of TiO_6 octahedra distortions and a high degree of Ti^{4+} off-centring from the crystallographic site, at least in comparison with the In^{3+} ions.

In terms of the deuteron position, the average O-D bond distance is found to be roughly 0.96 Å, and the preferred D^+ sites have a second nearest oxygen distance of 2.13 Å. This base on the RMC analysis confirms localised tilting of the deuteron and indicates a substantial amount of hydrogen bonding. Using a combined Rietveld and maximum entropy study on $BaSn_{0.5}In_{0.5}O_{2.75,}$ Ito *et al.* [15], reported that the D^+ ion was determined to be at, or very near, the 12*h* site (also called the bisector site, see Figure 5.4) with an O-D distance of 1.0 Å. For $BaTi_{0.5}In_{0.5}O_{2.53}(OD)_{0.44}$ sample the substantial tilting away from 12*h* position (Figure. 5.4) agrees well with experimental and theoretical studies concerning the structural impact of In-doping on the preferred proton site in $BaZrO_3$ [270-272][16, 19, 21] and $SrZrO_3$ [273]. In particular the present results support the 24k position suggested by Ahmed *et al.* [270] for $BaZr_{0.5}In_{0.5}O_{2.5}(OD)_{0.5}$.

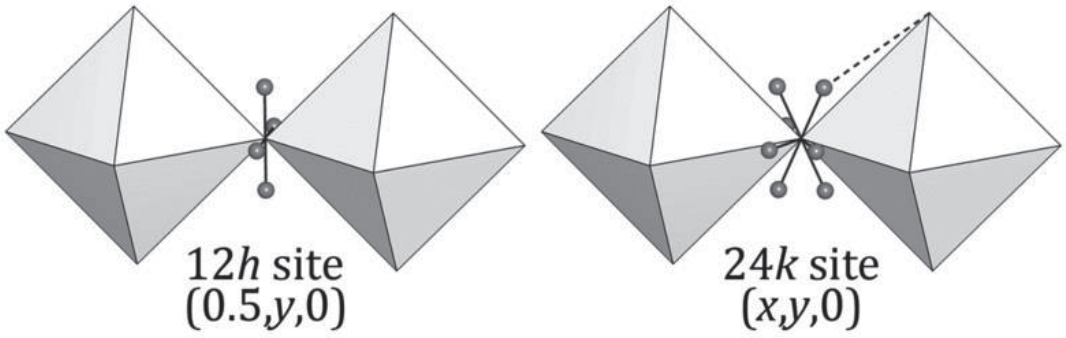

Figure 5.4 Polyhedral representations of the 12h and 24k sites for deuteron containg cubic perovskites (space group *Pm*-3*m*) with possible hydrogen bonding shown by the dashed line.

Based on a comparison of the 24k Rietveld results for the two phases it seems that the contraction of the unit cell caused by the smaller Ti ionic radii leads to a greater displacement of the D site from the perfect bisector position and results in a significantly closer next nearest O-D interaction, i.e. 2.13 Å for the titanate phase and 2.22(2) Å for the zirconate. Our findings for $BaTi_{0.5}In_{0.5}O_{2.53}(OD)_{0.44}$ based on the RMC analysis suggest tilting of the octahedra as rigid units is less prevalent and rather significant Ti^{4+} off-site displacements and distortion of the TiO_6 are likely to be the main mechanisms for relieving bond strain in the structure. The local structural information is useful in assessing the factors that impact on the proton mobility, such as jump distance and potential for hydrogen bonding.

6. Conclusion and future outlook

$BaZrO_3$ and $BaTiO_3$ based perovskite oxides with high acceptor doping were mainly synthesised using a solid state reaction route. The concept of high co-doping level at the B site and the use of ZnO as a sintering aid, both increased total conductivity. The best results were obtained when samples were prepared by wet chemical route. $BaTi_{1-x}Sc_xO_{3-\delta}$ with x = 0.1 and 0.2 (BTS10-20) are single phase and form a hexagonal (6H-$BaTiO_3$) structure , here shown for the first time. In the range 30-40 and above 80 mol% Sc^{3+} substitution and within the limit of solid state synthesis method, the structures are not comprehensively characterised and further work is necessary. On the other hand, samples with as much as 50% to 70% of the Ti substituted with Sc^{3+} (BTS50-70) adopt a cubic perovskite structure. Hydration behaviour indicates the filling of oxide ion vacancies by significant levels of proton defects. The effect of water vapour partial pressure, and the presence of an isotope effect, reveals that protons are the dominating charge carriers at temperatures below 600 °C; the conductivity of the material displays an enhancement almost two orders of magnitude in wet gas runs at $T \leq 300$ °C. The significantly higher total conductivity under dry O_2 than dry Ar run indicates a substantial contribution from p-type electron conductivity throughout the studied temperature range. The highest proton conductivity was achieved for the 70 mol% Sc^{3+} substituted $BaTiO_3$ with the composition of $BaTi_{0.3}Sc_{0.7}O_{3-\delta}$ (BTS70). For BTS70 the conductivity dependency on oxygen partial pressure is more significant than for BTI50. BTS70 is a good candidate for IT-SOFC applications as well as a potential mixed protonic and electronic conductor, though further optimisation is required in terms of density and grain boundary conduction.

Choice of dopant, basicity, electronegativity, tolerance factor can all be considered as controlling some of the factors influencing structure and hence proton

conductivity. Not all atoms form solid solution with $BaTiO_3$ to a very high level of doping. Both In and Sc are soluble while doping with other large atoms (such as Y and Yb) in $BaTiO_3$ did not produce single phase materials above 50-80 mol % when prepared by the solid state reaction route. Rietveld analysis on the hexagonal BTS20, shows that oxygen vacancy has a preference to reside on one particular oxygen site, and this phase shows much lower proton conductivity than that of cubic symmetry (BTS50-70). Synthesis with Sc_2O_3, for the Ti based perovskite system, seems not to favour achieving high relative density. In addition, the high melting point of Sc_2O_3 necessitates higher sintering temperature which can lead to Ba evaporation. In order to further improve proton conductivity, applying a co-doping strategy, using sintering aids and solution synthesis method for these materials would be worth trying in the future.

7. Acknowledgements

This is a scientific endeavour, without it; I certainly would have missed a great deal in my process of gathering knowledge. I would like to take the opportunity to thank all, who helped me out on this journey. Thanks to my supervisor, Professor Sten Eriksson, for understanding when to pursue and when not to, and displaying an unparalleled confidence in my abilities, even when my own confidence wavered. I thank my examiner Professor Jan-Erik Svensson along with former examiner professor Emeritus, Oliver Lindqvist for giving the opportunity at the Environmental Inorganic Chemistry division.

Sincere gratitude to all my co-supervisors; Associate Professors Chris Knee and Stefan Norberg and Dr. Istaq Ahmed for their invaluable thought, design of experiment, discussions, suggestions and input into my research. Financial support from Swedish Energy Agency (STEM) for this project is gratefully acknowledged. The Northern European Innovative Energy Research Programme (N-INNER) partners are thankfully remembered for scientific collaboration and prospect, especially, Professor Truls Norby and Associate Professor Reidar Haugsrud, University of Oslo, are gratefully remembered for their supervision and Harald Fjeld, Skjalg Erdal, Anna Magrasó, and Tor Svendsen Bjørheim all are kindly acknowledged for their help and friendship during the experiment at Oslo.

Special thanks to Professor Elisabet Ahlberg and Dr. Zareen Abbas, of the Electrochemistry group at Gothenburg University for their collaboration and invaluable discussion. I am grateful to Dr. Patrik Steegstra, University of Gothenburg for helping to collect SEM data. Valuable discussion on EDS data with assistant Professor Fang Liu, Dept. of Applied Physics, of Chalmers is gratefully acknowledged. Thanks to members

of the oxide group both current and former, including Dr. Annika Eriksson, Dr. Karinh Eurenius, Dr. Francis Kinyanjui and Stefan Saxin for making life in the office and in the labs enthusiastic and tidy. Much appreciation goes to collaborators Dr. Steve Hull and Dr. J.J.Biendicho of the ISIS facility in Oxford, U.K for their outstanding support not only in Neutron diffraction but also for access to the labs. Dr. Paul Henry of ESS, Scandinavia and Dr Abul K Azad of Universiti Brunei Darussalam are appreciated for valuable discussion. Dr. Maths Karlsson, Dr.Alexey Kalabukhov, Dr.Johan Bielecki and Nikolina Tuzla, Dept. of Applied Physics, of Chalmers, are gratefully thanked for scientific collaboration. I am grateful to all the former and current diploma students, Maria Nikumaa, Shengzhen Cai, Md. Khairul Hoque, Sara Ahmed, Jakob Svensson, Maja Rosengren, Zohreh Ghorbani Tari and the new member in Oxide group, Nico Torino.

Special thanks to Professor Vratislav Langer, Professor Lars-Gunnar Johansson, Professor Itai Panas, Docent Henrik Leon for sharing knowledge and views. Many thanks go to my Chalmers colleagues for their friendship especially, support personnel Roger Saghdahl, Esa Väänänen, Erik Svensson, Dr. Arvid Ödegård Jensen and Dr. Stefan Allard, for governing over the electronics and mechanical hardwires. I am thankful to Dr. Dongmei Zhao, for handling our safety issues, whereas Charlotte Bouveng for being generous, kind and nice in all official and management issues.

Finally, my wife, Tasnoova and my children deserve my endless appreciation and love, for being with me, encouraging, sacrificing and understanding me all these years. We have done this together. Thanks to my parents for their unconditional support in every single choice I've ever made.

8. References

[1] B. Cook, Introduction to fuel cells and hydrogen technology, *Engineering Science & Education Journal*, IEE (2002), p.205.
[2] Fuel Cell Today, http://www.fuelcelltoday.com/about-fuel-cells/technologies/, August 12, 2013.
[3] Y. Jamin, M. Raynolds, The Pembina Institute and the David Suzuki Foundation, Vancouver (2000).
[4] Pathways to Commercial Success: Technologies and Products, Department of Energy, Fuel Cell Technologies (FCT) Program, Office of Energy Efficiency and Renewable Energy (EERE). Pacific Northwest National Laboratory (PNNL) (2012).
[5] D. Steward, M. Penev, Hydrogen Technologies and Systems Center, National Renewable Energy Laboratory, Department of Energy (2010).
[6] A.S. Thorel, A. Chesnaud, M. Viviani, A. Barbucci, S. Presto, P. Piccardo, Z. Ilhan, D.E. Vladikova, Z. Stoynov, *ECS Transactions* **25** (2009) (2) 753.
[7] T. Norby, *Nature (London, U. K.)* **410** (2001) (6831) 877.
[8] E. Fabbri, D. Pergolesi, E. Traversa, *Chem Soc Rev* **39** (2010) (11) 4355.
[9] A. Boudghene Stambouli, E. Traversa, *Renewable and Sustainable Energy Reviews* **6** (2002) (3) 295.
[10] N.P. Brandon, S. Skinner, B.C.H. Steele, *Annual Review of Materials Research* **33** (2003) (1) 183.
[11] L. Carrette, K.A. Friedrich, U. Stimming, *Fuel Cells* **1** (2001) (1) 5.
[12] M. Conte, In: G. Editor-in-Chief: Jürgen, Editor, *Encyclopedia of Electrochemical Power Sources*, Elsevier, Amsterdam (2009), p.232-254.
[13] I. Dincer, M.A. Rosen, *Energy for Sustainable Development* **15** (2011) (2) 137.
[14] S. Gottesfeld, T.A. Zawodzinski, *Advances in Electrochemical Science and Engineering*, Wiley-VCH Verlag GmbH (2008), p.195-301.
[15] S.M. Haile, *Acta Materialia* **51** (2003) (19) 5981.
[16] S.M. Haile, P.N. Pintauro, *Journal of Materials Chemistry* **20** (2010) (30) 6211.
[17] S.P. Jiang, J. Li, Solid oxide fuel cells. Cathodes, CRC Press (2009), p.131-177.
[18] A. Kirubakaran, S. Jain, R.K. Nema, *Renewable and Sustainable Energy Reviews* **13** (2009) (9) 2430.
[19] N. Laosiripojana, W. Wiyaratn, W. Kiatkittipong, A. Arpornwichanop, A. Soottitantawat, S. Assabumrungrat, *Reviews on Solid Oxide Fuel Cell Technology* (2009).
[20] J. Larminie, A. Dicks, *Fuel Cell systems Explained*, John Wiley & sons Inc., England (2003).
[21] F. Lefebvre-Joud, G. Gauthier, J. Mougin, *J Appl Electrochem* **39** (2009) (4) 535.

[22] S. Mekhilef, R. Saidur, A. Safari, *Renewable and Sustainable Energy Reviews* **16** (2012) (1) 981.
[23] G. Meng, G. Ma, Q. Ma, R. Peng, X. Liu, *Solid State Ionics* **178** (2007) (7–10) 697.
[24] N.Q. Minh, *Journal of the American Ceramic Society* **76** (1993) (3) 563.
[25] M. Momirlan, T.N. Veziroglu, *International Journal of Hydrogen Energy* **30** (2005) (7) 795.
[26] T. Norby, R. Haugsrud, S. Marion, M.-A. Einarsrud, K. Wiik, O. Andersen, R.A. Stroem, T. Grande, Proton conducting solid electrolytes for electrochemical cells, (2006), p.36.
[27] A. Orera, P.R. Slater, *Chemistry of Materials* **22** (2010) (3) 675.
[28] K. Scott, C. Xu, X. Wu, *Wiley Interdisciplinary Reviews: Energy and Environment* (2013).
[29] S. Srinivasan, R. Mosdale, P. Stevens, C. Yang, *Annual Review of Energy and the Environment* **24** (1999) (1) 281.
[30] B.C.H. Steele, *Nature* **400** (1999) (6745) 619.
[31] B.C.H. Steele, A. Heinzel, *Nature* **414** (2001) (6861) 345.
[32] A.B. Stambouli, E. Traversa, *Renewable and Sustainable Energy Reviews* **6** (2002) (5) 433.
[33] E. Fabbri, L. Bi, D. Pergolesi, E. Traversa, *Advanced Materials* **24** (2012) (2) 195.
[34] IEA Energy Technology Essentials, http://www.iea.org/techno/essentials6.pdf, July, 2013.
[35] N. Ito, M. Iijima, K. Kimura, S. Iguchi, *Journal of Power Sources* **152** (2005) (0) 200.
[36] W.G. Coors, *Journal of Power Sources* **118** (2003) (1–2) 150.
[37] B. Zhu, M.D. Mat, *Int. J. Electrochem. Sci* **1** (2006) (8) 383.
[38] J. Huang, J. Yuan, Z. Mao, B. Sunde´ n, *Journal of Fuel Cell Science and Technology* **7** (2010) (1) 011012.
[39] X. Wang, Y. Ma, S. Li, A.-H. Kashyout, B. Zhu, M. Muhammed, *Journal of Power Sources* **196** (2011) (5) 2754.
[40] J. Zhang, Z. Xie, J. Zhang, Y. Tang, C. Song, T. Navessin, Z. Shi, D. Song, H. Wang, D.P. Wilkinson, Z.-S. Liu, S. Holdcroft, *Journal of Power Sources* **160** (2006) (2) 872.
[41] J. Jankovic, Proton Conductive Ceramic Materials for an Intermediate Temperature Proton Exchange Fuel Cell, Thesis, *Chemical And Biological Engineering*, The University of British Columbia Vancouver (2011).
[42] C. Xia, M. Liu, *Advanced Materials* **14** (2002) (7) 521.
[43] D.J.L. Brett, A. Atkinson, N.P. Brandon, S.J. Skinner, *Chemical Society Reviews* **37** (2008) (8) 1568.
[44] A. Tarancon, M. Burriel, J. Santiso, S.J. Skinner, J.A. Kilner, *Journal of Materials Chemistry* **20** (2010) (19) 3799.

[45] E.D. Wachsman, K.T. Lee, *Science* **334** (2011) (6058) 935.
[46] H. Yokokawa, In: T. Ishihara, Editor, *Perovskite Oxide for Solid Oxide Fuel Cells*, Springer US (2009), p.17-43.
[47] H. Yokokawa, H. Tu, B. Iwanschitz, A. Mai, *Journal of Power Sources* **182** (2008) (2) 400.
[48] B. Zhu, *Journal of Power Sources* **93** (2001) (1–2) 82.
[49] M.L. Faro, D. La Rosa, V. Antonucci, A.S. Arico, *Journal of the Indian Institute of Science* **89** (2012) (4) 363.
[50] K.T. Lee, H.S. Yoon, E.D. Wachsman, *Journal of Materials Research* **27** (2012) (16) 2063.
[51] A. Atkinson, J. Kilner, S. Skinner, N.P. Brandon, D.J. Brett, *Energy Production and Storage: Inorganic Chemical Strategies for a Warming World* (2010) 173.
[52] R. Haugsrud, T. Norby, *Nat Mater* **5** (2006) (3) 193.
[53] T. Norby, *Solid State Ionics* **125** (1999) (1-4) 1.
[54] R. Bashyam, P. Zelenay, *Nature* **443** (2006) (7107) 63.
[55] A.S. Arico, P. Bruce, B. Scrosati, J.-M. Tarascon, W. van Schalkwijk, *Nat Mater* **4** (2005) (5) 366.
[56] E. Fabbri, D. Pergolesi, A. D'Epifanio, E. Di Bartolomeo, G. Balestrino, S. Licoccia, E. Traversa, *Key Eng Mater* **421-422** (2010) 336.
[57] R. Peng, T. Wu, W. Liu, X. Liu, G. Meng, *Journal of Materials Chemistry* **20** (2010) (30) 6218.
[58] A. Evans, A. Bieberle-Hütter, J.L.M. Rupp, L.J. Gauckler, *Journal of Power Sources* **194** (2009) (1) 119.
[59] S. Hui, J. Roller, S. Yick, X. Zhang, C. Decès-Petit, Y. Xie, R. Maric, D. Ghosh, *Journal of Power Sources* **172** (2007) (2) 493.
[60] J.W. Fergus, *Journal of Power Sources* **162** (2006) (1) 30.
[61] K.D. Kreuer, *Annual Review of Materials Research* **33** (2003) 333.
[62] J.A. Asensio, E.M. Sanchez, P. Gomez-Romero, *Chemical Society Reviews* **39** (2010) (8) 3210.
[63] B. Smitha, S. Sridhar, A.A. Khan, *Journal of Membrane Science* **259** (2005) (1–2) 10.
[64] G. Alberti, M. Casciola, *Annual Review of Materials Research* **33** (2003) (1) 129.
[65] R. Borup, J. Meyers, B. Pivovar, Y.S. Kim, R. Mukundan, N. Garland, D. Myers, M. Wilson, F. Garzon, D. Wood, P. Zelenay, K. More, K. Stroh, T. Zawodzinski, J. Boncella, J.E. McGrath, M. Inaba, K. Miyatake, M. Hori, K. Ota, Z. Ogumi, S. Miyata, A. Nishikata, Z. Siroma, Y. Uchimoto, K. Yasuda, K.-i. Kimijima, N. Iwashita, *Chemical Reviews* **107** (2007) (10) 3904.
[66] M.A. Hickner, H. Ghassemi, Y.S. Kim, B.R. Einsla, J.E. McGrath, *Chemical Reviews* **104** (2004) (10) 4587.
[67] K. Sundmacher, L.K. Rihko-Struckmann, V. Galvita, *Catalysis Today* **104** (2005) (2–4) 185.

[68] V. Neburchilov, J. Martin, H. Wang, J. Zhang, *Journal of Power Sources* **169** (2007) (2) 221.
[69] Q. Li, R. He, J.O. Jensen, N.J. Bjerrum, *Chemistry of Materials* **15** (2003) (26) 4896.
[70] R.K. Nagarale, W. Shin, P.K. Singh, *Polymer Chemistry* **1** (2010) (4) 388.
[71] S.J. Peighambardoust, S. Rowshanzamir, M. Amjadi, *International Journal of Hydrogen Energy* **35** (2010) (17) 9349.
[72] L. Malavasi, C.A.J. Fisher, M.S. Islam, *Chemical Society Reviews* **39** (2010) (11) 4370.
[73] T. Norby, *Br. Ceram. Proc.* **63** (2003) (Grain Boundary Engineering of Electronic Ceramics) 1.
[74] H. Iwahara, *Solid State Ionics* **86–88, Part 1** (1996) (0) 9.
[75] H. Iwahara, Y. Asakura, K. Katahira, M. Tanaka, *Solid State Ionics* **168** (2004) (3–4) 299.
[76] H. Iwahara, *Solid State Ionics* **52** (1992) (1-3) 99.
[77] T. Norby, *MRS Bull.* **34** (2009) (12) 923.
[78] T. Norby, In: T. Ishihara, Editor, *Perovskite Oxide for Solid Oxide Fuel Cells*, Springer US (2009), p.217-241.
[79] R.K.B. Gover, P.R. Slater, *Annual Reports on the Progress of Chemistry - Section A* **100** (2004) 525.
[80] G.B. Zhang, D.M. Smyth, *Solid State Ionics* **82** (1995) (3–4) 161.
[81] C.A.J. Fisher, M.S. Islam, *Solid State Ionics* **118** (1999) (3-4) 355.
[82] N. Bonanos, *Solid State Ionics* **53-56** (1992) (Part 2) 967.
[83] P. Berastegui, S. Hull, F.J. García-García, S.G. Eriksson, *Journal of Solid State Chemistry* **164** (2002) (1) 119.
[84] J.F. Shin, K. Joubel, D.C. Apperley, P.R. Slater, *Dalton Trans.* **41** (2012) 261.
[85] J.F. Shin, D.C. Apperley, P.R. Slater, *Chemistry of Materials* **22** (2010) (21) 5945.
[86] J.B. Goodenough, Oxide-ion electrolytes, *Annual Review of Materials Research* (2003), p.91-128.
[87] H. Taroco, J. Santos, R. Domingues, T. Matencio, *Ceramic Materials for Solid Oxide Fuel Cells*, (2011).
[88] S.P.S. Badwal, F.T. Ciacchi, D. Milosevic, *Solid State Ionics* **136–137** (2000) (0) 91.
[89] V.V. Kharton, F.M.B. Marques, A. Atkinson, *Solid State Ionics* **174** (2004) (1–4) 135.
[90] S. Kim, U. Anselmi-Tamburini, H.J. Park, M. Martin, Z.A. Munir, *Advanced Materials* **20** (2008) (3) 556.
[91] C.E. Mohn, S. Stølen, S.T. Norberg, S. Hull, *Physical Review Letters* **102** (2009) (15) 155502.

[92] S. Hull, S.T. Norberg, M.G. Tucker, S.G. Eriksson, C.E. Mohn, S. Stolen, *Dalton Transactions* (2009) (40) 8737.
[93] A. Watanabe, *Solid State Ionics* **176** (2005) (31–34) 2423.
[94] A.A. Yaremchenko, V.V. Kharton, E.N. Naumovich, A.A. Tonoyan, *Materials Research Bulletin* **35** (2000) (4) 515.
[95] P. Shuk, H.D. Wiemhöfer, U. Guth, W. Göpel, M. Greenblatt, *Solid State Ionics* **89** (1996) (3–4) 179.
[96] A.M. Azad, S. Larose, S.A. Akbar, *Journal of Materials Science* **29** (1994) (16) 4135.
[97] T. Ishihara, H. Furutani, M. Honda, T. Yamada, T. Shibayama, T. Akbay, N. Sakai, H. Yokokawa, Y. Takita, *Chemistry of Materials* **11** (1999) (8) 2081.
[98] N. Trofimenko, H. Ullmann, *Solid State Ionics* **118** (1999) (3–4) 215.
[99] T. Ishihara, H. Matsuda, M. Azmi bin Bustam, Y. Takita, *Solid State Ionics* **86–88, Part 1** (1996) (0) 197.
[100] A. Petric, P. Huang, *Solid State Ionics* **92** (1996) (1–2) 113.
[101] A. Sinha, H. Näfe, B. Prakash Sharma, P. Gopalan, *Journal of The Electrochemical Society* **155** (2008) (3) B309.
[102] N. Zhou, G. Chen, H.J. Zhang, C. Zhou, *Physica B: Condensed Matter* **404** (2009) (21) 4150.
[103] J.B. Goodenough, J.E. Ruiz-Diaz, Y.S. Zhen, *Solid State Ionics* **44** (1990) (1-2) 21.
[104] T. Shimura, T. Yogo, *Solid State Ionics* **175** (2004) (1-4) 345.
[105] V. Jayaraman, A. Magrez, M. Caldes, O. Joubert, M. Ganne, Y. Piffard, L. Brohan, *Solid State Ionics* **170** (2004) (1-2) 17.
[106] T. Yao, Y. Uchimoto, M. Kinuhata, T. Inagaki, H. Yoshida, *Solid State Ionics* **132** (2000) (3–4) 189.
[107] M. Schwartz, B.F. Link, A.F. Sammells, *Journal of The Electrochemical Society* **140** (1993) (4) L62.
[108] A. Rolle, R.N. Vannier, N.V. Giridharan, F. Abraham, *Solid State Ionics* **176** (2005) (25–28) 2095.
[109] K. Kakinuma, A. Tomita, H. Yamamura, T. Atake, *J. Mater. Sci.* **41** (2006) (19) 6435.
[110] Y. Liu, R.L. Withers, J.F. Gerald, *Journal of Solid State Chemistry* **170** (2003) (2) 247.
[111] T. Norby, M. Wideroe, R. Glockner, Y. Larring, *Dalton Trans* (2004) (19) 3012.
[112] K.D. Kreuer, *Chemistry of Materials* **8** (1996) (3) 610.
[113] R.A. De Souza, Z.A. Munir, S. Kim, M. Martin, *Solid State Ionics* **196** (2011) (1) 1.
[114] H. Iwahara, T. Esaka, H. Uchida, N. Maeda, *Solid State Ionics* **3-4** (1981) (Aug) 359.
[115] T. Takahashi, H. Iwahara, *Rev. Chim. Miner* **17** (1980) (4) 243.

[116] H. Uchida, N. Maeda, H. Iwahara, *Solid State Ionics* **11** (1983) (2) 117.
[117] H. Iwahara, H. Uchida, K. Ono, K. Ogaki, *Journal of the Electrochemical Society* **135** (1988) (2) 529.
[118] H. Iwahara, *Solid State Ionics* **28** (1988) 573.
[119] H. Iwahara, H. Uchida, K. Morimoto, *Journal of the Electrochemical Society* **137** (1990) (2) 462.
[120] H. Iwahara, T. Yajima, T. Hibino, K. Ozaki, H. Suzuki, *Solid State Ionics* **61** (1993) (1-3) 65.
[121] R. Haugsrud, *Handbook of Fuel Cells*, John Wiley & Sons, Ltd (2010).
[122] K.H. Ryu, S.M. Haile, *Solid State Ionics* **125** (1999) (1–4) 355.
[123] P. Babilo, S.M. Haile, *Journal of the American Ceramic Society* **88** (2005) (9) 2362.
[124] S.W. Tao, J.T.S. Irvine, *Advanced Materials* **18** (2006) (12) 1581.
[125] E. Fabbri, D. Pergolesi, S. Licoccia, E. Traversa, *Solid State Ionics* **181** (2010) (21-22) 1043.
[126] K.D. Kreuer, S. Adams, W. Munch, A. Fuchs, U. Klock, J. Maier, *Solid State Ionics* **145** (2001) (1-4) 295.
[127] A.S. Nowick, Y. Du, K.C. Liang, *Solid State Ionics* **125** (1999) (1-4) 303.
[128] K.C. Liang, Y. Du, A.S. Nowick, *Solid State Ionics* **69** (1994) (2) 117.
[129] Y. Du, A.S. Nowick, *Journal of the American Ceramic Society* **78** (1995) (11) 3033.
[130] D.J.D. Corcoran, J.T.S. Irvine, *Solid State Ionics* **145** (2001) (1-4) 307.
[131] T. Omata, T. Fuke, S. Otsuka-Yao-Matsuo, *Solid State Ionics* **177** (2006) (26-32 SPEC. ISS.) 2447.
[132] A. Manthiram, J.F. Kuo, J.B. Goodenough, *Solid State Ionics* **62** (1993) (3-4) 225.
[133] T. Schober, J. Friedrich, *Solid State Ionics* **113** (1998) 369.
[134] W. Fischer, G. Reck, T. Schober, *Solid State Ionics* **116** (1999) (3–4) 211.
[135] T. Hashimoto, Y. Inagaki, A. Kishi, M. Dokiya, *Solid State Ionics* **128** (2000) (1–4) 227.
[136] I.E. Animitsa, N.A. Kochetova, A.R. Shaikhlislamova, *Russ. J. Electrochem.* **43** (2007) 708.
[137] T. Omata, M. Kita, Y. Goto, T. Okura, S. Otsuka-Yao-Matsuo, *Journal of the Electrochemical Society* **152** (2005) (6) A1068.
[138] M. Saito, S. Ito, T. Takayama, H. Yamamura, *Trans. Mater. Res. Soc. Jpn.* **34** (2009) 233.
[139] E. Quarez, S. Noirault, M.T. Caldes, O. Joubert, *J. Power Sources* **195** (2010) (4) 1136.
[140] V. Jayaraman, A. Magrez, M. Caldes, O. Joubert, F. Taulelle, J. Rodriguez-Carvajal, Y. Piffard, L. Brohan, *Solid State Ionics* **170** (2004) (1-2) 25.
[141] J. Jankovic, D.P. Wilkinson, R. Hui, *Journal of Power Sources* **201** (2012) 49.
[142] N. Hideshima, K. Hashizume, *Solid State Ionics* **181** (2010) (37-38) 1659.

[143] S. Ito, M. Saito, T. Takayama, H. Yamamura, *Trans. Mater. Res. Soc. Jpn.* **35** (2010) 507.
[144] P. Lacorre, F. Goutenoire, O. Bohnke, R. Retoux, Y. Laligant, *Nature* **404** (2000) (6780) 856.
[145] S. Georges, O. Bohnké, F. Goutenoire, Y. Laligant, J. Fouletier, P. Lacorre, *Solid State Ionics* **177** (2006) (19–25) 1715.
[146] S. Basu, P.S. Devi, H.S. Maiti, *Journal of the Electrochemical Society* **152** (2005) (11) A2143.
[147] L. León-Reina, E.R. Losilla, M. Martínez-Lara, M.C. Martín-Sedeño, S. Bruque, P. Núñez, D.V. Sheptyakov, M.A.G. Aranda, *Chemistry of Materials* **17** (2005) (3) 596.
[148] X. Kuang, M.A. Green, H. Niu, P. Zajdel, C. Dickinson, J.B. Claridge, L. Jantsky, M.J. Rosseinsky, *Nat Mater* **7** (2008) (6) 498.
[149] T. Omata, K. Okuda, S. Tsugimoto, S. Otsuka-Matsuo-Yao, *Solid State Ionics* **104** (1997) (3–4) 249.
[150] T. Omata, S. Otsuka-Yao-Matsuo, *Journal of The Electrochemical Society* **148** (2001) (6) E252.
[151] M.E. Bjorketun, C.S. Knee, B.J. Nyman, G. Wahnstrom, *Solid State Ionics* **178** (2008) (31-32) 1642.
[152] K.E.J. Eurenius, E. Ahlberg, I. Ahmed, S.G. Eriksson, C.S. Knee, *Solid State Ionics* **181** (2010) (3–4) 148.
[153] T. Norby, N. Christiansen, *Solid State Ionics* **77** (1995) (0) 240.
[154] S.M. Haile, C.R.I. Chisholm, K. Sasaki, D.A. Boysen, T. Uda, *Faraday Discussions* **134** (2007) (0) 17.
[155] R. Haugsrud, *Solid State Ionics* **178** (2007) (7–10) 555.
[156] S. Erdal, L.-E. Kalland, R. Hancke, J. Polfus, R. Haugsrud, T. Norby, A. Magrasó, *International Journal of Hydrogen Energy* **37** (2012) (9) 8051.
[157] A. Rothschild, W. Menesklou, H.L. Tuller, E. Ivers-Tiffée, *Chemistry of Materials* **18** (2006) (16) 3651.
[158] I. Riess, *Solid State Ionics* **157** (2003) (1–4) 1.
[159] H. Ullmann, N.T.A. Naoumidis, D. StoÌˆver, *Journal of the European Ceramic Society* **19** (1999) (6-7) 791.
[160] T. Norby, Y. Larring, *Solid State Ionics* **136-137** (2000) 139.
[161] F. Emiliana, P. Daniele, T. Enrico, *Science and Technology of Advanced Materials* **11** (2010) (4) 044301.
[162] D. Westphal, G.C. Mather, F.M.B. Marques, S. Jakobs, U. Guth, *Solid State Ionics* **136–137** (2000) (0) 19.
[163] S.J. Skinner, *International Journal of Inorganic Materials* **3** (2001) (2) 113.
[164] T. Ishihara, In: T. Ishihara, Editor, *Perovskite Oxide for Solid Oxide Fuel Cells*, Springer US (2009), p.1-16.
[165] T. Norby, KJM5120 and KJM9120 Defects and Reaction Lecture notes, www.uio.no, January, 2012.

[166] P. Murugaraj, K.D. Kreuer, T. He, T. Schober, J. Maier, *Solid State Ionics* **98** (1997) (1-2) 1.
[167] J. Maier, *Physical chemistry of ionic materials: ions and electrons in solids*, Wiley. com (2004).
[168] C. Wagner, *Annual Review of Materials Science* **7** (1977) (1) 1.
[169] N. Bonanos, *Solid State Ionics* **145** (2001) (1–4) 265.
[170] S.-J. Song, E.D. Wachsman, S.E. Dorris, U. Balachandran, *Solid State Ionics* **149** (2002) (1–2) 1.
[171] A. Puntis, *An Introduction to Mineral Sciences*, Cambridge University Press (1992).
[172] F.A. Kröger, H.J. Vink, In: S. Frederick, T. David, Editors, *Solid State Physics*, Academic Press (1956), p.307-435.
[173] K.D. Kreuer, *Solid State Ionics* **125** (1999) (1-4) 285.
[174] R. Glockner, M.S. Islam, T. Norby, *Solid State Ionics* **122** (1999) (1-4) 145.
[175] H. Iwahara, In: T. Ishihara, Editor, *Perovskite Oxide for Solid Oxide Fuel Cells*, Springer US (2009), p.45-63.
[176] I. Fahle, Defects and Transport in Ti-doped Ca2AlNbO6 and Ca2YNbO6, Thesis, University of Oslo, (2012).
[177] T. Norby, Y. Larring, *Curr. Opin. Solid State Mater. Sci.* **2** (1997) (5) 593.
[178] K.D. Kreuer, *Solid State Ionics* **97** (1997) (1-4) 1.
[179] A.L. Allred, E.G. Rochow, *Journal of Inorganic and Nuclear Chemistry* **5** (1958) (4) 264.
[180] T.S. Bjørheim, A. Kuwabara, I. Ahmed, R. Haugsrud, S. Stølen, T. Norby, *Solid State Ionics* **181** (2010) (3–4) 130.
[181] P. Babilo, *Processing and characterization of proton conducting yttrium doped barium zirconate for solid oxide fuel cell applications*, Thesis, California Institute of Technology (2007).
[182] J. Wu, *Defect chemistry and proton conductivity in Ba-based perovskites,* Thesis, California Institute of Technology (2005).
[183] A. Navrotsky, D.J. Weidner, *Perovskite: a structure of great interest to geophysics and materials science*, American Geophysical Union (1989).
[184] A.S. Nowick, A.V. Vaysleyb, *Solid State Ionics* **97** (1997) (1-4) 17.
[185] T. Norby, P. Koestad, *Solid State Ionics* **20** (1986) 169.
[186] W. Münch, K.D. Kreuer, Adams, G. Seifert, J. Maier, *Phase Transitions* **68** (1999) (3) 567.
[187] R.A. Davies, M.S. Islam, J.D. Gale, *Solid State Ionics* **126** (1999) (3–4) 323.
[188] M.S. Islam, *Solid State Ionics* **154–155** (2002) (0) 75.
[189] F. Shimojo, K. Hoshino, *Solid State Ionics* **145** (2001) (1–4) 421.
[190] M.S. Islam, M. Cherry, *Solid State Ionics* **97** (1997) (1–4) 33.
[191] R.C.T. Slade, N. Singh, *Journal of Materials Chemistry* **1** (1991) (3) 441.
[192] T. Scherban, Y.M. Baikov, E.K. Shalkova, *Solid State Ionics* **66** (1993) (1–2) 159.

[193] R. Hancke, Z. Li, R. Haugsrud, *Journal of The Electrochemical Society* **160** (2013) (8) F757.
[194] T. Hibino, K. Mizutani, H. Iwahara, *Journal of The Electrochemical Society* **140** (1993) (9) 2588.
[195] K.C. Liang, A.S. Nowick, *Solid State Ionics* **61** (1993) (1-3) 77.
[196] V.P. Gorelov, V.B. Balakireva, *Russian Journal of Electrochemistry* **33** (1997) (12) 1346.
[197] R. Shannon, *Acta Crystallographica Section A* **32** (1976) (5) 751.
[198] Y. Yamazaki, P. Babilo, S.M. Haile, *Chemistry of Materials* **20** (2008) (20) 6352.
[199] I. Ahmed, S.G. Eriksson, E. Ahlberg, C.S. Knee, P. Berastegui, L. Johansson, H. Rundlof, M. Karlsson, A. Matic, L. Borjesson, *Solid State Ionics* **177** (2006) (17-18) 1395.
[200] I. Ahmed, Acceptor-Doped BaZrO3 Perovskite: Synthesis, Structure and Proton Conductivity, Chalmers University of Technology,ISBN 978-91-7385-101-5 (2008).
[201] W. Munch, K.D. Kreuer, G. Seifert, J. Maier, *Solid State Ionics* **136** (2000) 183.
[202] S.M.H. Rahman, C.S. Knee, I. Ahmed, S.G. Eriksson, R. Haugsrud, *International Journal of Hydrogen Energy* **37** (2012) (9) 7975.
[203] G.B. Zhang, D.M. Smyth, *Solid State Ionics* **82** (1995) (3–4) 153.
[204] I. Animitsa, N. Tarasova, Y. Filinkova, *Solid State Ionics* **207** (2012) (0) 29.
[205] A.R. West, *Solid State Chemistry and Its Applications*, Wiley. com (1991).
[206] R. Merkle, J. Maier, *Zeitschrift für anorganische und allgemeine Chemie* **631** (2005) (6-7) 1163.
[207] T. Schober, H.G. Bohn, *Solid State Ionics* **127** (2000) (3-4) 351.
[208] Z. Sun, E. Fabbri, L. Bi, E. Traversa, *Journal of the American Ceramic Society* **95** (2012) (2) 627.
[209] A.K. Azad, J.T.S. Irvine, *Solid State Ionics* **179** (2008) (19-20) 678.
[210] Y. Guo, R. Ran, Z. Shao, *International Journal of Hydrogen Energy* **35** (2010) (11) 5611.
[211] H.d.A.L. Viana, J.T.S. Irvine, *Journal of Materials Chemistry* **20** (2010) (39) 8506.
[212] S. Ricote, N. Bonanos, *Solid State Ionics* **181** (2010) (15–16) 694.
[213] S. Tao, J.T.S. Irvine, *Journal of Solid State Chemistry* **180** (2007) (12) 3493.
[214] D. Gao, R. Guo, *Journal of Alloys and Compounds* **493** (2010) (1–2) 288.
[215] C. Zhang, H. Zhao, N. Xu, X. Li, N. Chen, *International Journal of Hydrogen Energy* **34** (2009) (6) 2739.
[216] J.-S. Park, J.-H. Lee, H.-W. Lee, B.-K. Kim, *Solid State Ionics* **181** (2010) (3-4) 163.
[217] U. Holzwarth, N. Gibson, *Nature Nanotechnology* **6** (2011) (9) 534.
[218] B.D. Cullity, S.R. Stock, *Elements of X-ray Diffraction*, Prentice hall Upper Saddle River, NJ (2001).

[219] M.T. Weller, *Inorganic materials chemistry*, Oxford University Press Oxford (1994).
[220] D8 ADVANCE/D8 DISCOVER, User Manual, Bruker AXS GmbH (2010), http://www.bruker.com/products/x-ray-diffraction-and-elemental-analysis/x-ray-diffraction/d8-advance/learn-more.html.
[221] R.M. Ibberson, W.I. David, *Structure determination from powder diffraction data. IUCr monographs on Crystallography* **13** (2006).
[222] B.T.M. Willis, C.J. Carlile, *Experimental neutron scattering*, Oxford Univ. Press (2009).
[223] G. Bacon, *Neutron Diffraction*, *Clarendon, Oxford* (1975).
[224] H.M. Rietveld, *Journal of Applied Crystallography* **2** (1969) 65.
[225] R.A. Young, *The Rietveld Method*, Oxford University Press, Oxford, ISBN 0 19855577 6, (1993).
[226] L.B. McCusker, R.B. Von Dreele, D.E. Cox, D. Louer, P. Scardi, *Journal of Applied Crystallography* **32** (1999) (1) 36.
[227] J.I. Langford, L. Daniel, *Reports on Progress in Physics* **59** (1996) (2) 131.
[228] S.T. Norberg, M.G. Tucker, S. Hull, *Journal of Applied Crystallography* **42** (2009) (2) 179.
[229] T. Proffen, S.J.L. Billinge, *Journal of Applied Crystallography* **32** (1999) (3) 572.
[230] R.L. McGreevy, *Journal of Physics-Condensed Matter* **13** (2001) (46) R877.
[231] H. Ress, L. Bruegemann, Powder XRD Instrumentation and Data Quality – Sep 30, 2010, *Good Diffraction Practice, Webinar Series,* (2010).
[232] A.C. Larson, R.B.V. Dreele, **Los Alamos National Laboratory Report LAUR 86-748** (2004).
[233] B.H. Toby, *Journal of Applied Crystallography* **34** (2001) 210.
[234] J. Rodriguez Carvajal, *Physica B* **192** (1993).
[235] P.-E. Werner, L. Eriksson, M. Westdahl, *Journal of Applied Crystallography* **18** (1985) (5) 367.
[236] J. laugier, B. Bochu, LMGP-Suite Suite of Programs for the interpretation of X-ray Experiments, (2000).
[237] S. Hull, R.I. Smith, W.I.F. David, A.C. Hannon, J. Mayers, R. Cywinski, *Physica B: Physics of Condensed Matter* **180-181** (1992) (PART 2) 1000.
[238] A.K. Soper, Gudrun − A computer program developed for analysis of neutron diffraction data. http://www.isis.stfc.ac.uk/groups/disordered-materials/software/. (April 2010).
[239] M.G. Tucker, D.A. Keen, M.T. Dove, A.L. Goodwin, Q. Hui, *Journal of Physics: Condensed Matter* **19** (2007) (33) 335218.
[240] J.E. Bauerle, *Journal of Physics and Chemistry of Solids* **30** (1969) (12) 2657.
[241] J.R. Macdonald, *J Electroanal Chem* **223** (1987) (1-2) 25.
[242] J.T.S. Irvine, D.C. Sinclair, A.R. West, *Advanced Materials* **2** (1990) (3) 132.

[243] N. Bonanos, B.C.H. Steele, E.P. Butler, *Impedance Spectroscopy*, John Wiley & Sons, Inc. (2005), p.205-537.
[244] J.R. Macdonald, W.B. Johnson, *Impedance Spectroscopy*, John Wiley & Sons, Inc. (2005), p.1-26.
[245] M.E. Orazem, B. Tribollet, *Electrochemical impedance spectroscopy*, Wiley. com (2011).
[246] T. Norby, *Compendium for the advanced level course: Experimental methods KJM-MENA4010 Module* **2** (2009), www.uio.no, January, 2012, .
[247] D. Vladikova, J.A. Kilner, S.J. Skinner, G. Raikova, Z. Stoynov, *Electrochimica Acta* **51** (2006) (8–9) 1611.
[248] A. Lasia, In: B.E. Conway, J.O.M. Bockris, R. White, Editors, *Modern Aspects of Electrochemistry*, Springer US (2002), p.143-248.
[249] S.M. Haile, D.L. West, J. Campbell, *Journal of Materials Research* **13** (1998) (6) 1576.
[250] NorECs. Probostat™, http://www.norecs.com/, February 2013.
[251] A. Løken, *Thermodynamics and transport of defects in Sc-doped CaSnO3 and CaZrO3*, Thesis, University of Oslo, 2011, (2011).
[252] SMaRT Impedance Measurement Software, Solartron Analytical.
[253] T. Norby, P. Kofstad, *Journal of the American Ceramic Society* **69** (1986) 780.
[254] K.A. Furøy, R. Haugsrud, M. Hänsel, A. Magrasó, T. Norby, *Solid State Ionics* **178** (2007) (7-10) 461.
[255] A. Holt, P. Kofstad, *Solid State Ionics* **100** (1997) (3–4) 201.
[256] R. Marassi, F. Nobili, In: G. Editor-in-Chief: Jürgen, Editor, *Encyclopedia of Electrochemical Power Sources*, Elsevier, Amsterdam (2009), p.758-768.
[257] S. Imashuku, T. Uda, Y. Nose, K. Kishida, S. Harada, H. Inui, Y. Awakura, *Journal of The Electrochemical Society* **155** (2008) (6) B581.
[258] N. Ito, H. Matsumoto, Y. Kawasaki, S. Okada, T. Ishihara, *Solid State Ionics* **179** (2008) (9–10) 324.
[259] I. Ahmed, S.G. Eriksson, E. Ahlberg, C.S. Knee, M. Karlsson, A. Matic, D. Engberg, L. Borjesson, *Solid State Ionics* **177** (2006) (26-32) 2357.
[260] I. Ahmed, C.S. Knee, S.-G. Eriksson, E. Ahlberg, M. Karlsson, A. Matic, L. Borjesson, *Journal of the Electrochemical Society* **155** (2008) (11) P97.
[261] F. Giannici, A. Longo, A. Balerna, K.-D. Kreuer, A. Martorana, *Chemistry of Materials* **19** (2007) (23) 5714.
[262] I. Ahmed, S.G. Eriksson, E. Ahlberg, C.S. Knee, *Solid State Ionics* **179** (2008) (21-26) 1155.
[263] I. Ahmed, S.G. Eriksson, E. Ahlberg, C.S. Knee, P. Berastegui, L.G. Johansson, H. Rundlof, M. Karlsson, A. Matic, L. Borjesson, D. Engberg, *Solid State Ionics* **177** (2006) (17-18) 1395.
[264] L. Bi, S.Q. Zhang, L. Zhang, Z.T. Tao, H.Q. Wang, W. Liu, *International Journal of Hydrogen Energy* **34** (2009) (5) 2421.

[265] R.G. Pearson, *Inorganic Chemistry* **27** (1988) (4) 734.
[266] H.G. Bohn, T. Schober, *Journal of the American Ceramic Society* **83** (2000) (4) 768.
[267] F. Iguchi, T. Yamada, N. Sata, T. Tsurui, H. Yugami, *Solid State Ionics* **177** (2006) (26–32) 2381.
[268] Y. Yamazaki, R. Hernandez-Sanchez, S.M. Haile, *Chem. Mater.* **21** (2009) 2755.
[269] F. Iguchi, T. Tsurui, N. Sata, Y. Nagao, H. Yugami, *Solid State Ionics* **180** (2009) (6–8) 563.
[270] I. Ahmed, C.S. Knee, M. Karlsson, S.G. Eriksson, P.F. Henry, A. Matic, D. Engberg, L. Borjesson, *Journal of Alloys and Compounds* **450** (2008) (1-2) 103.
[271] M. Karlsson, M.E. Björketun, P.G. Sundell, A. Matic, G. Wahnström, D. Engberg, L. Börjesson, I. Ahmed, S.G. Eriksson, P. Berastegui, *Physical Review B* **72** (2005) (9) 094303.
[272] S.J. Stokes, M.S. Islam, *Journal of Materials Chemistry* **20** (2010) (30) 6258.
[273] C. Shi, M. Morinaga, *Journal of Computational Chemistry* **27** (2006) (6) 711.